MODELING AND CHARACTERIZATION OF MECHANICAL PROPERTIES IN LASER POWDER BED FUSION ADDITIVE MANUFACTURED INCONEL 718

by

Senthamilaruvi Moorthy

A Thesis submitted to the Faculty and The Board of Trustees of the Colorado School of Mines in partial fulfillment of the requirements of the degree of Master of Science (Mechanical Engineering)

Golden, Colorado

Date: _____

Signed: _____

Senthamilaruvi Moorthy

Signed: _____

Dr. Aaron Stebner

Thesis Advisor

Golden, Colorado

Date: _____

Signed: _____

Dr. John Berger

Professor and Department

Head of Mechanical Engineering

ABSTRACT

Laser powder bed fusion (L-PBF) is a promising additive manufacturing process capable of manufacturing near net shaped components directly from digital computer-aided-design (CAD) data. Lack of consistency in mechanical properties of L-PBF printed parts prevent widespread adaptation of this technique in industry. To understand the factors that cause variability and inconsistency in mechanical properties two plates each of tensile and compression samples were L-PBF printed in various orientations using Inconel 718 alloy. One plate each of compression and tensile samples was subjected to solution annealing and double aging heat treatment. Tensile, compressive and hardness properties were measured in as built and heat-treated condition. Compressive properties were also characterized in the machined condition to understand the influence of all post-processing activities on mechanical properties. Porosity of compression samples was characterized with X-ray micro computed tomography to understand the influence of porosity on mechanical properties.

Apart from build orientation, factors such as shape, thickness and laser scanning path were found to cause variation in mechanical properties. Anisotropy in mechanical properties that developed because of build orientation and laser scanning path was retained after heat treatment. Hardness increased by 58% after heat treatment. More than 50% of porosity by volume was found to be removed after machining compression samples from 2mm nominal diameter down to 1.5mm diameter. The samples also showed higher yield and Young's modulus after machining. An attempt has been made to explain the observed variability in mechanical properties across orientation and part position on the build plate using machine learning algorithms. Although the regression approach could not explain the variability, the classification technique seems to be a plausible approach. Orientation and position could not completely explain the variability in mechanical properties. This suggests that more variables are involved in determining the final mechanical properties of L-PBF printed parts.

TABLE OF CONTENTS

LIST OF FIGURES

LIST OF TABLES

ACKNOWLEDGEMENTS

I would like to express my sincere gratitude and respects to my advisor Dr. Aaron Stebner and Dr. Branden Kappes for helping me academically and personally throughout my time as a Master's student at Colorado School of Mines. It is their guidance and support that kept me motivated to tirelessly pursue my research work. I feel proud to have worked in the ADAPT group with Dr. Stebner and Dr. Kappes.

I am grateful to my fellow researcher Garrison Hommer for spending his time to help me learn the Digital Image Correlation technique which is an important part of my research. I am thankful to all ADAPT and Beam Team colleagues who helped me in this research. I appreciate all help and support provided by Bryan Marsh and other undergraduate students in designing experimental setups.

I would like to thank my committee members Mr. Craig Brice and Dr. John Berger for their help and support. And I am grateful to my sponsor Faustson Tools, who provided equipment and samples to conduct this research.

I thank Mr. Raguram Ramamoorthy and all my friends who encouraged me to pursue my Master's degree. Above all, I thank my mother Mrs. Kokilavani, and my father Mr. A.R. Moorthy, and all my teachers who made me what I am today.

Senthamilaruvi Moorthy

CHAPTER 1

INTRODUCTION

Most conventional manufacturing (subtractive) processes used extensively in industry involve the removal of material to shape the final product. Additive manufacturing builds up each part by adding material according to a 3D model, usually layer upon layer [1]. In 1983, Chuck Hull invented stereolithography, a rapid prototyping process which uses UV light to photopolymerize thin layers of light-sensitive polymer into a three-dimensional part [2]. Many layer-based manufacturing techniques have evolved.

Additive manufacturing (AM) is gaining importance because of its unique ability to produce a near net shape part directly from a 3D computer-aided-design (CAD) file. Also, AM offers the design freedom to include complicated geometries inaccessible to conventional machining processes, such as interdigitated internal channels. These unique capabilities also enable a high degree of customization. Some studies conclude that, by 2030, many custom products and spare parts will be manufactured by additive manufacturing [3]. Management experts predict that AM is going to be crucial for industries such as aerospace, where products with high complexity are needed, medicine, where individualization is beneficial, and oil and mining for replacement of parts in remote areas [4].

The unique capability of the laser powder bed fusion (L-PBF) process to produce fully dense parts with complicated geometries and light weight structures in metals has led to applications in medicine [5] and, aerospace [6] and in areas needing high value-added products. Currently, steel and iron-based alloys, titanium and titanium-based alloys and nickel-based alloys are the most used in the L-PBF process. Most of the research work in L-PBF process has been done with these alloys [7]. Although the availability of raw material in powder form restricts the use of other alloys, the list of materials used for this process is expected to grow in the near future. This research, in particular, focuses on the L-PBF process of Inconel 718 a nickel-based super alloy.

Inconel 718 alloy is known for its high strength, creep resistance, corrosion resistance and oxidation properties. Its ability to perform at higher temperatures (600 – 800 °C) makes it suitable for harsh environments [8]; hence, Inconel 718 alloy is used in the aerospace and, in the oil and

gas, and in nuclear reactors. Parts used in aerospace, nuclear energy, and oil and gas applications often have complicated geometries and hence are difficult to machine. Moreover, Inconel 718 work hardens and causes tool wear and breakage, making the machining process more complicated [9]. All these draw backs make AM, especially L-PBF a desirable alternative for conventional manufacturing.

Although there are many advantages to L-PBF, such as complete design freedom, manufacturing without tooling and minimal lead time, there are certain factors preventing it from widespread adoption. Foremost among them is a lack of consistency or repeatability in the mechanical properties of AM parts produced with L-PBF process. The objective of this thesis is to investigate reasons for these inconsistencies. Challenges in the characterization of the mechanical properties of AM samples in the as-built condition are discussed, as are the influences of porosity, sample orientation, and sample location on the build plate. The influences of post-processing activities, such as machining and heat-treatment, are also characterized. An attempt has been made to model the variation in mechanical properties with respect to position and orientation using machine learning algorithms.

1.1. Additive manufacturing

AM, which was once only used to make prototypes and models, has turned into a manufacturing process adapted by various manufacturing sectors and some projections show that by 2020 sales of industrial-grade 3-D printers in the United States will be 42% by volume of industrial automation and robotic sales [10]. Early AM technologies were only capable of printing polymers, but now metals, concrete, wood and even human cells can be additively manufactured. Because of its ability to manufacture objects directly from a digital file without the need for special tooling, jigs or fixtures, its applications and uses are growing continuously. As mentioned earlier, AM is the name for the group of technologies that use layer based manufacturing. Although the basic process chain for all AM processes is same, the physics behind the processes are entirely different. The AM process chain, classification and applications are discussed as follows.

1.1.1. Additive manufacturing process chain

As AM increasingly expands into more industries, a series of four steps have emerged to guide its development for new applications: choosing the right AM technology, design for additive

and model construction, selection and optimization of AM build parameters, and sample removal and post-processing.

Step 1: Choosing the right AM technology

Because there are various types of additive manufacturing processes such as VAT photopolymerization, material jetting, binder jetting, material extrusion, powder bed fusion, sheet lamination and directed energy deposition, the right process should be chosen for the specific application based on material requirements, the properties of the material generated by the process, and the cost, and production volume. AM processes are classified based on the raw material, binding technology, and joining technology involved in the process such as laser, extrusion thermal, etc. [11]. These classifications have been described by Bikas et al. and are shown in Fig 1.1 [12]. The ASTM F42 standard classifies additive manufacturing processes into seven major categories:

a) Vat photopolymerization: – This technique uses photopolymer resins, which solidify when exposed to light of a particular wavelength. Additive processes that use this technique include Stereolithography (SLA), Direct Light Processing (DLP), Continuous Direct Light Processing (CDLP) [13].

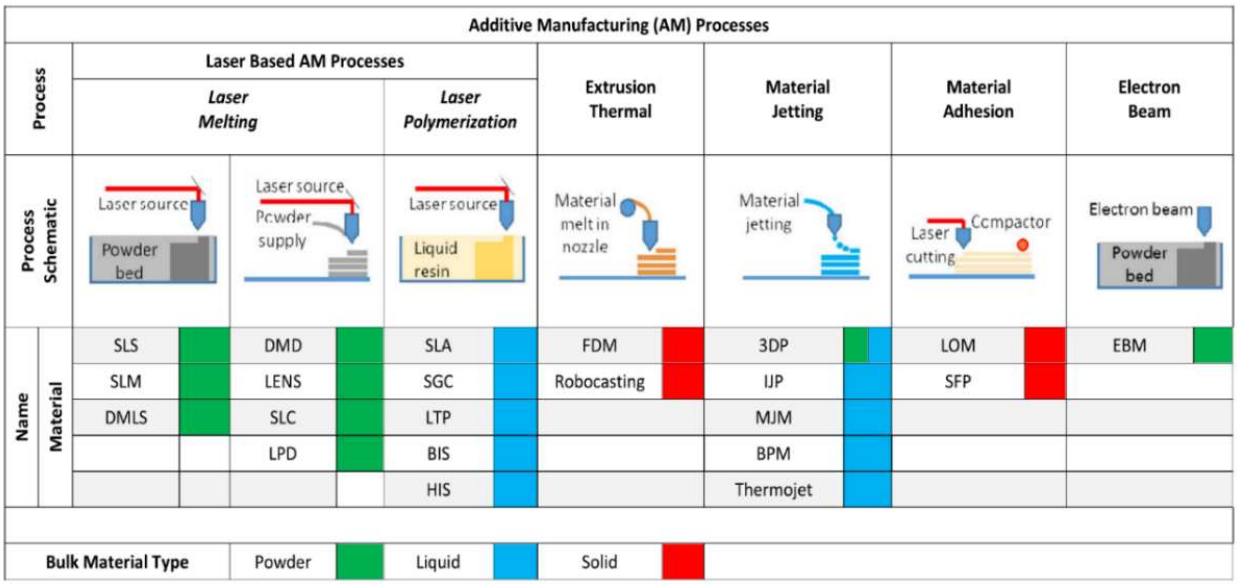

Fig. 1.1 Classification of additive manufacturing processes [12].
Reproduced under license CC BY 4.0

b) Material jetting: - Material is propelled directly onto the build plate, like an ordinary ink jet printer. Nano Particle Jetting (NPJ) and Drop on Demand (DOD) printers use this technology [11].

c) Binder jetting process: – The binder jetting process is very similar to the material jetting process except that it alternately deposits layers of material and binder. This provides an additional level of control, in that the material and binder may be controlled separately for functionally graded or hybrid builds.

d) Material extrusion: – In this process, the source material is heated and extruded as a continuous semi-solid wire to construct the part. This technique provides very interesting design modalities, such as the ability to construct parts with directionally anisotropic moduli along.

e) Powder bed fusion: – Raw material (metal or plastic) is fed in the form of powder and spread onto the build plate. Then a heat source, either a laser or electron beam, is used to selectively melt some part of the powder layer. A new layer of powder is then spread over the previous layer and the cycle is repeated to build a three-dimensional part. Selective Laser Melting, Selective Laser Sintering, Electron Beam Melting (EBM), and the Multi Jet Fusion process are examples of powder bed fusion technology [11].

f) Sheet lamination: – Material is fed in sheet form and cut to shape for each layer. These layers are then joined using ultrasonic welding or adhesives. Ultrasonic Additive Manufacturing (UAM) and Laminated Object Manufacturing (LOM) use sheet lamination technology [11].

g) Directed energy deposition: - In this type of process material is melted by a laser or electron beam as it is fed either in powder or wire form and deposited on the surface of the part or build plater. Laser Engineered Net Shape (LENS) and Electron Beam Additive Manufacturing processes (EBAM) uses this technology [11]

Step 2: Design for AM and model construction

After choosing the right AM technology, factors such as support structure, build orientation, simplification of design and topology optimization should be considered before designing a part for AM.

a) Support structure: When there is an overhanging portion in the part being printed all printers generate support structures to prevent failure of the print. These support structures are temporary

structures purposefully printed to be very weak to ease their removal after printing; however, the areas where the support structures contact the part become rough, which affects the surface finish. So, the design of the part should strategically avoid support structure in critical areas where surface finish is of importance. The software provided with the printer allows visualization of the part along with its support structures so that design could be modified to avoid support structures in critical areas of the part.

b) Build orientation: - Build orientation is an important factor because strength changes with respect to the printing orientation of a part. Additively printed part are usually weak along the build direction because of weaker interlayer bonding strength. A designer should be aware of this anisotropy in additive printing when designing parts for critical applications.

c) Simplification of design: - Multiple different parts are manufactured individually and assembled together to achieve a single functionality in a conventional manufacturing process. Such assemblies could be redesigned to combine multiple parts into one without affecting the functionality they achieve together. A designer could make use of such advantages to reduce assembly time.

d) Topology optimization: - Topology optimization is the modification of design of the part in such a way that it takes least amount of material to manufacture it without affecting its functionality. Such modification may result in organic shapes or lattice structures which could not be manufactured by conventional manufacturing processes. Ability of AM to print a part with lattice structures make it suitable for topology optimized designs.

Step 3: Selection and optimization of AM build parameters

Each AM technique has different settings that control the build process. For example, thermal extrusion printers have parameters such as extrusion rate and bed temperature. A detailed discussion of control parameter optimization for all seven AM methods is beyond the scope of this thesis. For further reading, the interested reader is referred to [11]. This work focuses on the L-PBF process. The basic control parameters for this process include laser speed, spot size, power, and scan pattern; layer thickness, dose factor, powder size and morphology; recoate blade speed and chamber atmosphere. These parameters must be optimized for each material system, and will further differ between printer make and model. Optimization of these parameters is a highly

iterative, non-linear process. This study uses parameters optimized by, and purchased from Concept Laser that will be discussed in detail in section 2.3.

Step 4: Sample removal and post-processing

After the build is complete, the build plate is transferred from the process station (build chamber) to the handling station where the excess, unmolten powder is removed and reclaimed. Typically, the powder is sieved for future reuse, although the number of times a powder can be recycled is limited [14].

The need for post-processing depends on the size of the part, the material, and the application. While a select few geometries do not require post-processing, many do. Some common post-processing steps are strain relieve anneals to mitigate thermal stresses that developed during the build process, HIP-ing to reduce porosity, polishing and etching to improve surface finish, and secondary machining to impart features, such as threads and contact surfaces, that are more amenable to subtractive machining. Other traditional post processing steps, such as beta-annealing Ti-6Al-4V [15] or solid solution/precipitation hardening of Inconel 718 [16], may also be added to the post-processing regimen to achieve application-specific materials performance requirements.

1.1.2. Applications of AM processes

Additive manufacturing finds application in various industries such as biomedical, aerospace, manufacturing, automotive, and architecture.

a) Biomedical: – The development of biocompatible materials for laser AM has enabled additively manufactured endoprostheses, and found successful application in knee, hip and spinal implants [17]. Because of its ability to print organic shapes and adapt to patient-specific requirements, L-PBF is also being used in prosthodontics and, orthodontics [18]. Although printing fully functional organs is far from reality, some success has been reported in the additive manufacture of cartilage, blood vessels, and skin in laboratories [19].

b) Aerospace: – Because of the ability to print light weight, high strength parts, additive manufacturing has found many applications in the aerospace industry. Electron Beam Additive Manufacturing (EBAM) has been especially successful, having been used to print aircraft frames,

jet engines and turbine blades [20] [21] and to reduce the manufacturing lead time for a spacecraft fuel tank by 80% [22].

c) Manufacturing: – Additive manufacturing is used for manufacturing dies with complicated and intricate designs that could not be manufactured by conventional manufacturing processes [23]. In the foundry and casting industry, lost cores and patterns of complicated designs can easily be made with AM without additional tooling [21].

d) Automotive – Additive manufacturing has been used in rapid prototyping in the automotive industry for a long time, but recently, stereolithography (SLA) has been used to produce interior parts such as light cases, speaker cases, and dashboard inserts. Additionally, L-PBF has been used to manufacture exhaust gas manifolds and engine parts [21].

e) Architecture – Architects have historically relied on wooden models and computer simulations to validate their designs. But now, with the advent of 3D printing technologies, scaled models can be printed to provide visualization of the actual design [24].

1.2. Inconel 718

Inconel 718 belongs to the family of superalloys. While the term superalloy does not have a strict definition in a technical sense, it is generally understood to be an alloy of nickel, cobalt and iron. Superalloys were invented as an extension of stainless steel technology to provide and maintain good performance in high-temperature applications. Initially, they were developed for gas turbine engine foils (GTE) around 1950 by Eiselstein [25].

Inconel 718 is known for its superior high-temperature performance and oxidation resistance [8], [25],[26]; it also possesses good fatigue and creep properties [27], [28]. Since its invention, Inconel 718 continues to be researched because of its flexibility and superior properties.

Inconel 718 is a precipitation hardened alloy. It precipitates out various phases such as γ'(Ni_3Al), γ'' (Ni_3Nb), δ (Ni_3Nb) and η (Ni_3Ti) at various temperatures during heat treatment, as shown in Fig 1.2, and all influence the mechanical properties of this alloy. γ' and γ'' are the important strengthening precipitates. δ and η phases are always incoherent with γ matrix and can only help in strengthening if they are present in small amount. And hence the influence of different types of precipitates on mechanical properties was studied [29], [30]. The impact of different

processing routes and heat treatments on mechanical properties is characterized [31], [32], [33]. The behavior and properties of Inconel 718 at different temperature ranges were quantified [8]. Hydrogen embrittlement and oxidation behavior were recorded [34] . Although Inconel 718 is extensively studied because of its widespread application in different industries, it has disadvantages. It is very difficult to machine Inconel 718 because of its low thermal conductivity. Machining of Inconel 718 often results in poor surface finish and tool wear unless the machining parameters are carefully chosen because of its work hardening effect. Researchers are continuously trying to characterize the work hardening behavior and find optimum cutting parameters for machining [35], [36], [37]. Because of these complications involved in machining, additive manufacturing became a favorable method to manufacture components using this alloy.

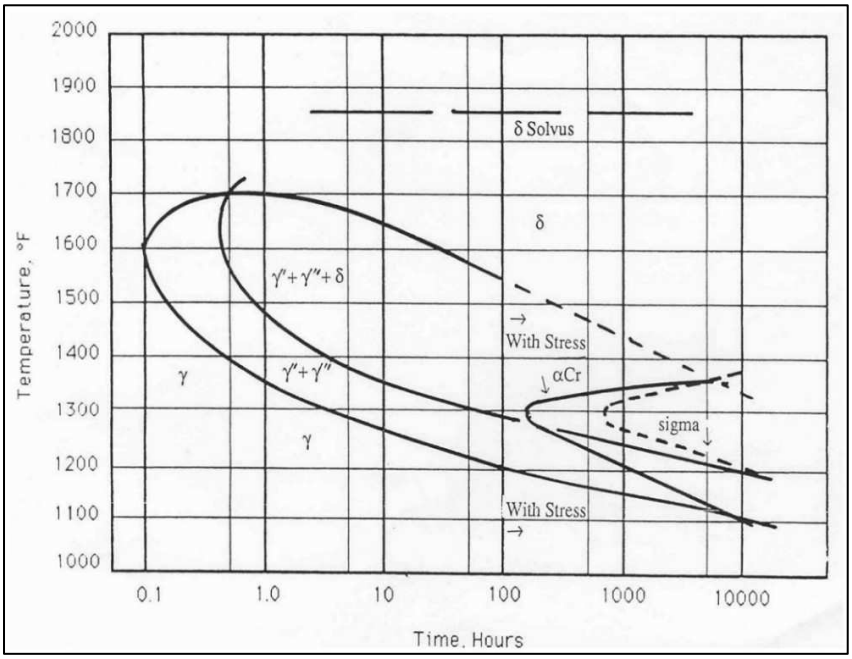

Fig. 1.2 TTT diagram of Inconel 718 alloy [38]
Copyright 1991 by The Minerals, Metals & Materials Society. Used with permission

Powder bed fusion processes such as Selective Laser Sintering (SLS), Direct Metal Laser Sintering (DMLS) and Selective Laser Melting (SLM) are being researched more, as these processes provides a combination of small feature size and reasonable build envelopes. Experimental investigation was conducted of the static and dynamic properties of additive manufactured Inconel 718 alloy, and modeling attempts were made. Much is already known about Inconel 718. Controlling phase formation and segregation through different laser modes and the

effect of interdendritic δ phase have been experimentally studied elsewhere [29], [39], [40]. The impact of microstructure, laser parameters and heat treatment on static mechanical properties of L-PBF fabricated Inconel 718 parts has also been experimentally investigated [41], [42], as have fatigue and creep properties [43]. Comparative studies of the microstructure and mechanical properties of cast, forged and L-PBF fabricated parts have been conducted [44]. A crystal plasticity model incorporating the effects of precipitates on compressive, tensile and cyclic deformation of DMLS fabricated Inconel 718 has been developed [45]. Thermal models and finite element simulations of Inconel 718 fabricated by laser powder bed fusion fabricated samples were developed and have been used by others [46], [47], [48].

1.2.1. Composition

The composition of Inconel 718 (UNS N07718) alloy is specified in Ref. [49]. The composition of Inconel 718 for additive manufacturing is given by ASTM F3055 – 14 a [50] is shown in Table 1.1. Like the wrought and cast alloy, Inconel 718 is a Ni-Cr-Fe alloy with intermetallic additions that precipitate strengthening cubic phases γ' ($L1_2$) and γ'' ($D0_{22}$)

Table 1.1 Composition of Inconel 718 in wt %

Elements	min	max
Ni	50	55
Cr	17	21
Fe		Balance
Nb	4.75	5.5
Mo	2.18	3.3
Ti	0.65	1.15
Al	0.2	0.8
Co	-	1

Elements	min	max
C	-	0.08
Mn	-	0.35
Si	-	0.35
P	-	0.015
S	-	0.015
B	-	0.006
Cu	-	0.3

1.2.2. Standard heat treatment for Inconel 718 alloy

In general, superalloys are strengthened by different mechanisms such as solid solution hardening, precipitation hardening, oxide dispersion hardening and carbide hardening. Inconel 718 is a precipitation hardened alloy. Precipitation hardening is dependent on the fact that some alloying elements have limited solubility in the matrix below a certain temperature. In the case of Inconel 718 alloying elements such as titanium, aluminum, and niobium precipitate out at reduced

temperature. Precipitates help in strengthening by restricting the movement of dislocation. Movement of dislocation is possible only by shearing through precipitates [51]. Precipitation hardening has the following steps.

Solution annealing

The temperature of the material is raised and held at a point until all the alloying elements such as aluminum, titanium, and niobium completely dissolve in the matrix. Then it is rapidly cooled (usually water quenched) to create a super saturated solution of the alloying elements [52].

Precipitation hardening

Further, the material temperature is raised to some intermediate level and held at that temperature for 8-10 h for the phases to precipitate out [52]

Two different commercial heat treatments are followed for Inconel 718 [49].

a) Solution anneal to 1700-1850 ° F then water quench and precipitation harden at 1325 ° F for 8 hours further furnace cool at 1150 ° F then age at that temperature for 18 h

b) Solution anneal to 1900-1950 ° F then water quench and then precipitation harden at 1400 ° F for 10 hours further furnace cool at 1200 ° F and then age at that temperature for 20 h

1.2.3. Applications of Inconel 718

Because of its superior corrosion resistance, high-temperature properties, and toughness, Inconel 718 is used in a wide variety of applications, such as the oil and gas industry, aerospace, and power plants.

a) Oil and gas industry

Inconel 718 is recommended by API standards for high-temperature applications where high H_2S output is expected. Therefore, it is used in several types of equipment, such as drilling tools, downhole equipment [31], [53], surface well heads, and Christmas tree equipment.

b) Aerospace

In the aerospace industry, Inconel 718 is used in various applications such as high-speed air frame parts, gas turbines, jet engines, exhaust manifolds and turbochargers.

c) Power plants

Directionally solidified Inconel 718 is used in power generation turbine blades for to allow for a higher operating temperature and improved efficiency [54]. Because of its high temperature corrosion resistance, it is also used in nuclear power plants.

1.3. Laser powder bed fusion

Laser powder bed fusion works by melting and fusing metal powders in a selected region layer by layer according to CAD model. This process was invented by Fockele and Schwarze of F & S Stereolithographietechnik GmbH, with Meiners, Wissenbach, and Andres of Fraunhofer, ILT [55]. At present, many companies, including EOS (Germany), Renishaw (UK), Concept Laser (Germany), SLM Solutions (Germany), Realizer (Germany), and 3D Systems (France/USA), produce printers using laser based powder bed fusion technology [11].

A schematic representation of an L-PBF printer is shown in Fig. 1.3. It has a powder supply piston and fabrication piston. The fabrication piston lowers by a distance of one layer thickness while the powder supply piston raises to supply powder for the build. A recoater blade spreads the powder over the build plate. Then a laser is used to locally melt the powder along a predetermined path. This cycle repeats until the complete three-dimensional part is built. Manufactured parts often have support structures, which are used to support parts during fabrication, and unmolten powder attached to their surface. After the build is complete the manufactured part is removed from the build plate, the support structure removed, and the part processed to achieve application-specific performance metrics. Unused powder can be stored for later reuse.

An L-PBF process that can produce near-net-shape, fully dense components with minimal post-processing is an area of active research in AM. L-PBF printed steel, nickel, and titanium alloys are commonly studied by researchers. Apart from these three alloys, materials like aluminum, copper, tungsten, and gold are also being studied [7] .

In a broader sense, research work performed on the L-PBF process can be classified into two groups. The first is experimental investigation of process-structure-property relationships, for example, studying the relationship between porosity and mechanical and fatigue properties of L-PBF printed parts. The second is numerical and finite element modeling (FEM) of the L-PBF process.

Initially, researchers attempted to study the densification, microstructure, and mechanical behavior of L-PBF printed parts. The goal of these research works was to find an optimal laser energy density that avoids balling phenomena and to study the microstructure of the L-PBF fabricated parts [42] [56], [57]. Subsequently, research work on the effect of build orientation on mechanical properties was investigated An initial investigation on grain texture and porosity of

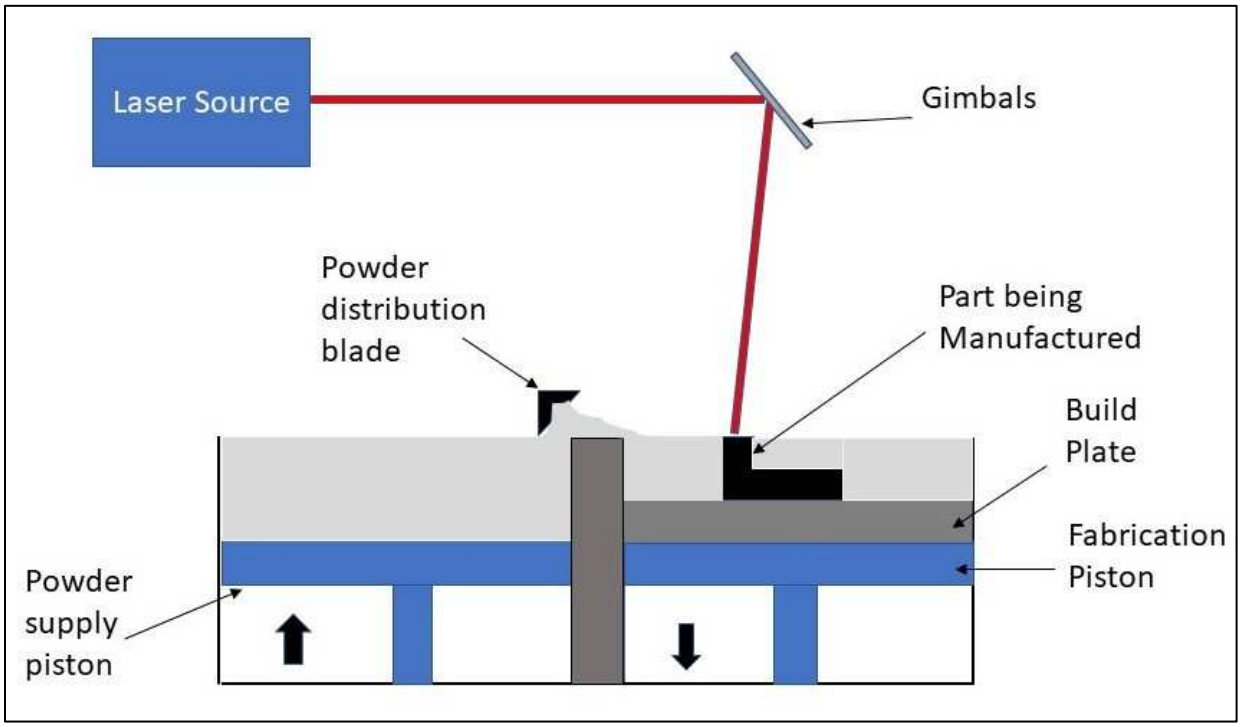

Fig. 1.3 Schematic representation of laser powder bed fusion (L-PBF) printer

L-PBF fabricated parts was performed [58]. Effects of heat treatment on microstructure and mechanical properties were studied [16] [59], as were high-temperature oxidation properties [60]. The influence of laser parameters—like scanning speed, power, overlap, laser scanning path—was also investigated [61], [62], [63], [64]; some researchers investigated the possibility of using the laser scan strategy and build orientation to tailor the texture of L-PBF printed parts [65]. Fatigue crack growth and the influence of different phases on fatigue crack growth were studied [43], [66].

Significant progress has been made on physics-based numerical modeling of the L-PBF process. A numerical model of L-PBF considering separate particles has been developed [67]. Numerical simulation of heat and mass transfer between powder particles was performed [68].

Finite element simulations of laser–particle interactions, considering optical penetration depth, were performed [46]. Finite element simulations were created to explain the thermal behavior of powder particles [69]. A crystal plasticity model, which includes the effect of precipitates, was developed to explain the compressive, tensile, and cyclic loading behavior of additively manufactured Inconel 718 [45].

1.4. Machine learning

Scientists try to explain observed, experimental phenomena based on theory and physics principles. Computational models simulate these phenomena to predict the behavior under a variety of conditions, and often at a fidelity not easily achievable with physical experimentation. And the complexity of some phenomena are currently intractable or prohibitively expensive. For example, computational modeling of the L-PBF additive manufacturing process is complicated, as it involves modeling a multiscale process. Melting and solidification of metal powders takes place in a few microseconds, and building parts take hours—very different time scales. This demands a coupled, multiscale model to create microstructure aware models [70]. Creating such a model requires a great deal of effort and computational efficiency. Thus, this research uses a data-driven modeling approach. Conventional mechanics and materials research involves creating computational models based on physics and validating the models through experimentation. Data-driven models operate in reverse. The model is created by using the available experimental data. Machine learning algorithms are at the heart of data-driven modeling. Programmers used to instruct the computer step by step through algorithms. But now computers can learn based on the data provided. In other words, with the help of machine learning algorithms, computers extract knowledge from the data we provide.

The concept of artificial intelligence was conceived in the 1950s when Alan Turing proposed his eponymous concept that we can claim a computer learns when humans interact with it and that there is no difference between human-human and human-computer interactions. In 1959, Arthur Lee Samuel of IBM developed a self-learning program that could play checkers [71]. He coined the term “machine learning.” Since then, machine learning algorithms have been formulated from five different schools of thought, according to Pedro Domingos in his book *The Master Algorithm*: symbolists, connectionists, evolutionaries, Bayesian, and analogizers [72].

On a broad basis, most of the machine learning algorithms can be classified into three different categories: supervised, unsupervised, and reinforcement learning algorithms [71].

a) Supervised algorithms

Supervised machine learning involves collection of known input values *x* and measured output values *y*, which can be collected through experimentation or observation. Then, based on these data, a function *f* is identified to predict the output values from arbitrary input. Regression algorithms are used to predict continuously variable output; classification algorithms are used when the output takes discrete values [73].

b) Unsupervised algorithms

Instead of finding relationships between input and output variables, unsupervised algorithms find relationships between input variables. Clustering algorithms, which work by grouping variables based on their distance in the multidimensional input space, and dimensionality reduction techniques, like principal component analysis, are examples of unsupervised algorithms [74].

c) Reinforcement learning

In reinforcement learning algorithms, the model updates every time new data are provided. It has a feedback mechanism that allows the algorithm to update itself based on every new datum to improve prediction. Examples are the upper confidence bound algorithm and Thompson sampling [75].

1.4.1. Machine learning in materials science and manufacturing

Because machine learning models depend only on data, relying on the intrinsic connection between the data and the underlying science/physics, they have been successfully used in many different sectors, including materials science and manufacturing. Commonly used machine learning algorithms in materials science and manufacturing are listed in Fig. 1.4 [76].

In materials science, machine learning algorithms have been used in both microscopic and macroscopic property prediction and in crystal structure prediction [76], such as the crystal structure of cathode materials in Li-ion batteries [77]. Density functional theory has been used

along with machine learning to predict the properties of materials [78], [79]. Microstructural images have been identified and classified successfully using machine learning techniques [80]

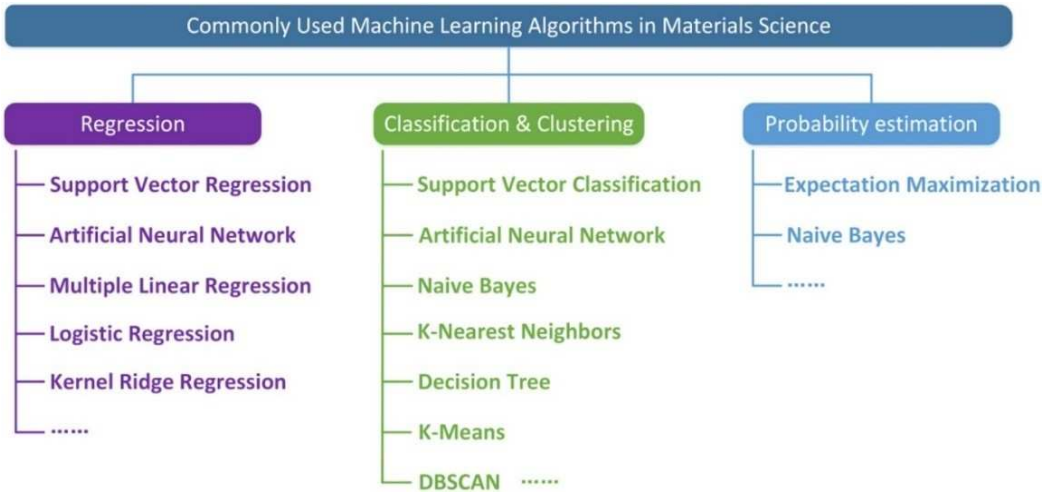

Fig. 1.4 Commonly used machine learning algorithms [76].
Reproduced under license CC BY-NC-ND 4.0

Machine learning techniques had been successfully used in the prediction of mechanical properties of parts manufactured through conventional manufacturing processes. They were used to predict mechanical properties of castings in foundries, surface roughness in CNC machining, and mechanical properties of concretes. Because a huge number of variables are involved in determining the ultimate strength of castings, physics-based models could not be developed. Castings were qualified based only on destructive testing. With the help of machine learning algorithms, models were developed to predict the ultimate strength of castings. Various classification algorithms were used to predict the ultimate strength of cast parts in foundries [81]. Extreme learning machine (ELM), an artificial neural network (ANN)-based algorithm, was used to predict mechanical properties of hot rolled products. Many variables like cutting speed, feed, tool angle, cutting fluid, and material hardness are involved in determining final surface roughness of a part in CNC machining. Because of complications in developing physics-based models, machine learning models were used to predict the final surface roughness. ANN coupled with a genetic algorithm was used to predict and optimize CNC machining parameters for surface roughness [82]. The performance of various machine learning algorithms in predicting mechanical strength of cork under compression was evaluated [83]. A support vector machine (SVM) classification algorithm was developed to successfully classify the mechanical property data set of

a large vapor-grown carbon nanofiber (VGCNF)/vinyl ester (VE) nanocomposite. Machine learning models helped eliminate costly experimentation involved in determining concrete strength. ANN and support vector regression (SVR) models showed superior performance in predicting the splitting tensile strength of plain and steel fiber-reinforced concretes [84].

All these examples show that machine learning is efficient in predicting the output, or at least a range of possible outputs, for a given set of processing conditions when a large number of input variables are involved. Although additive manufacturing processes involve many input variables such as printing orientaion, printing location, laser power, laser speed, spot size, and overlap in determining output mechanical properties, very few attempts have been made to make use of machine learning in additive manufacturing.

1.4.2 Machine learning models used in this research.

Regression and classification algorithms have been used to model the variations in mechanical properties of additively printed parts in this research work. All machine learning models used in this research work are explained as follows.

a) Decision trees

A decision tree is a supervised learning algorithm that works by developing a set of rules based on the training data fed into the algorithm and making decisions based on those rules. Decision trees can be implemented into both classification and regression algorithms. Classification algorithms perform the split based on an impurity measure. Let us say N_m number of training instances reach node m [85]. N_i be number of instances classified as class C_i. Estimate of probability (P) of an instance belongs to a class C_i is

$$P(C_i|N_m, m) \equiv p^i = \frac{N_i}{N_m} \tag{1.1}$$

The node m is pure if all the instances reaching that node belong to class C_i or all instances do not belong to class C_i. If the split is pure, the tree does not need to be split further. If the split is impure, entropy is used to measure the impurity of a split using the formula [85]

$$I_m = -\sum_{i=1}^{k} p_m^i \; log_2 \, p_m^i \tag{1.2}$$

Where p_m^i is the ratio of number of instances classified as class C_i at node m to total number of instances reaching the node m and k is number of classes. A regression tree is very similar to a

classification tree except that the impurity measure is the mean squared error of the predicted value and the estimated value [85].

b) Random forest algorithm

The random forest algorithm is a supervised machine learning algorithm built based on the decision tree algorithm. The difference is that instead of relying on one decision tree, the random forest algorithm builds multiple decision trees based on selected input parameters from the complete set of input parameters fed to the algorithm. Output from all the decision trees are compared and the best output is chosen on a vote basis [86].

c) Support vector machines

Support vector machines are also supervised machine learning algorithms that work by finding the best hyperplane that separates multiple classes of data in a n-dimensional space. It is usually implemented in a classification algorithm, but it could also be implemented in a regression algorithm. For detailed mathematical implementation the reader can refer to Ref. [87].

d) Kernel ridge regression

Kernel ridge regression applies a kernel function to map the input data into a space where it can perform linear regression between input parameters and output, whereas the relationship between them is nonlinear in the original space. Several different kernel functions like linear, polynomial, and Gaussian kernels can be used in modeling. Kernel ridge regression is based on ordinary least square and ridge regression. Let X be feature matrix of arbitrary size N × d. Y is the output vector, and the kernel ridge regression is used to find the solution to the problem [88], [89]:

$$\min_{\beta} ||Y - X\beta||^2 + \gamma||\beta||^2 \tag{1.3}$$

where γ is the ridge parameter to control trade-off between bias and variance. The closed-form solution for the above problem is $\beta = (X^T X + \gamma I)^{-1} X^T Y$ where I is the identity matrix. The predicted output is given by $\beta^T X$ [89].

e) K nearest neighbor classifier

K nearest neighbor classifier is the simplest supervised machine learning algorithm. It works by guessing the class of an unknown instance based on the class of most neighboring

instances. Number of neighbors are chosen by user. Many different distance measures are used to find the nearest neighbors. For this work Euclidean distance measure shown in equation 1.4 was used

$$\sqrt{\sum_{i=0}^{i=n}(A_i - B_i)^2} \tag{1.4}$$

where A and B are two points in n-dimensional space.

f) Naïve Bayes Classifier

The Bayes classifier works based on the Bayes theorem mathematically represented as shown in equation 1.5. It assumes that every input parameter affects the output independently and there is no interdependent variation.

$$P(A|B) = \frac{P(B|A).P(A)}{P(B)} \tag{1.5}$$

P(A|B) is a conditional probability—the probability of event A occurring given B. It is also called posterior probability.

P(B|A) is also the conditional probability—the probability of event B occurring given A. It is also called likelihood.

P(A) and P(B) are probabilities of observing A and B. They are also called marginal probability.

1.4.3 Validation of models

K-fold cross-validation is used to validate the regression models and stratified *K*-fold cross-validation is used for classification algorithms.

a) *K*-fold cross-validation

In *K*-fold cross-validation the entire data set is divided into *k* different subsets (in this work, 10). $k-1$ subsets are used in training the algorithm and the remaining part is used for validation. This procedure is repeated with all *k* parts of the data withheld in turn as the validation set, and the accuracy reported as the average over all iterations.

b) Stratified *K*-fold cross validation:

Stratified *K*-fold cross validation is applied to classification algorithms in a procedure that is very similar to *K*-fold cross validation. When the different classes do not have an equal number of samples, the data set is divided into *k*-different parts so as to maintain the percentage of each class in every fold.

1.4.4 Metrics used

For measuring performance of regression algorithms, the mean absolute error was used as the metric; precision, recall, f1-score and accuracy were used in measuring performance of classification algorithms.

a) Mean absolute error:

Let Y_t be a one-dimensional vector of test data that contains n elements, and Y_p be another one-dimensional vector that contains the corresponding predicted data. Then mean absolute is

$$\sum_{i=1}^{i=n} \frac{||Y_t(i) - Y_p(i)||}{n} \tag{1.6}$$

b) Metrics used for classification algorithms:

Metrics used for measuring performance of classification algorithms are derived from the confusion matrix. A confusion matrix helps in visualizing the performance of classification algorithms. Confusion matrix terminology is shown in Table 1.2.

Table 1.2 Confusion matrix based on actual and predicted values

	Predicted Yes	**Predicted No**
Actual Yes	True Positive (tp)	False Negative (fn)
Actual No	False Positive (fp)	True Negative (tn)

All the metrics used for measuring performance of classification algorithms are given in Table 1.3. Performance of classification algorithms could not be measured by just one algorithm as the measure would be biased. So, four different metrics were used for measuring the

performance of classification algorithms. They are recall, precision, F-1 score and accuracy. All the metrics are derived from the confusion matrix described in the Table 1.2.

Table 1.3 Metrics used for measuring performance of classification algorithms. The abbreviations are defined in Table 1.2.

Metrics	Formula	Definition
Recall (R)	tp / (tp+fn)	The ratio of positive samples correctly classified
Precision (P)	tp/ (tp+fp)	The total number of positive samples correctly predicted from all positive samples
F1-Score	2*P*R/ (P+R)	The harmonic mean of precision and recall
Accuracy	tp+tn/ (tp+tn+fp+fn)	The ratio of correct predictions over total number of predictions

1.5. Objective of this thesis

Conventionally, metallic parts are manufactured through materials fabrication processes, like forging and casting, followed by one or more machining processes, like turning, milling, and drilling, to remove unwanted material and provide the final shape and dimensions. Methods to control the properties of parts manufactured by conventional processes are well understood and consistent. There are a large number of variables involved in the additive manufacturing process, each of which can affect the mechanical properties of the final part. This thesis is an investigation into the reasons for inconsistencies in the L-PBF part properties. In L-PBF, these variables include the orientation of the part; the location of the part on the build plate; laser power, speed, spot size, and overlap; powder size; layer thickness; etc. This work seeks to understand the impact of part build orientation and location of the part on the build plate on the mechanical properties of L-PBF printed parts. The impact of post-processing activities, like machining and heat treatment, on their mechanical properties is also analyzed. Machine learning algorithms are used to understand the sources of variability in the mechanical properties.

a) Characterizing the variation of compressive, tensile, and hardness properties with respect to build orientation and location of samples on the build plate (Chapter 2).

A fair amount of research has already been conducted on studying the microstructure and mechanical properties of L-PBF printed Inconel 718. Some of the earlier research work conducted was concentrated on the characterization of microstructure and mechanical behavior, and on

improving or comparing the as-built mechanical properties with a subsequent process, like hot isostatic pressing (HIP) and annealing [17], [90]. Anisotropy caused by build orientation was not considered in those works. Subsequent attempts focused on optimizing laser parameters, such as laser power and laser scanning speed, to manufacture fully dense parts [42],[91]. An attempt has been made to characterize the microstructure and tensile properties of L-PBF printed Inconel 718 in the as-built condition and to compare it with heat-treated samples. Existing work has also considered orientation effects [16]. Tensile properties were measured after CNC machining the printed parts. Although CNC machining was performed to maintain the sample-to-sample uniformity or to comply with a standard geometry, machining modifies the surface morphology of the L-PBF printed part completely, removing the unmolten powder and the porosity, which is mostly concentrated towards the outer periphery (~200 μm shell from outer diameter). Characterizing the parts with all the adverse characteristics of the process is important to understand the process without affecting the sample through the changes that inescapably occur during post-processing. Therefore, in this research, samples in the as-built condition were characterized without any post-processing or machining except removal of the support structure. Challenges in characterizing the samples in the as-built condition are discussed. Distribution of powder across the build plate varies depending on the flowability of the powder. The orientation of the laser also varies based on the location of the sample on the build plate. Hence, the variation of properties with respect to location needs to be studied. To the best of the author's knowledge, no previous work has been reported on characterizing the variation of mechanical properties with respect to the location on which the sample is printed on the build plate.

b) Characterizing the influence of post-processing activities such as machining and heat treatment on compressive and tensile properties (Chapter 3).

As an extension of the previous objective, the mechanical properties are characterized after machining and compared with properties of the as-built samples and connected to previous research works. Popovich et al. have discussed the variation of tensile properties of the as-built sample and heat-treated samples (homogenization + aging) at 20 °C and 1000 °C without considering effects of orientation [92]. Fabrizia Caiazzo et al. have characterized the tensile properties of heat treated samples (solution annealing + aging) at room temperature and 650 °C. Three different build orientations were studied in this work, but they were not compared with the

as-built properties. E. Chlebus et al. characterized the difference in tensile properties from the as-built condition to four different heat-treated conditions. This work considered four different build orientations [16]. Still, more efforts are needed to characterize the effect of heat treatment because most previous studies were performed with cylindrical tensile samples with thickness around 4 mm. In samples of such thickness, the contour laser settings, which are used to scan the outer periphery (200 μm) of each part, would have much less effect on the final properties. In this research work, flat sub-sized tensile samples of 2 mm thickness, as described in ASTM E8/E8M [93], were used to characterize tensile properties. The effect of contour laser settings on the final properties are more pronounced on thinner samples. Tensile samples were built in twelve different build orientations, and compressive samples were built in nine different orientations to study anisotropy effects extensively. Also, most of the previous research work reported tensile properties and not compressive properties. Considering that Inconel 718 alloy exhibits tensile/compressive asymmetry in mechanical properties [94], [95], characterizing compression properties are also important. Also, effects due to printing location and porosity were not considered in previous studies. This research work addresses those knowledge gaps in the literature.

c) Modeling the variation of mechanical properties of L-PBF printed Inconel 718 with respect to position and orientation using machine learning models (Appendix A).

Although machine learning models have been used to predict material properties and determine optimum machining parameters for a long time, as described in section 1.4.1, the possibility of using them to predict the properties of additively printed metals has not been researched extensively. In recent work published by G. Tapia et al., a Gaussian Process Regression (GPR) model was used to predict the porosity using process parameters [96]; however, no attempt has been made to predict the mechanical properties of additively printed parts using machine learning models. In this research work, preliminary attempts have been made to model the variation of mechanical properties with respect to position and orientation of additively printed samples using machine learning models.

CHAPTER 2

EXPERIMENTAL METHODS

The influence of part orientation, position, and post-processing activities such as machining and heat treatment of L-PBF printed Inconel 718 alloys on mechanical properties were investigated. For this investigation, four different build plates (two each of compression and tensile samples) were printed, as shown in Fig. 2.1. Samples from one of each of the compression and tensile plates were removed and analyzed in the as-built condition. The other plates were subjected to solution annealing and double aging heat treatment before sample removal. All mechanical testing was carried out using the digital image correlation (DIC) technique. Some compression samples were machined from a 2 mm nominal diameter down to 1.5 mm nominal diameter. All compression samples were scanned using X-ray computed microtomography to characterize porosity. Hardness tests were conducted with some compression samples in both the as-built and heat-treated conditions.

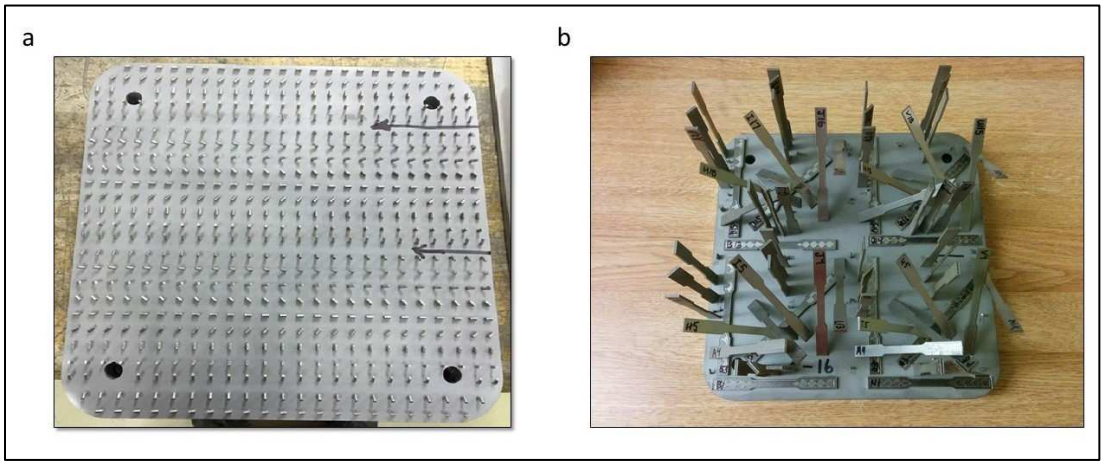

Fig. 2.1 a) Compression build plate and b) tensile build plate in as-built condition

2.1. Experimental method

The sample dimensions and build plan in this experiment were designed to understand how properties of a sample vary with respect to its size, orientation, and location on the build plate. Compression samples and tensile samples printed in different orientations and in various locations were subjected to mechanical testing. Additionally, compression samples were scanned through

X-ray CT to understand the formation of defects and porosity and their influence on mechanical properties.

2.1.1. Sample dimensions

Both compression and tensile samples were printed on build plates of dimensions 247 mm x 247 mm made out of P-20 tool steel. Tensile samples were ASTM E-8 [93] subsized tensile specimens of dimensions shown in Fig. 2.2a. This geometry allows at least four samples of each orientation to be built in various locations.

Compression samples were cylinders of 2 mm diameter and 4 mm length. This is the largest dimension for an Inconel 718 specimen that can be scanned through tomography. Smaller samples would have properties more sensitive to overbuilds, unmolten powder, and porosity. So, the dimensions of the compression samples were intentionally made small to catch variations caused by the above mentioned adversities.

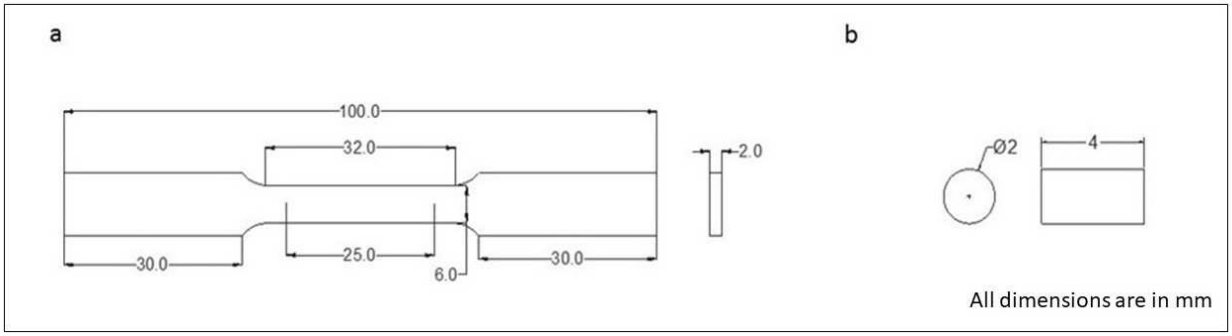

Fig. 2.2 a) Tensile sample dimensions b) Compression sample dimensions

2.1.2. Printing orientation

Two different types of orientations were assumed to influence the mechanical properties of the samples. They were polar orientation and azimuthal orientation of the sample, herein referred to as ϕ and θ, respectively. Polar orientation (ϕ) is the orientation of the sample with respect to the normal of the build plate, and azimuthal orientation (θ) is the orientation of the sample with respect to the swiping direction of the blade. Fig. 2.3 depicts polar and azimuthal orientation of compression samples. Orientation of tensile samples is explained in Fig. 3.9 in Chapter 3.

The laser direction and build direction influence heat flux through the sample during the L-PBF process. Grains have been shown to grow in the direction of the heat flux [16]. As the direction of heat transfer to the substrate changes with polar orientation of a part, so does the resultant heat flux direction. So, it is expected that texture and mechanical properties change with polar orientation (ϕ) and azimuthal orientation (θ).

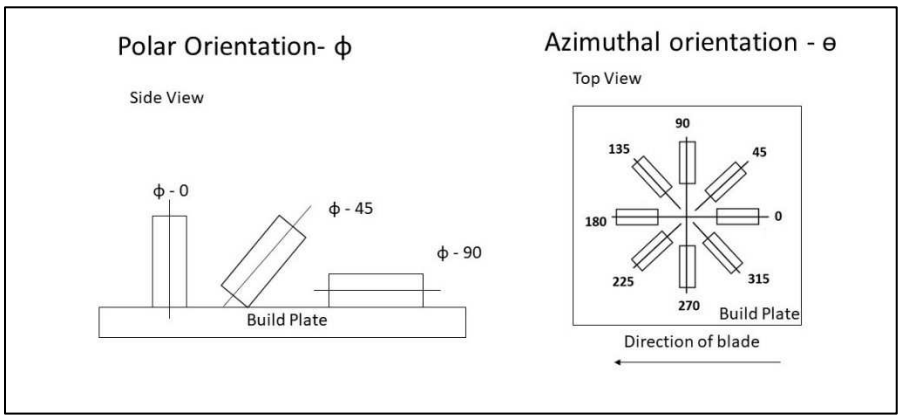

Fig. 2.3 Two different types of orientations

Samples were printed in three different polar orientations, $\phi = 0$, $\phi = 45$, and $\phi = 90$, and their mechanical properties were studied so that properties of samples at other polar orientations could be interpolated from these three orientations. The laser scanning path changes for a part with respect to azimuthal orientation, and hence, mechanical properties are also expected to change. So, the variation of properties with respect to azimuthal orientation was also studied.

2.1.3. Build plan (compression samples)

In total, nine unique (ϕ, θ) orientation combinations (Table 2.1) were studied in compression samples. With 10 mm (can be modified) separation between compression samples, approximately 600 samples can be printed on a build plate. But if all 9 orientations are printed in all 600 possible locations on a build plate, a total of approximately 5,400 samples should be printed on 9 different build plates just to study properties in the as-built condition. So, to reduce the number of samples, twenty-five samples of the same orientation were printed in each row to study the variations of properties along the x-axis. To study variation of properties along the y-axis, all orientations were printed thrice on the build plate, except for two orientations [($\phi = 45$, $\theta = 0$), ($\phi = 45$, $\theta = 270$)], which were printed only twice because of space constraints, as shown in Fig. 2.4.

Table 2.1 Combinations of orientations of compression samples

No	1	2	3	4	5	6	7	8	9
ϕ	90	90	90	0	45	45	45	45	90
ɵ	0	45	90	0	90	270	180	0	135

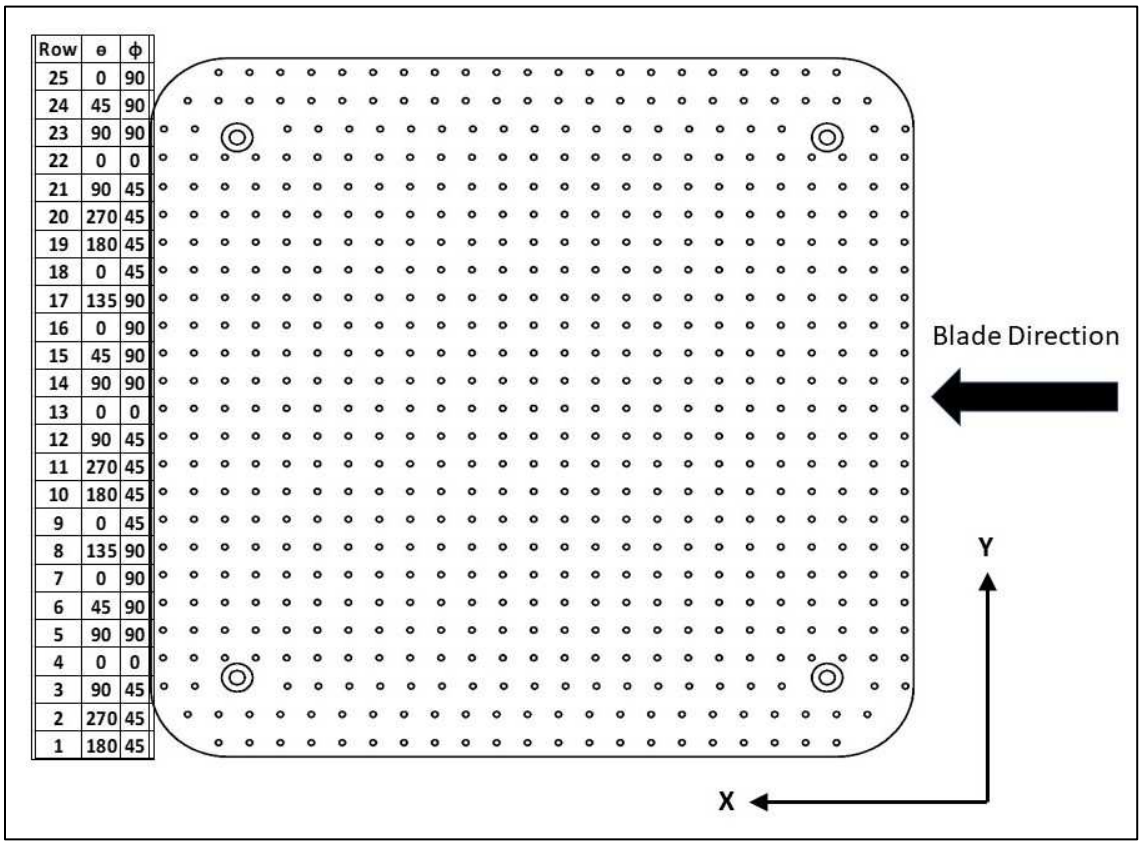

Fig. 2.4 Schematic representation of samples on compression build plate

2.1.4. Build plan (tensile samples)

In total, 12 unique (ϕ, θ) orientation combinations (Table 2.2) of the tensile specimen were printed on the build plate. At least four samples of all orientations were printed on the build plate. Samples where ϕ = 0 were printed in greater number in several different locations to understand if the properties change with respect to their distance from the laser source. In total, 68 tensile samples were printed on the build plate, as shown in Fig. 2.2. A pictorial representation of all these orientations is given in Fig. 3.8 in the next chapter.

Table 2.2 Combinations of orientations of tensile samples

No	1	2	3	4	5	6	7	8	9	10	11	12
ϕ	0	0	0	0	45	45	45	45	45	90	90	90
ɵ	0	45	90	135	0	90	180	270	315	0	45	90

2.2. Powder and Printer

Gas atomized Inconel 718 powders with a particle size in a range of 10–45 µm purchased from Concept Laser were used as printing material in this study.

Table 2.3 Technical specifications of the printer

	Build Chamber	**Powder Chamber**
Dimensions (L x W x H) in mm	250 x 250 x 280	250 x 250 x 280
Volume in dm^3	Approx. 18	Approx. 18
Design height in mm (minus build plate thickness)	Max. 280	
Exposure field in mm	245 x 245	

All samples for this research work were manufactured with a Concept Laser M2 Dual Laser with the specifications shown in Table 2.3. It used the selective laser melting process for printing samples. This is a dual laser printer that uses two 200W fiber lasers. The basic parameter editor, which was used in this process, provides independent control over the laser settings for four contextual build regions: advanced contour, contour, skin, and core laser settings. The laser settings are unique combinations of laser power, speed, spot size, and overlap. Laser power speed and spot size control the power density. The overlap refers to that of adjacent laser tracks. Advanced contour and core laser settings are used only in printing parts more than 10 mm in thickness on the surface normal to build direction. So, they have no significance relevant to this research. Only two different laser settings named contour and skin settings were used in printing the samples. They are explained as follows. Both contour and skin laser settings use power of 160 W and speed of 800 mm/s. They differ only by spot size. The contour laser setting uses 50 µm spot size, and the skin laser setting uses 80 µm spot size. The contour laser setting with the smaller spot

size was used in scanning the outer contour of the samples for a better surface finish and dimensional accuracy.

Fig. 2.5a shows a metallography of a compression sample ground to 1 mm, etched, and polished to show areas scanned by contour and skin laser settings. Fig. 2.5b is a schematic showing contour and skin laser settings. There was 0.16 mm of overlap between the contour and skin regions of the samples. The build chamber was sealed and maintained in an argon atmosphere to establish an oxygen concentration below 0.61%. The temperature of the build chamber was maintained between 70 and 80 °F and relative humidity was maintained between 6 and 18 %.

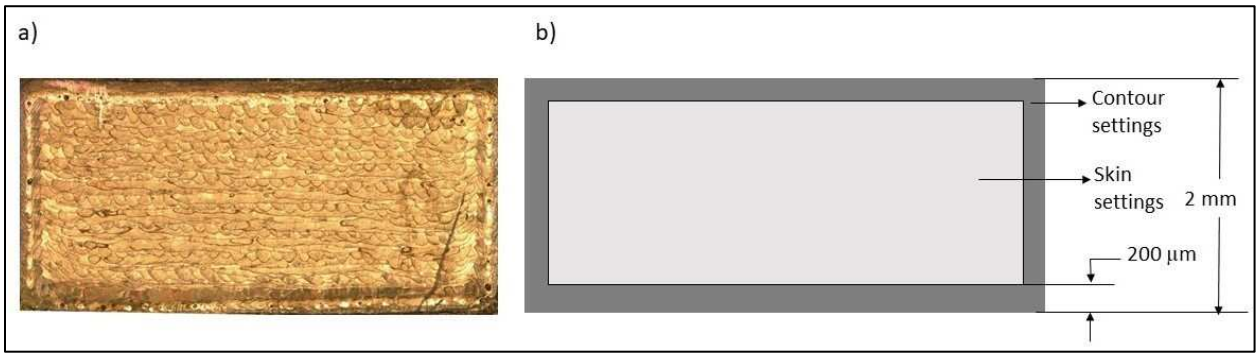

Fig. 2.5 a) Metallography and b) schematic showing contour and skin laser setting.

2.3. Porosity characterization using X-ray computed tomography

X-ray computed tomography (CT) is a nondestructive imaging technique that allows us to see through the internal structures of an object without cutting it. To obtain a three-dimensional tomographic image of an object, it is irradiated with X-rays or gamma rays, and a series of two-dimensional projections are obtained at various angles. The projections are used to reconstruct a three-dimensional image.

A schematic representation of the X-ray CT scanning process of a compression sample is shown in Fig. 2.6. A sample is set in the path of a high-energy X-ray beam, and the intensity variations in the beam passing through the sample are recorded by a detector. The intensity of the beam passing through thicker metal varies from a porous metal, which enables us to detect porosity in samples. Projections are taken as the sample, mounted on the turn table, is rotated through a small angle. The process is continued until the sample is rotated through 360 degrees. Zeiss

reconstruction software uses these two-dimensional images to produce a three-dimensional tomography.

For this research, CT scans were performed in a Zeiss Xradia Versa 520 that uses a tungsten target and an adjustable accelerating voltage of 30–160 kV to generate divergent, white beam X-rays. At an operating voltage of 160 kV and current of 62.5 μA (10 W), the spot size for this source was approximately 5 μm and could image the cylindrical Inconel 718 test coupons at a spatial resolution of approximately 4.5 μm. Every compression cylinder of diameter 2 mm x length 4 mm was scanned through 360° to obtain 1601 projections. The magnification was set by the source–sample (a) and sample–detector (b) distances, shown in Fig. 2.6, and the optical magnification ($m_{optical}$). The total magnification is the product of the geometric and optical magnifications:

$$M = m_{\text{optical}} \times m_{\text{geometric}} = 0.4 \times \frac{a+b}{a} \tag{2.1}$$

where a is ~15 mm and b is ~270 mm. This provides a field of view (FOV) of approximately 4.5 x 4.5 mm.

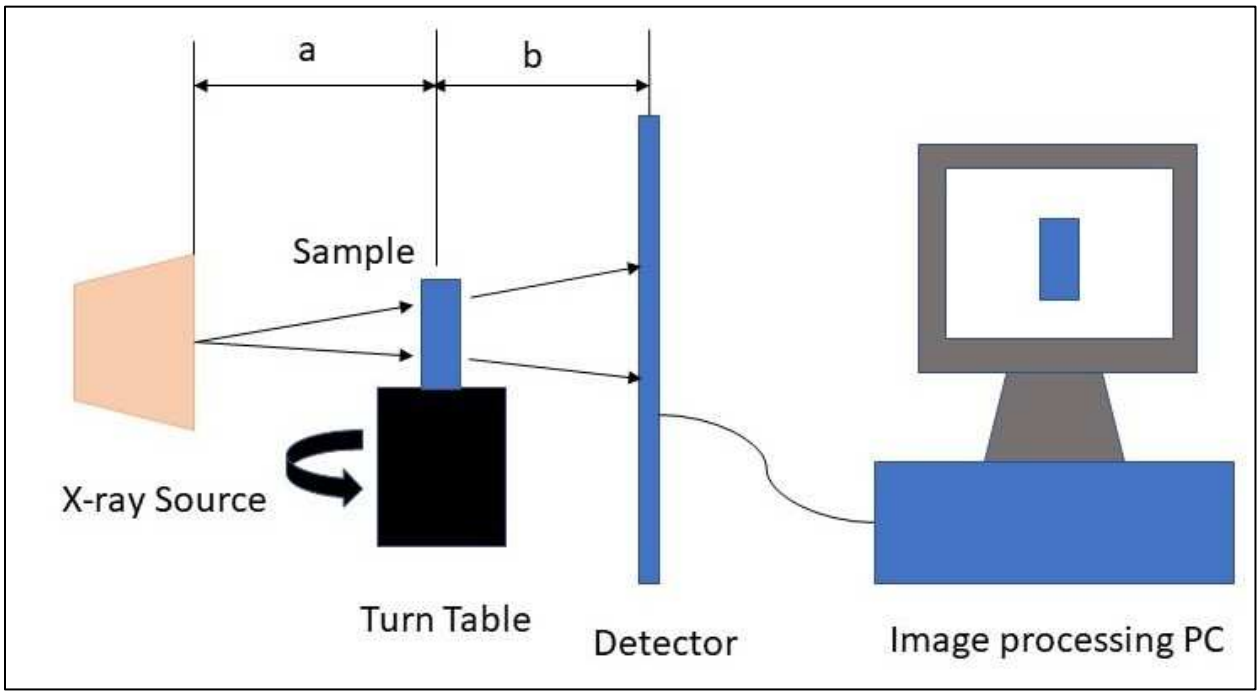

Fig. 2.6 Schematic representation of X-ray CT scan

Three-dimensional images generated from CT scans were processed using TRACR, an algorithm developed by Henry Geerlings of Colorado School of Mines for his thesis work entitled "High throughput porosity characterization using TRACR," which is to be published in May 2018 [97]. TRACR characterizes porosity in the sample by differentiating volumes of metal from porosity in each sample. TRACR can compute the volume of all pores in the sample irrespective of shape or size of the pores and can provide volume fraction of porosity. Pore diameter is calculated assuming that all pores in the sample are spherical. Further, statistics of the pore distribution are computed: mean pore diameter, median pore diameter, mean pore spacing, and median pore spacing. In this work, the effect of maximum pore diameter and porosity volume fraction on mechanical properties were studied.

2.4. Digital image correlation (DIC)

Digital image correlation (DIC) is a noncontact optical technique to measure displacement and compute strain from displacement [98]. DIC works by tracking a group of pixels in digital images of the surface of the sample being tested taken at different stages of deformations and building up a strain map [98]. This technique has been widely adapted and successfully implemented in many experimental mechanics research works [99].

The image area captured in DIC provides a full two-dimensional strain map, and thus, a more complete picture of the strain field than the one-dimensional length-averaged and localized strain measured by extensometers and strain gages, respectively. The addition of a second DIC camera to the first provides stereo, or 3D-DIC, that adds out-of-plane deformation to the in-plane deformation field collected from 2D-DIC. In general, digital image correlation is a three-step process: sample speckling, recording images, and processing images [100].

Digital image correlation tracks surface deformation by tracking morphological changes of high-contrast surface patterns, for example, black spots on a white background. If no such pattern occurs naturally, black and white colored paints are used to create a speckle pattern.

Two important parameters called facet size and step size are involved in determining the computing time and accuracy of strain computed by DIC software. Software tracks the deformation by groups of pixels called facets. Facet size is measured in terms of pixels. It is a subset of pixels, and in this work, 25 x 25 pixels are chosen as the facet size. The facet size of the

images is adjusted per the speckle size, and the speckle size is chosen per the sample size tested. The aim is to obtain at least three different color changes along each edge of the facet, as shown in Fig. 2.7a. Every facet functions as a point of strain measurement for DIC. Step size, which is also measured in terms of pixels, helps resolve the facets. Step size is the number of pixels in the overlapping area along each corner of the facet.

To acquire accurate strain measurements with a Field of view (FOV) of 5 x 4 mm, the features of the speckle pattern must be approximately less than 10 µm. To achieve these dimensions, compression sample speckle patterns were created with black Createx air brush color base and speckled with aluminum oxide powder (less than 10 µm average size) mixed with acetone and sprayed with an Iwata HP-BC1 air brush to create a nonreflective surface.

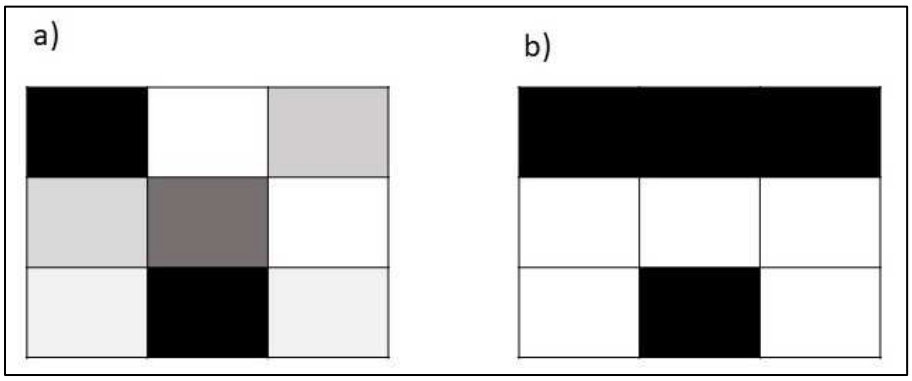

Fig. 2.7 Examples of a) good speckle pattern and b) bad speckle pattern.

An analogous technique was used for tensile specimens. The FOV larger than the compression samples required a commensurately larger speckle feature, approximately 40-50µm. A uniform white background was applied with Krylon® spray paint. The foreground was applied by wafting the sample through an aerosolized mist of black Krylon® spray paint.

Series of images were recorded at a predetermined frequency while load was applied to the sample. The images were acquired at a rate of 1 image per second, and load data was acquired at 10 data points per second. The load data is down sampled to match the image acquisition rate. In 2D-DIC, one camera is placed normal to the surface of the sample to capture the images. If the deformation being measured is strictly planar, then 2D-DIC is preferred for its ease of setup; however, the presence of out-of-plane motion leads to defocusing that makes 2D-DIC data unusable. To understand the properties of additively manufactured parts, a majority of the

compression samples were tested in their as-built condition. However, nonparallel ends caused by overbuild or residual support material present on these parts can result in shear (out-of-plane motion), so 3D-DIC was required to track the complex compressive deformations observed during testing of the as-built parts.

Strain fields were calculated from the DIC images using commercial software, e.g., ARAMIS®, VIC 3D®, or NCORR®. In this work ARAMIS software was used to compute strain.

2.5. Compression Testing

Compression testing was conducted on a Mark 10 ESM1500 load frame equipped with a 10 kN load cell and YTZP (Yttria Stabilized Zirconia) compression platens. The load frame was aligned to less than 20 με of bending strain. A molybdenum disulfide coating was used to reduce friction between the sample and platens. All tests were performed under displacement control at a 0.24 mm/min displacement rate, approximately equal to a strain rate of 10^{-3} s^{-1} for a 4 mm tall cylindrical compression sample.

DIC setup for compression testing is shown in Fig. 2.8a. For performing stereo DIC, two Baseler acA640–750 μm cameras were positioned at an angle of 25° to the normal direction of the surface of the sample being tested, as shown in Fig. 2.8b. Schneider Unifoc-12 lenses (P/N 25-014780) were used in a forward configuration to achieve the required working distance (the distance from the sample to the front face of the extension tube), as shown in Fig. 2.8b. Extension tube length of 130 mm was used with a working distance of 120 mm to achieve a field of view of 5 x 4 mm. This setup was calibrated against a 5 x 4 mm GOM optical calibration target. High-intensity LEDs were used to illuminate the sample. As DIC only requires black and white images, red filters were used to enhance the image contrast. Linear polarizers were used to eliminate unwanted reflected light and obtain a reflection-free image.

Strain computations were performed in ARAMIS 6.3.1 using a facet size of 25 pixels and a step size of 13 pixels for all the strain computations. Stereo digital image correlation captured full 3D strain surface information; furthermore, with ARAMIS software, uniaxial strain could be separated from other strain.

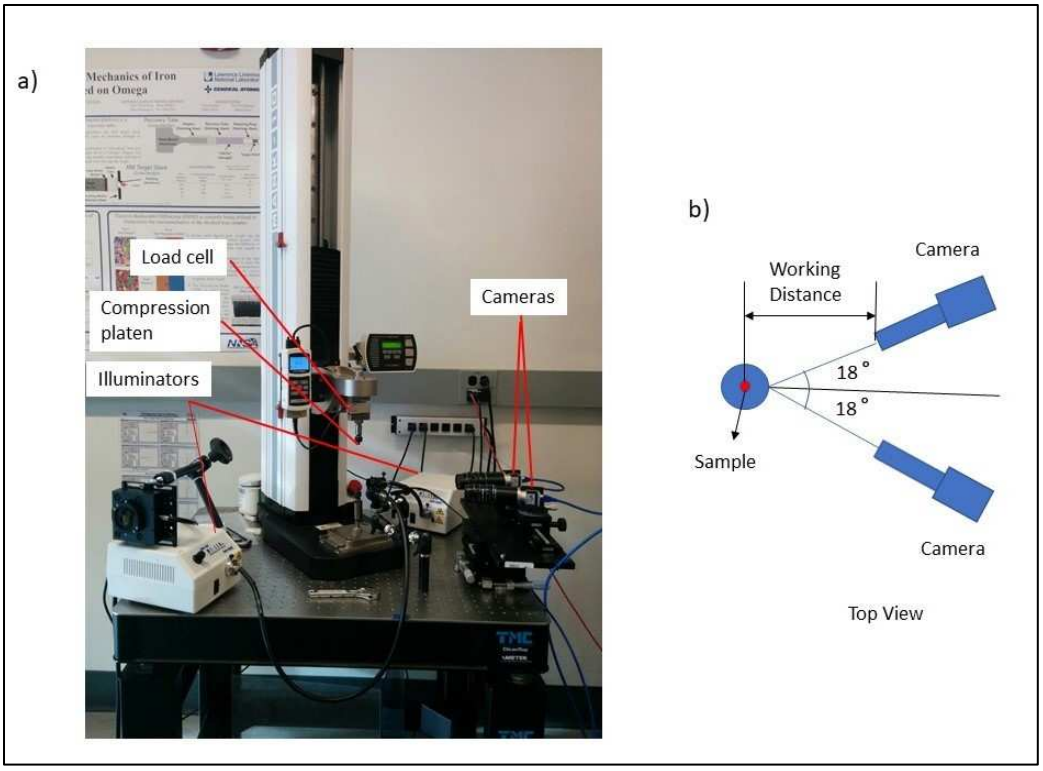

Fig. 2.8 a) DIC set up and b) camera angle and position for compression testing

2.6. Tensile Testing

All tensile testing for this work was conducted on an MTS 370.02 model load frame using a 25 kN load cell aligned to less than 20 με bending strain. Hydraulic wedge grips with diamond pattern grip faces were used to hold the test specimens. Displacement of the load frame was controlled to impart an approximate strain rate of 10^{-3} s^{-1} .

The DIC setup for tensile testing is shown in Fig. 2.9a. For performing stereo DIC, two Baseler acA2500–14 μm cameras were placed at an angle of 25° to the normal direction of the surface of the sample being tested, as shown in the Fig. 2.9b. Schneider Unifoc-12 lenses (P/N 25-014780) were used in a forward configuration to achieve the required working distance (distance from the sample to the front face of the extension tube), as shown in Fig. 2.9b. An extension tube length of 35 mm was used with a working distance of 70 cm to achieve FOV of 45 x 30 mm. This setup was calibrated with a 30 x 24 mm GOM optical measuring calibration target. A high-intensity LED illuminator was used to illuminate the sample. As only black and white images are obtained when performing the DIC technique, red filters were used to enhance the image. Red filters can

lighten the difference between similar colors and improve the difference between opposite colors. Linear polarizers were used to eliminate unwanted reflected light and obtain a reflection-free image.

Strain computations were performed in Aramis 6.3.1. Facet size of 90 pixels and a step size of 40 pixels was used for all the strain computations to maintain consistency. Stereo digital image correlation could capture 3D deformation data and further data was processed in Aramis to obtain uniaxial strain.

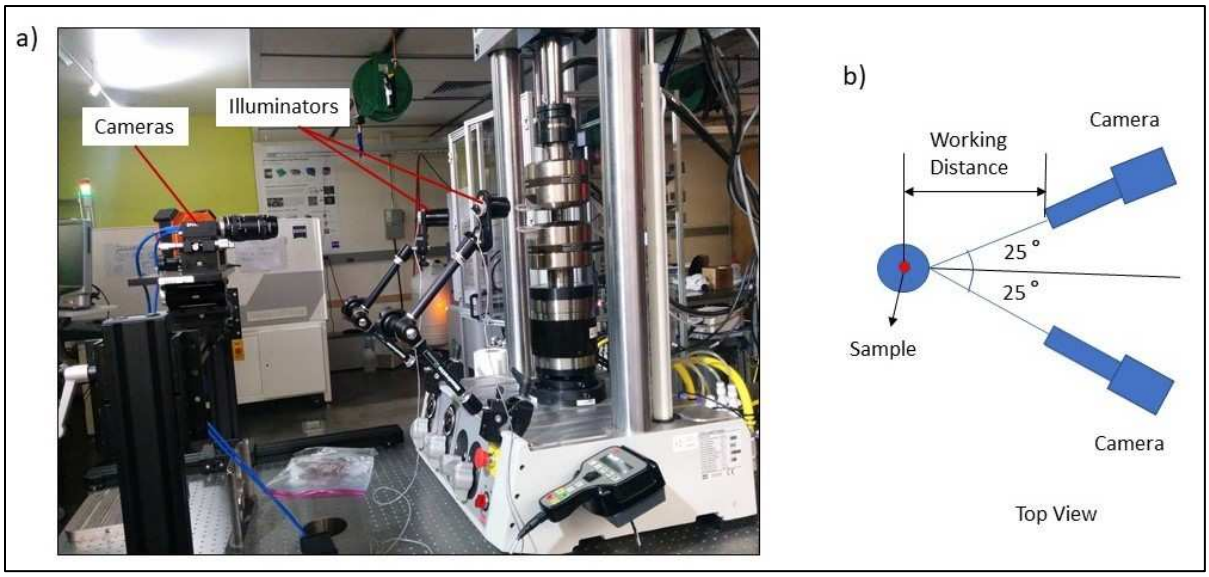

Fig. 2.9 a) DIC set up and b) camera angle and position for tensile testing

2.7. Hardness Testing

Some of the compression samples are utilized for hardness testing as well. Samples were mounted in epoxy resin. Struers LaboForce model 100 specimen mover was used to grind the samples using 500-, 1200-, and 2000-grit SiC paper and polished with successive diamond polishes down to 1 µm. Samples were ground half way through the thickness as shown in Fig 2.10. Polishing was completed with colloidal silica.

A Wilson Tukon Series 200 hardness tester was used to test the Vickers hardness (H_V) with a 500 lbf load and hold time of 10 s. All tests are conducted per ASTM E-384 [101]. Four measurements were made along the length of the sample and the average recorded as the hardness of the sample, as shown in the Fig 2.11.

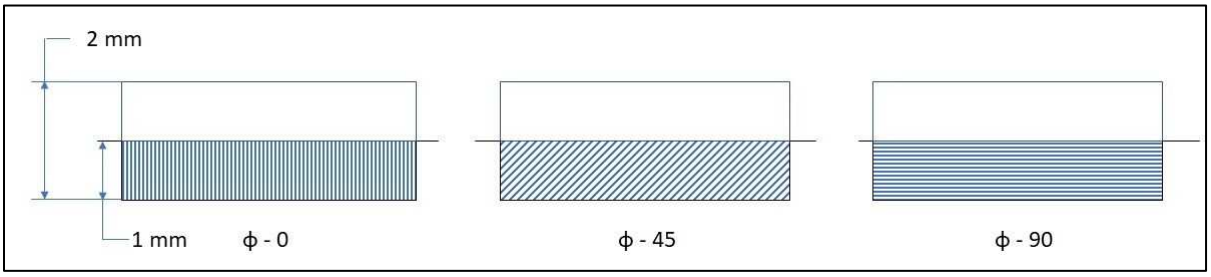

Fig. 2.10 Samples ground halfway through for hardness measurement

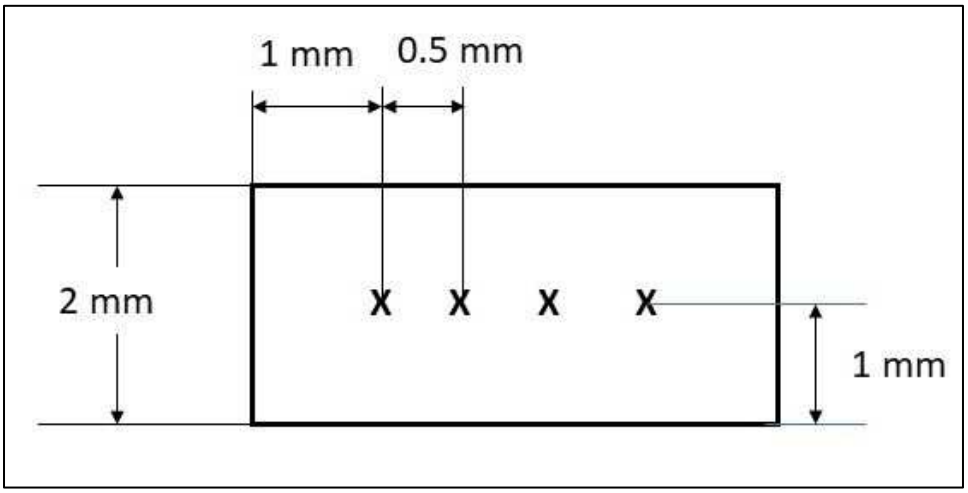

Fig. 2.11 Schematic showing hardness measurement location

2.8. Heat Treatment

In general, two different solid solution and precipitation hardening heat treatments are specified for Inconel 718. Plate 1 followed one such heat treatment: it was solution annealed at 980 °C, then water cooled. The plate was then precipitation hardened at 720 °C for 8 h and allowed to furnace cool over 2 h to 620 °C, where it was aged for an additional 8 h before being allowed to air cool to room temperature.

CHAPTER 3

CHARACTERIZATION OF MECHANICAL PROPERTIES IN AS-BUILT CONDITION

Often, characterization of mechanical properties of L-PBF printed parts is made after machining the parts smooth and to a uniform dimension. However, machining after printing the sample is not in line with the direct digital manufacturing principle of additive manufacturing and can obfuscate the impact of surface and near-surface defects that form in the as-printed part. And while simple geometric shapes like tensile and compressive samples can be machined after printing, it may not be possible to machine every surface of more intricate shapes. Hence, understanding the difference between properties in the as-built and machined conditions becomes important. In this chapter compressive and tensile properties of L-PBF printed samples in various orientations and locations on the build plate are studied in the as-built condition without any post-processing. Variation of properties with respect to the polar orientation and azimuthal orientation of the samples and their location on the build plate were characterized. Challenges in characterizing additively manufactured samples in the as-built condition and the methods used to overcome those challenges are discussed.

3.1 Challenges in characterizing compressive properties in as-built condition

Characterizing compressive properties of additive printed samples in the as-built condition is challenging. Factors such as non-parallel ends and non-uniform cross-section prevent standard testing protocols from achieving complete uniaxial compression. So, some metrics should be established to differentiate uniaxial and non-uniaxial compression. Indeed, even measuring the cross-sectional area of the sample is challenging because the shape of the compression sample when additively manufactured always deviates from the intended regular cylindrical shape or circular cross-section. Hence straight forward measurement of cross-section is not possible. Methods used to overcome these challenges are discussed in this section.

3.1.1. Differentiating uniaxial from non-uniaxial compression.

Although post-processing activities such as machining or electro-polishing are not carried out on compression samples, support structures are manually removed either by filing or cutting using a Dremel® tool. Despite efforts to make the compression sample ends parallel after removing the support structure, failure to achieve parallel ends, non-uniform cross-section or

eccentric loading frequently lead to shear or bending, as shown schematically in Fig 3.1. When the compression samples were tested in the as-built condition it was not possible to prevent shear or bending completely. It was possible, though, to identify whether or not uniaxial compression was achieved in a sample using some basic metrics.

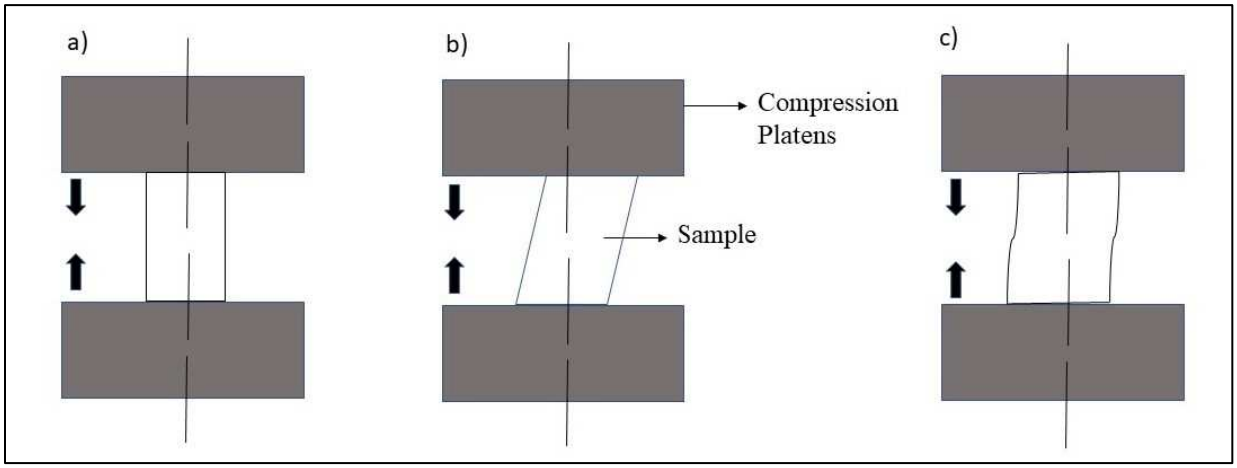

Fig. 3.1. Different modes of compression (a) uniaxial, (b) shear and (c) bending

Shear or bending may be induced before or after yield. If it is induced before yield the test is excluded from analysis. If, however, it is induced after yield, useful data can be extracted from the test. To identify whether shear or bending occurred before or after yield, both uniaxial and mises strain were computed from all compression tests conducted. Both uniaxial strain vs. uniaxial stress and mises strain vs. uniaxial stress plots were made, and 0.2% offset yield and Young's modulus computed from both plots. When Young's modulus measurements from both plots were within 10% variation, the test was considered to have achieved uniaxial compression and was retained for analysis. Typical stress-strain plots of both accepted and rejected tests are given in Fig. 3.2.

3.1.2 Area of cross-section of as-built samples

As mentioned earlier, the cross-section from samples in the as-built condition is not circular and not uniform throughout the length. Hence, the cross-sectional area of the compression samples cannot be determined by simply measuring the diameter with calipers. Therefore, an algorithm was developed to slice the three-dimensional tomography images of every non-machined compression sample into 1000 two-dimensional images. The number of pixels were counted in

each slice and multiplied by the area of one pixel to obtain the area of the cross-section of each slice. Then the minimum area was assigned as the cross-sectional area of that sample. A typical cross-section of samples of each orientation is shown in Fig 3.3.

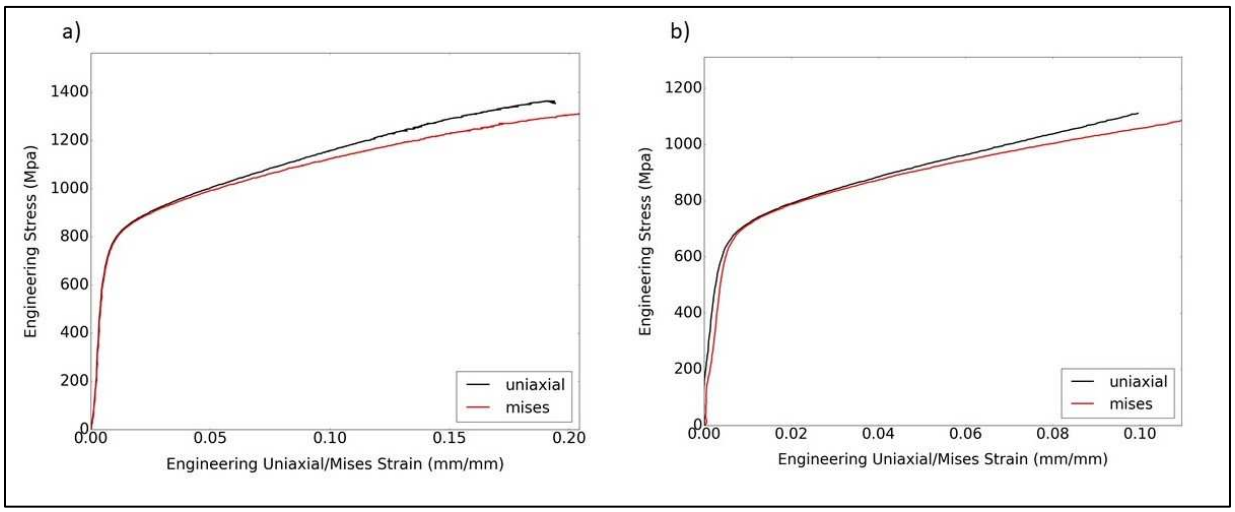

Fig. 3.2 (a) Accepted compression test and (b) rejected test, the latter being differentiable by the clear difference between the calculated uniaxial and mises stress-strain curves.

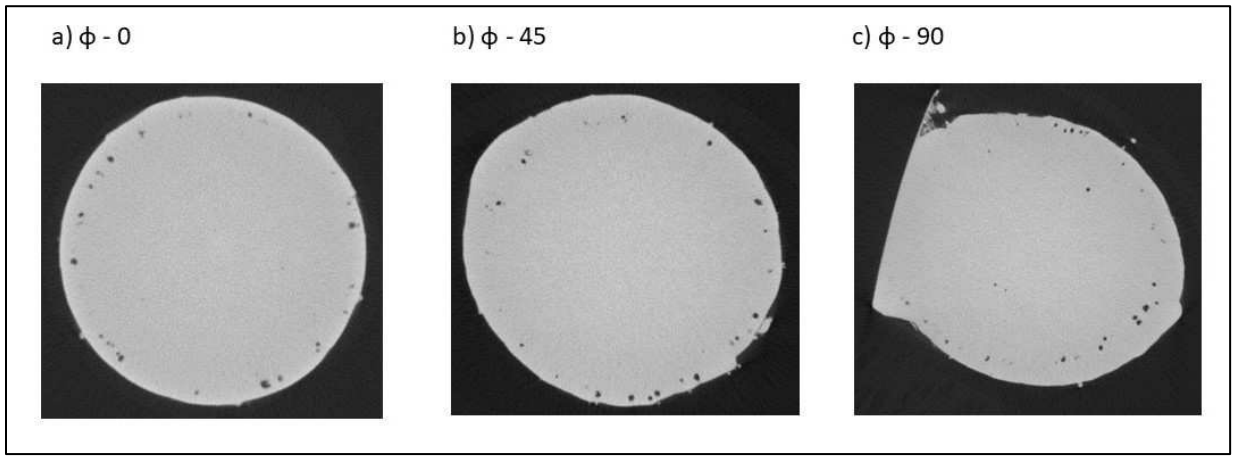

Fig. 3.3. Typical cross-section of compression samples built in various orientations

The target dimension of each sample is 2 mm x 4 mm with an ideal cross-section of 3.14 mm^2. It was observed that the actual cross-section varied from the ideal cross-section. Fig. 3.4 shows the distribution of actual cross-section of all compression samples tested in three different polar orientations. For studying mechanical properties in the machined condition, samples in the as-built condition were turned to a nominal diameter of 1.5 ± 0.2 mm. All machined

compression samples were tested per ASTM E9 [102]. Modulus measurements were performed per ASTM E111.

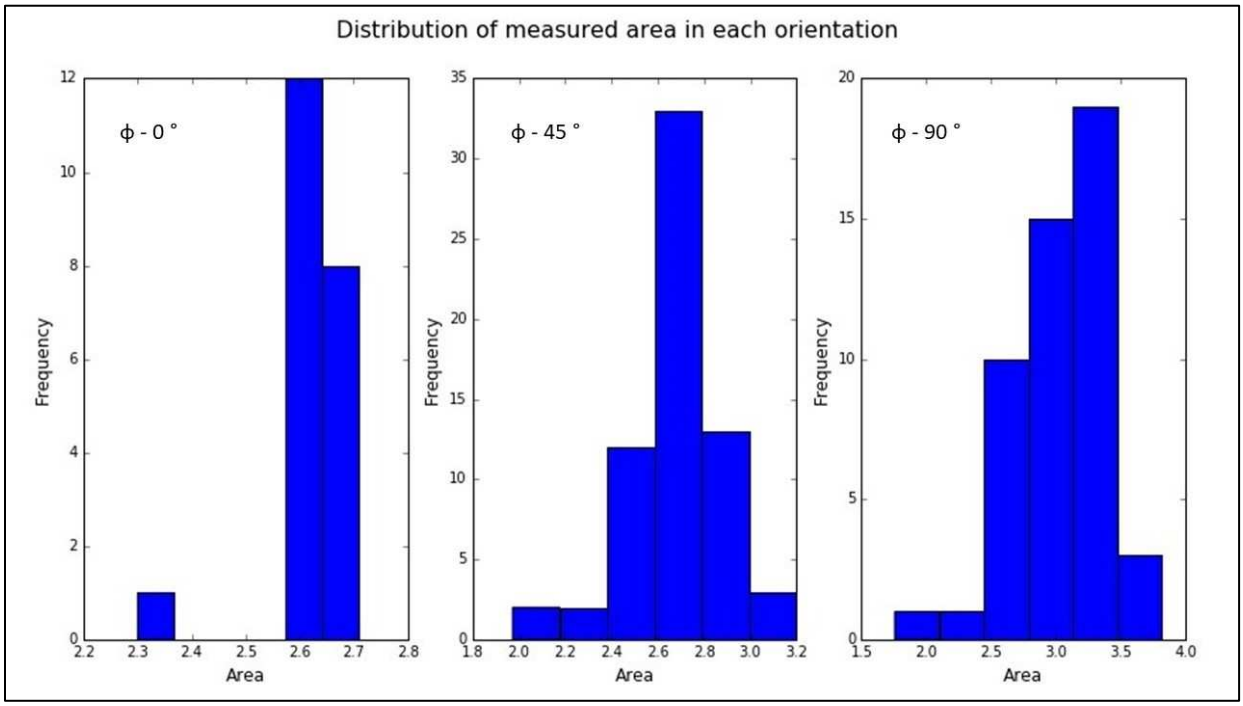

Fig. 3.4. Distribution of measured areas of compression samples of all polar orientations.

3.2. Effect of build orientation on compressive properties

In order to design a part for additive manufacturing, it is important to understand various factors that affect the properties of additively printed parts. Build orientation is an important factor to be considered. In this work, the impact of two different types of build orientations, such as polar build orientation ϕ and azimuthal build orientation θ as discussed in section 2.1.2, were studied. A schematic representation of all different types of orientations studied is shown in Fig. 2.3. Laser scanning path and the direction of heat transfer to the substrate are two heat flux directions involved in the L-PBF process. Grains grow in the direction of resultant heat flux direction. The direction of heat transfer to the substrate changes with polar orientation, and laser scanning path changes with azimuthal orientation; therefore, it is expected that texture and mechanical properties change with polar orientation ϕ and azimuthal orientation θ.

3.2.1. Effect of polar build orientation -ϕ on compressive properties

The influence of polar build orientation on compressive properties is shown in Fig 3.5. Both yield strength and elastic modulus of compression samples show properties in the trend of $\phi = 45° > \phi = 90° > \phi = 0°$. This trend agrees with earlier works reported on tensile properties [16], [58]. Several reasons have been reported in the literature for this anisotropy in mechanical properties with respect to build orientation. One ascribes this anisotropy to the columnar grain growth in the direction of heat flux. As the heat flux direction varies with respect to the laser scanning path and build orientation, so do the microstructures and mechanical properties [16]. Also γ" precipitates with strong [2 0 0] texture have been reported as a reason for anisotropy in the mechanical properties [56].

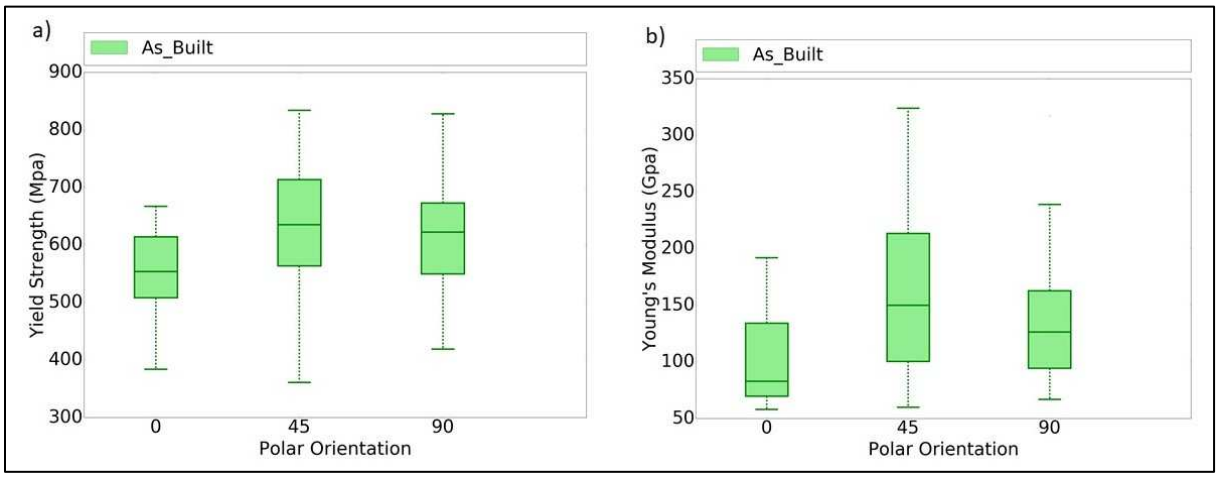

Fig. 3.5 Influence of polar orientation ϕ on compression properties a) yield strength and b) Young's modulus

3.2.2. Effect of azimuthal build orientation - θ on compressive properties

The influence of azimuthal orientation on the compressive properties of $\phi = 45°$ and $\phi = 90°$ samples are shown in Figs. 3.6 and 3.7, respectively. Strong trends were not observed with respect to variation in the azimuthal orientation θ. This may be because compression samples have only a very small cross-sectional area perpendicular to the build direction. The largest cross-sectional area perpendicular to the build direction of compressive samples is in $\phi = 90°$ samples and it is less than 8 mm^2, as shown in Fig 3.8. So, the effect of variation in laser scanning path with respect to azimuthal orientation has less effect on compressive properties.

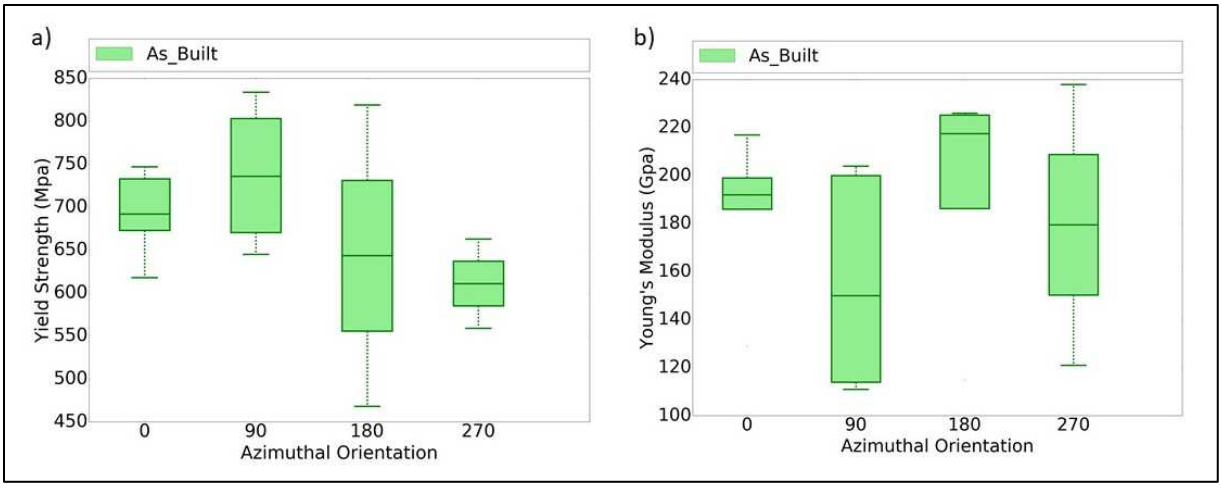

Fig. 3.6. Variation of compressive properties of ϕ = 45° build orientation samples with respect to azimuthal orientation, θ: (a) yield strength and (b) Young's modulus.

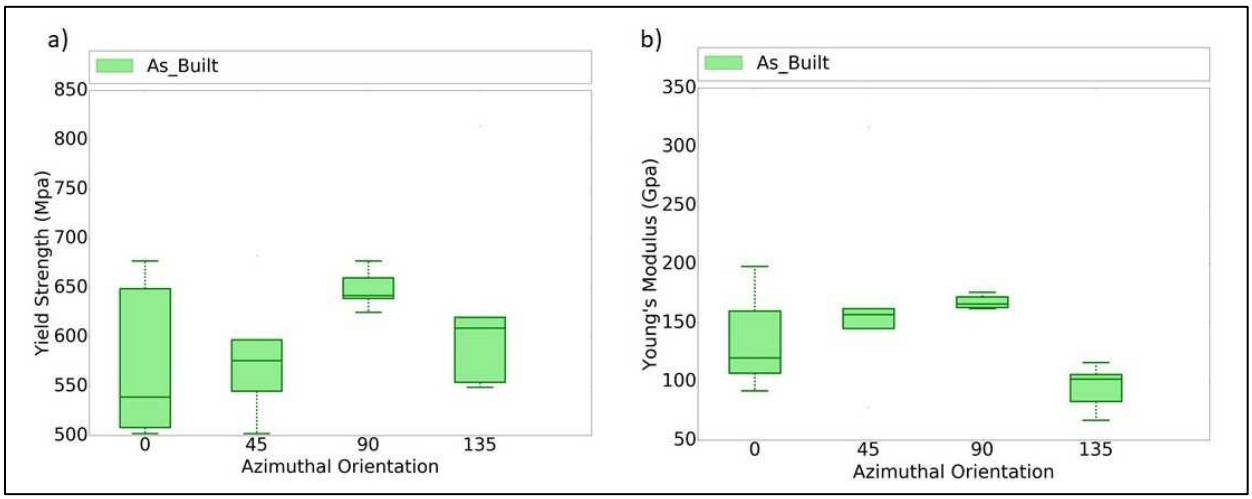

Fig. 3.7. Variation of compressive properties of ϕ = 90° build orientation samples with respect to azimuthal orientation, θ: (a) yield strength and (b) Young's modulus.

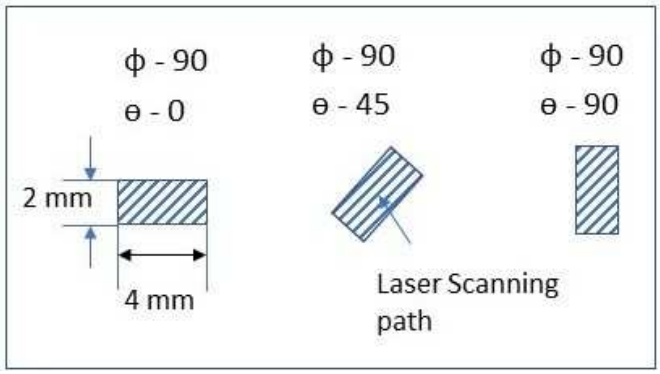

Fig. 3.8 Variation in the laser scanning path with respect to azimuthal orientation, θ.

3.3. Effect of build orientation on tensile properties

Different polar orientations (ϕ) and azimuthal orientations (θ) of tensile samples discussed in this work are schematically illustrated in Fig 3.9. Heat transfer into the substrate and along the receding build path are two examples of heat flux involved in the L-PBF processes. Heat flux impacts mechanical properties by affecting microstructure, and it has been shown that grain growth occurs in the direction of resultant heat flux direction [16]. The direction of heat transfer to the substrate changes with polar orientation and build path changes with azimuthal orientation. So, it is expected that texture and mechanical properties change with polar orientation (ϕ) and azimuthal orientation (θ). Tensile samples were tested in the as-built condition only. The conditions that adversely affect the testing of compression samples in the as-built condition are not present in tensile testing because, unlike compression testing, the loading direction is perpendicular to the sample-load frame contact surfaces. In the absence of these testing artifacts, it is expected that trends in tensile properties with respect to polar and azimuthal orientation will more accurately reflect the true properties of the materials.

3.3.1. Effect of polar build orientation - ϕ on tensile properties

Despite a huge spread in properties, from Fig. 3.11 in page 44 we can observe a clear trend in all tensile properties. Yield strength, Young's modulus, and ultimate strength show a clear trend with respect to polar orientation such that $\phi = 90° > \phi = 45° > \phi = 0°$. This trend does not agree with either literature or the compression properties discussed earlier.

Yield strength, Young's modulus, and ultimate strength of $\phi = 45°$ are larger than those measurements for $\phi = 90°$, i.e., the tensile properties at $\phi = 45°$ are greater than the tensile properties at $\phi = 90°$, according to E. Chlebus et al. [16]. This disparity may be because samples tested and reported in literature were cylindrical samples with gage diameters not less than 4 mm, whereas in this work, flat specimens with rectangular cross-sections and gage thicknesses of 2 mm were used. In flat samples, the ratio of the area scanned with contour and skin laser settings is significantly different than that for the $\phi = 90°$ sample, as illustrated schematically in Fig. 3.10. Compared to the machined samples of thicker circular cross-section tested in literature [16], flat tensile specimens built at $\phi = 0°$ and $\phi = 45°$ orientations exhibited a lower Young's modulus while $\phi = 90°$ samples showed a comparable Young's modulus. This suggests that the significant area

fraction built with the *contour laser setting* impacts the final mechanical properties of samples built at any angle to the build surface.

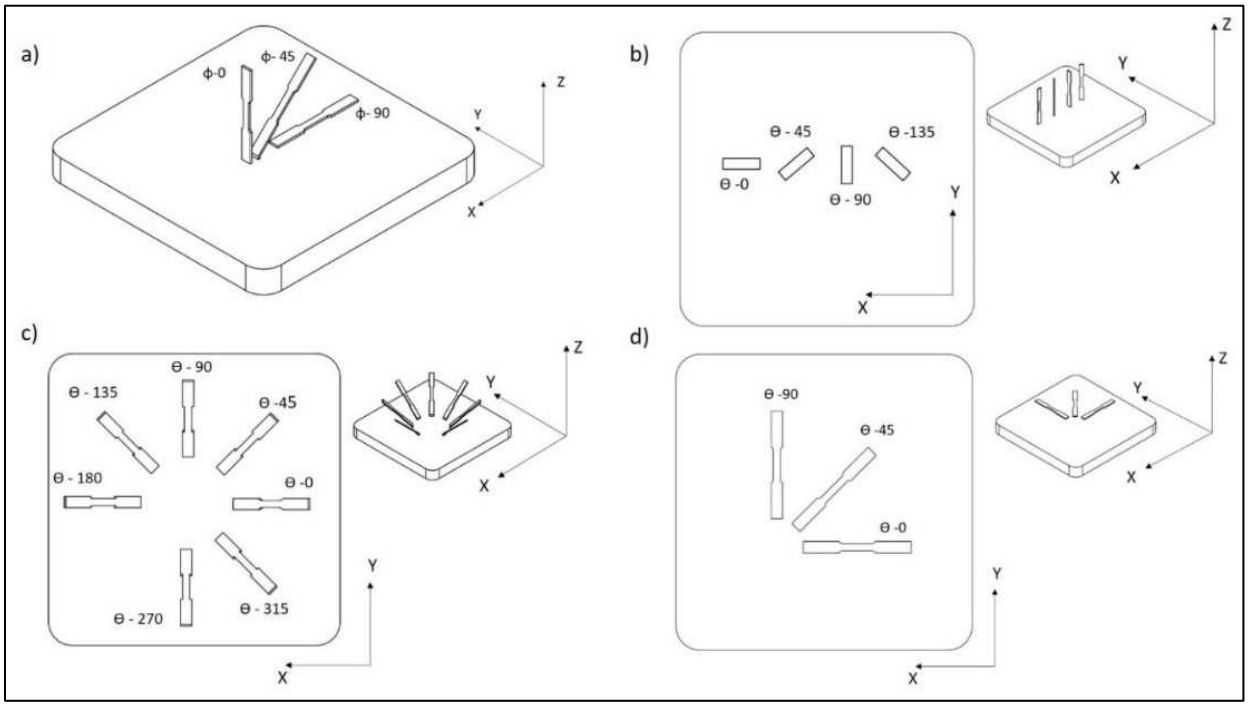

Fig. 3.9 Schematic representation of a) polar build orientation (ϕ) and azimuthal build orientations for b) ϕ = 0° samples, c) ϕ = 45° samples and d) ϕ = 90° samples

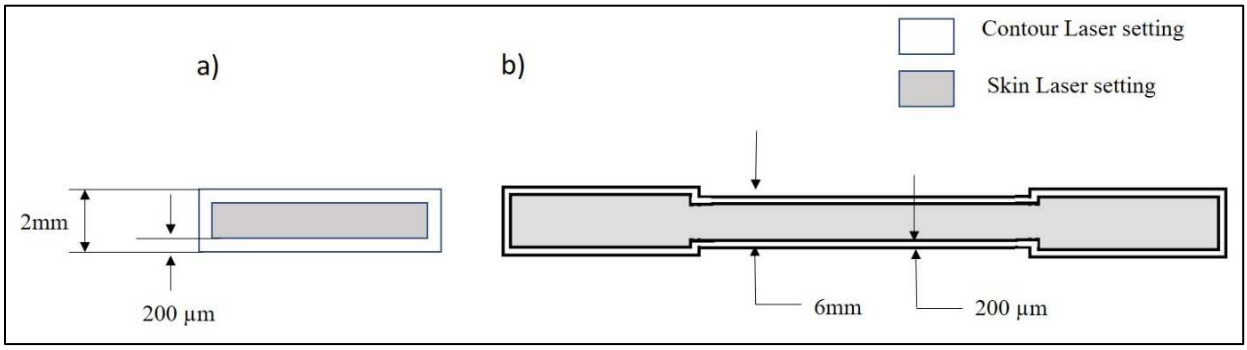

Fig. 3.10 When built at ϕ = 0° each layer in the build is a cross section as shown in panel (a), as compared to the cross section of parts built (b) at ϕ = 90°. A larger fraction of the part is built with the contour laser setting in (a) than in (b).

3.3.2. Effect of azimuthal build orientation - θ on tensile properties

It is clear from Figs. 3.12 in page 45, 3.14 in page 46, and 3.15 in page 47 that azimuthal orientation has very low effect on ϕ = 0° and ϕ = 45° samples, but has considerable impact on ϕ = 90° samples. It could be observed that the effect of θ orientation on mechanical properties gets

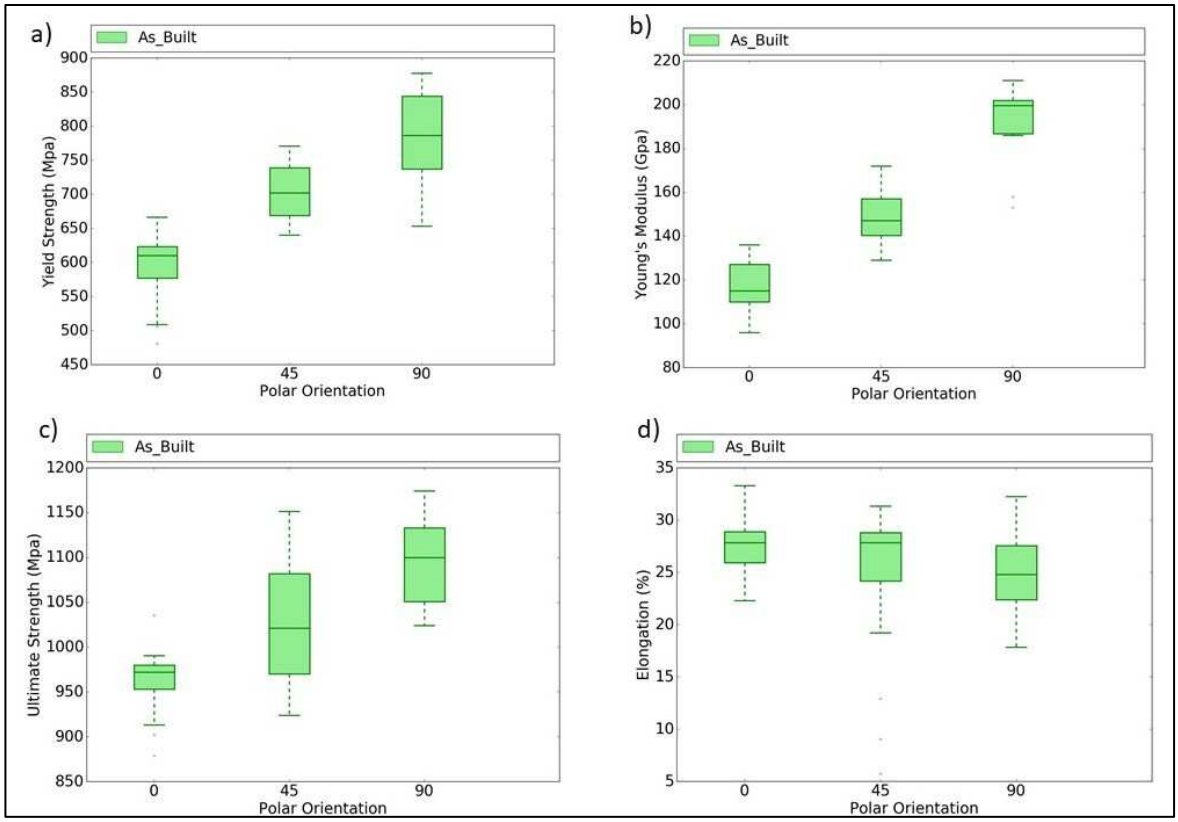

Fig. 3.11 Variation of tensile properties (a) yield strength, (b) Young's modulus, (c) ultimate strength, and (d) ductility with respect to polar orientation.

more obvious and clear in $\phi = 90°$ build samples. The laser scanning pattern at every point in the build is set by the distance to the surface nearest to that point. Points within 200 µm of an outer surface are built with the contour laser scanning pattern. In a single build layer, the skin will be more than 200 µm from an edge. Points more than 200 µm from any surface are built with the skin laser scanning pattern. For $\phi = 0°$ and $\phi = 45°$ builds, area scanned with skin laser setting is very small. This laser scanning pattern traverses the layer cross-section at a constant angle.

For $\phi = 90°$ samples, area scanned with skin laser settings per layer is large compared to samples of other two orientations. Importantly, at $\phi = 90°$, the constant angle for the skin laser scanning pattern is collinear with the loading direction in the gage at $\theta = 45°$. This effect is shown in Fig. 3.13 in page 45. Also, $\phi = 90°$ samples were loaded perpendicular to build direction during testing, where variation of laser scanning path and its effect on mechanical properties becomes more important.

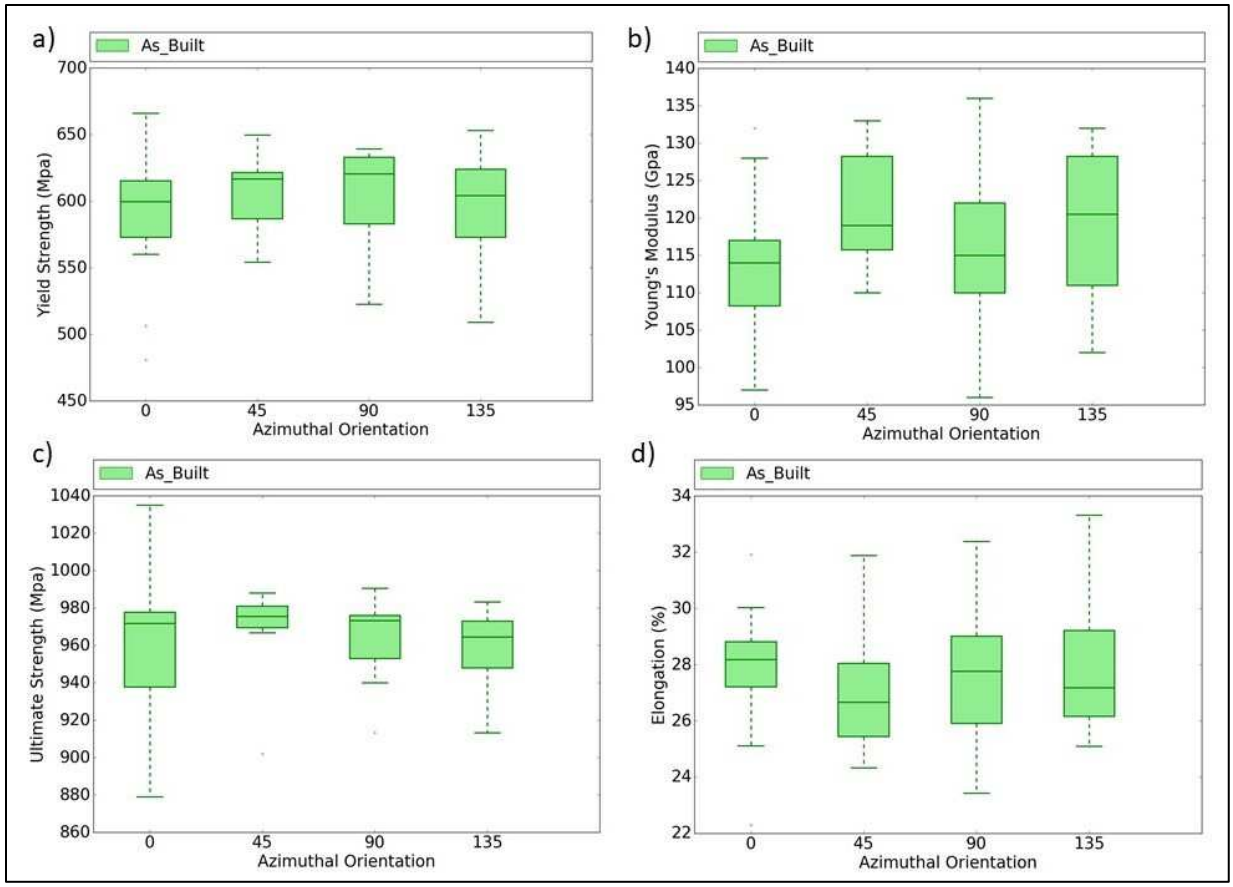

Fig. 3.12 Variation of tensile properties of $\phi = 0°$ build orientation samples with respect to azimuthal orientation, θ (a) yield strength, (b) modulus, (c) ultimate strength and (d) ductility.

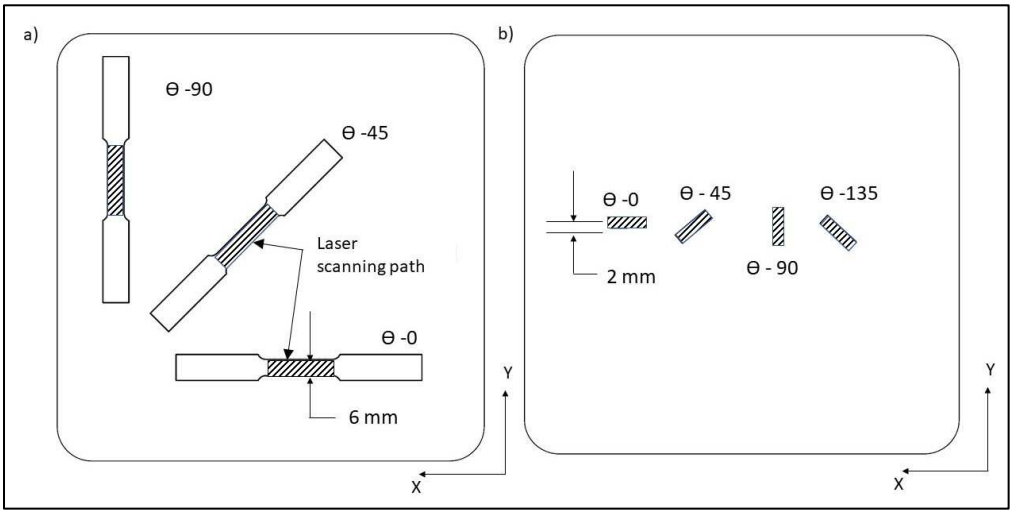

Fig. 3.13 Variation in the laser scanning path caused by azimuthal build orientation a) $\phi = 90°$ samples b) $\phi = 0$ samples

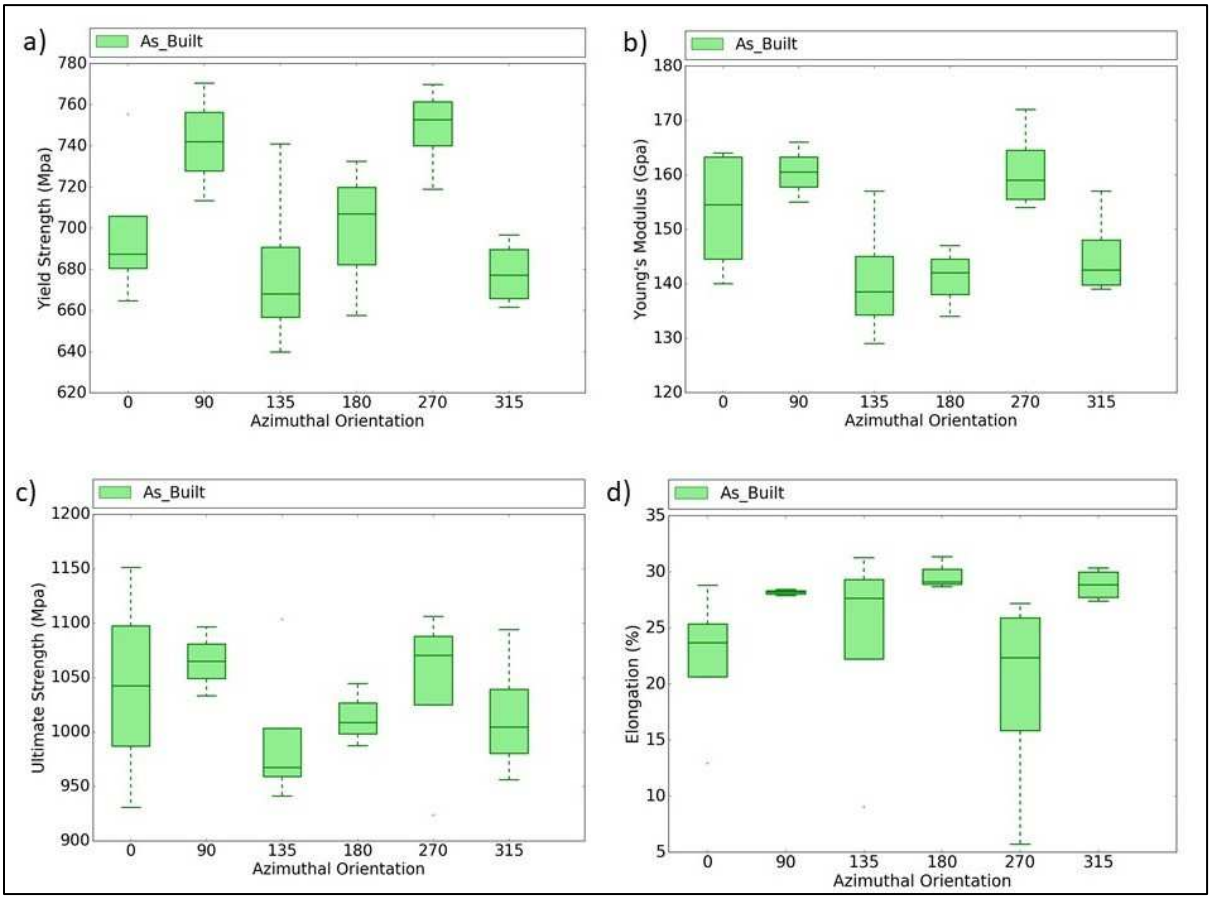

Fig. 3.14 Variation of tensile properties of $\phi = 45°$ build orientation samples a) yield strength b) Young's modulus c) ultimate strength and d) ductility with respect to azimuthal orientation θ

3.3.3 Effect of printing location on tensile properties

Because the laser source is fixed and not moving, the intensity distribution and shape of the laser spot may vary between a position straight below the source and a position at an angle to the source on the build plate. This effect was studied in additive manufacturing of polymers but not in metals. Studying and quantifying this effect would help us understand how far from a laser source we could build samples without a significant change in properties. This effect is one of the important factors to be considered to expand the build volume in the L-PBF process. To study this effect, $\phi = 0°$ build orientation samples were built at various locations on the build plate. $\phi = 0°$ samples were chosen to study this effect because $\phi = 0°$ builds are more constrained to a specific location and they are built with the least change in laser orientation throughout the build. The position of samples built to study this effect are given in Fig. 3.16 in page 48.

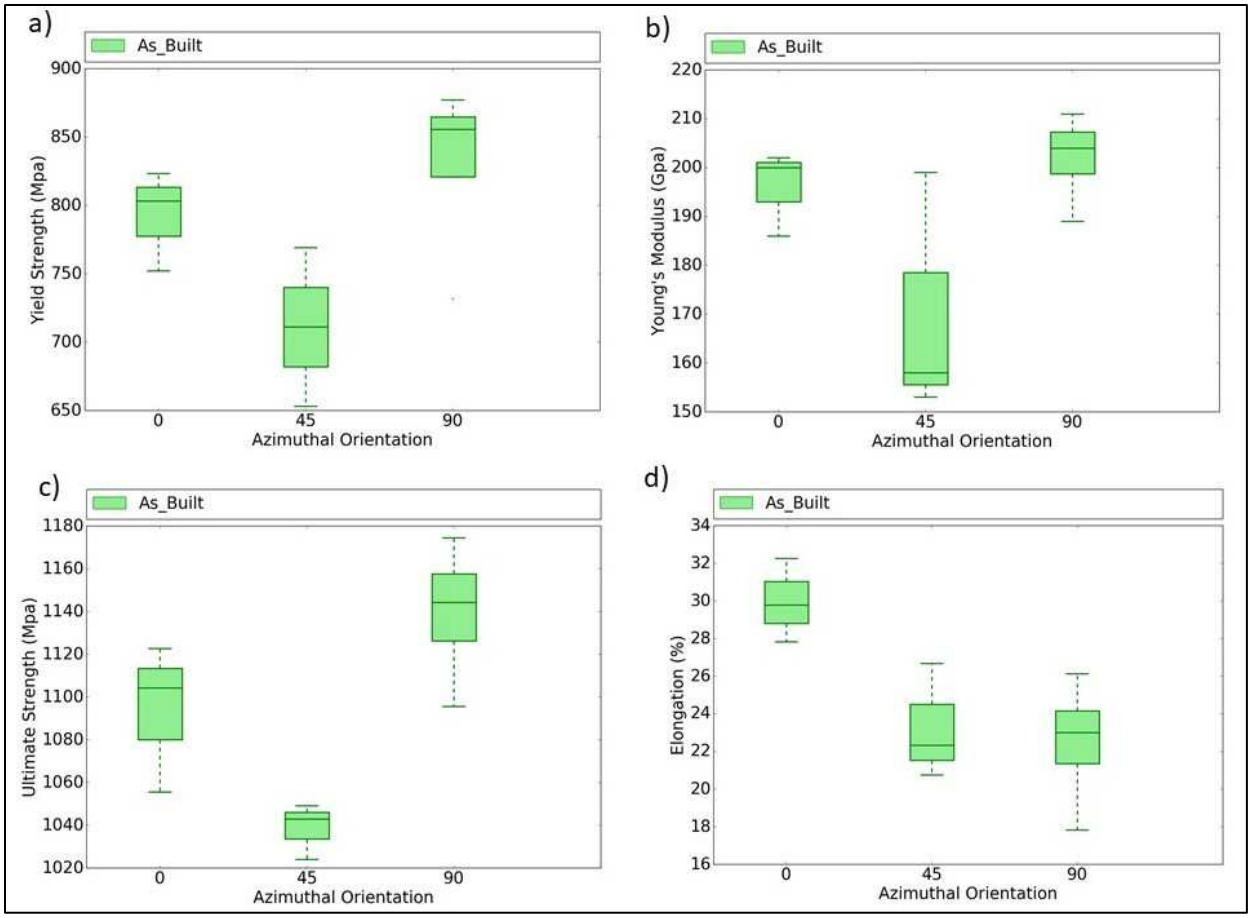

Fig. 3.15 Variation of tensile properties of $\phi = 90°$ build orientation samples a) yield strength b) Young's modulus c) Ultimate strength and d) Ductility with respect to azimuthal orientation θ

A comparison of Young's modulus of samples built by laser 1 and laser 2 in various locations of the build plate is shown in Fig. 3.17 in page 49. It could be observed that there is no strong trend in variation of modulus of samples as their distance from the laser source increases. This proves that variation of intensity distribution within the range of the build plate is minimal, and effect of this variation on tensile properties is not strong.

3.4. Hardness

Hardness properties are shown in Fig. 3.18 in page 49. Unlike other properties discussed previously, hardness properties do not show a strong trend with respect to build orientation. These results are generated by testing nine samples in each orientation. From Figs. 3.5 in page 40, 3.11 in page 44, and 3.18 in page 49, it can be observed that the trends in compressive strength and tensile strength with respect to polar orientation do not match the trend in hardness. So, it can be

understood that hardness values of additively printed parts are not representative of the parts' tensile and compressive strengths like conventionally manufactured parts. This may be because additive printing is a layer-based process and hence different layers may undergo different thermal histories, unlike conventional processes.

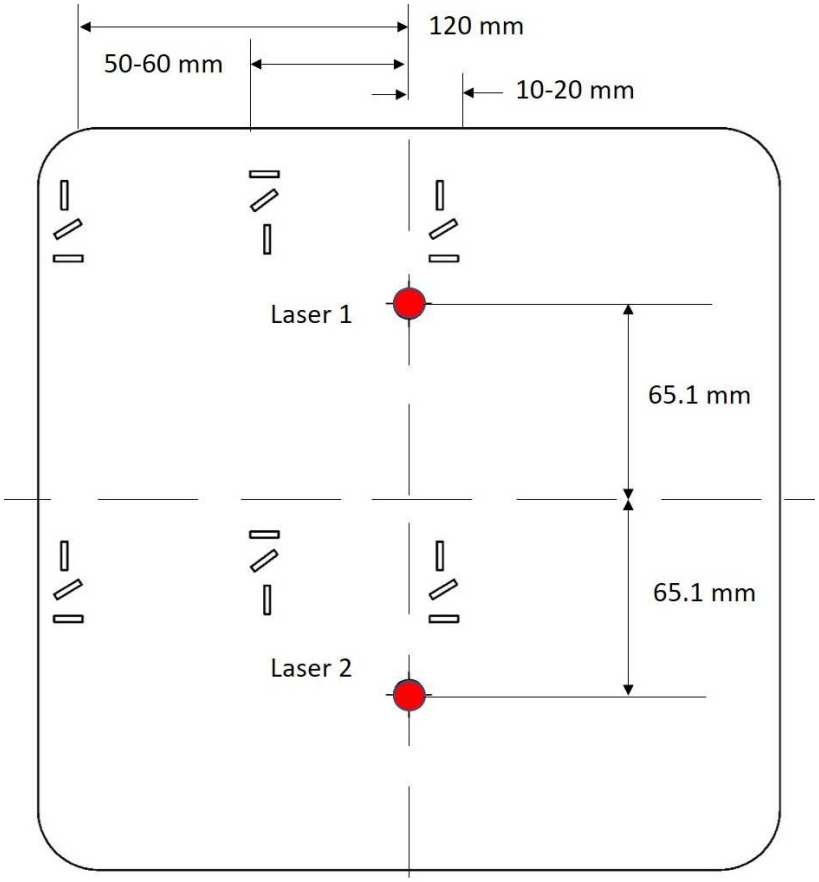

Fig. 3.16 $\phi = 0°$ samples printed in various location on the plate to assess the effect of their position with respect to laser source

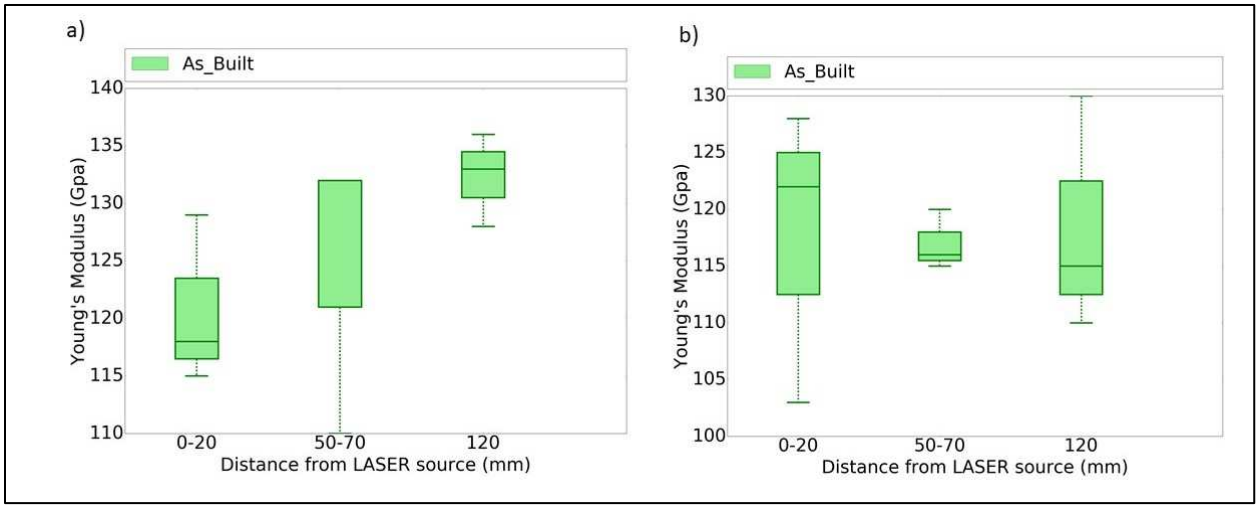

Fig 3.17 Variation of Young's modulus with respect to sample's position on build plate a) laser 1 and b) laser2

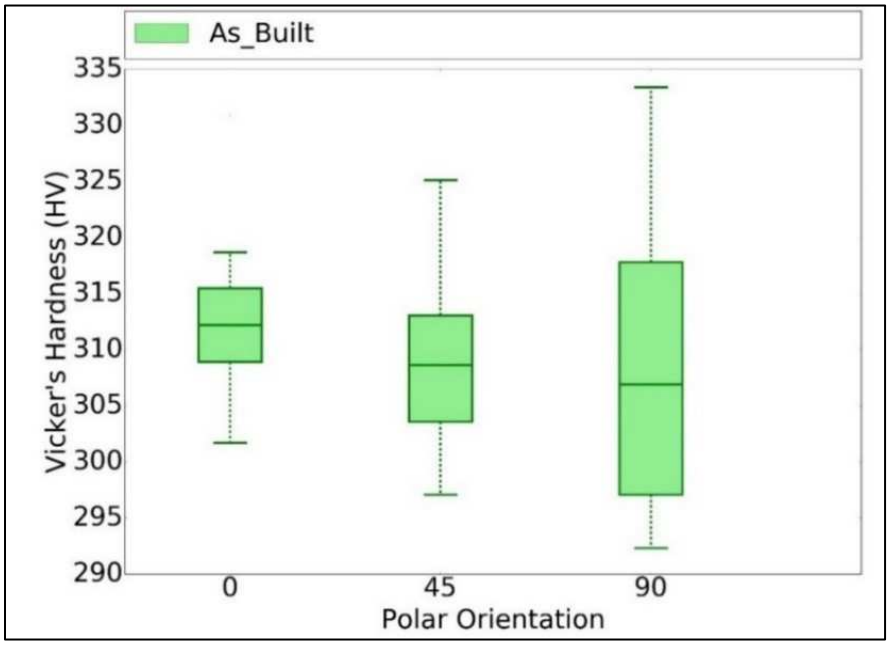

Fig 3.18 Variation of Vicker's hardness with respect to polar orientation.

CHAPTER 4

INFLUENCE OF POST PROCESSING ACTIVITIES AND POROSITY ON MECHANICAL PROPERTIES

All samples were printed to their specified dimension and geometry and were expected to achieve their desired properties. In reality, they deviated from their specified geometry, shape, and expected mechanical properties for several reasons, such as unmolten powder, overbuild, porosity, and support structures. Machining makes the shape of the compression samples uniform, removes all unmolten powder on their surface, and removes most of the porosity concentrated around their outer periphery. Also, it was discussed earlier in section 3.3 that some part of the sample was manufactured with contour laser setting and some part was manufactured with skin laser setting. Machining removes the part of the sample manufactured with contour laser setting; hence, variations in properties after machining need to be understood.

Heat treatment changes the microstructure. Because Inconel 718 is a precipitation hardened alloy, new phases precipitate out in the matrix and strengthen the alloy. For this reason, it is important to understand how heat treatment influences the properties in general and whether it changes the anisotropy developed in the as-built condition because of build orientation. To understand the impact of machining, some samples from each polar orientation in the as-built condition were machined from 2 mm diameter down to 1.5 mm nominal diameter. At the same time, samples from heat-treated plates of compression and tensile samples of all polar orientations were tested and their properties were comparatively analyzed with corresponding properties in the as-built condition, as discussed in this chapter.

4.1 Effect of post processing activities on compressive properties

Machining and heat treatment are two common post-processing activities used to improve mechanical properties. Machining is performed to remove all unmolten powder and porosity and to make the surface of the part smooth. Currently, standard solid solution strengthening and precipitation hardening heat treatments are also frequently performed to improve mechanical properties. In this section, the impact of both these post-processing activities on compression properties are analyzed by comparing them to the samples in corresponding orientations in the as-built condition.

4.1.1. Effect of machining on compressive properties

Figure 4.1 reveals that the trend in variation of properties with respect to polar orientation remained the same in both the as-built and machined conditions, but that the latter showed improved modulus and yield strength. This change can be rationalized by the fact that the area produced by the contour laser setting is completely removed and that the ends are flat and parallel, which, unlike coupon ends in the as-built condition, creates the conditions required for uniaxial compression. Moreover, after machining, 50% of the porosity was removed. Also, the cross-sectional area of the samples became uniform after machining. A nonuniform cross-section leads to an axial misalignment in the application of load that further complicates strain measurements. All these factors contribute to improvement of properties after machining. While the yield strength became more consistent, the distribution of modulus measured remained wide even after machining, which is consistent with the insensitivity of the static Young's modulus to sub-1% porosity.

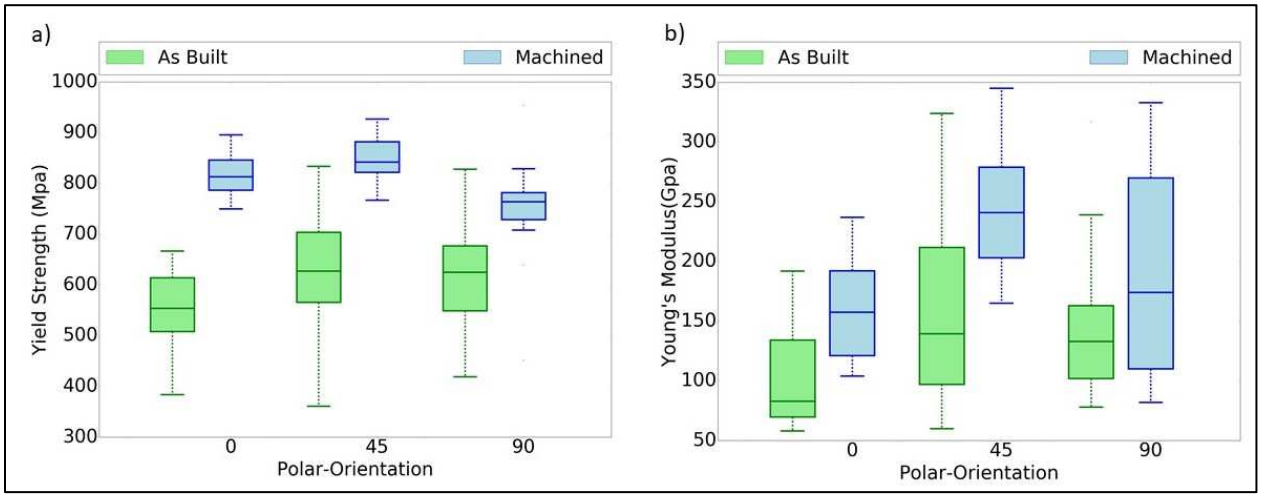

Fig. 4.1 Comparison of properties in as built and machined condition a) yield strength and b) Young's modulus

4.1.2. Effect of heat treatment on compressive properties

After solution annealing and ageing, all heat-treated samples, regardless of orientation, show improved yield strength. This is expected because after heat treatment the phase fraction of γ' (Ni_3Al) increases, which increases the yield strength [92]. Although the mean Young's modulus of all build orientation shows a positive shift, the distribution stays within the range measured in the as-built condition. It can be observed from Fig 4.2 that the anisotropy in mechanical properties

developed in the as-built condition ($\phi = 45° > \phi = 90° > \phi = 0°$) is still preserved even after heat treatment. This indicates that the anisotropy with respect to build orientation that developed in the as-built condition is not modified by annealing, which is in agreement with literature [16].

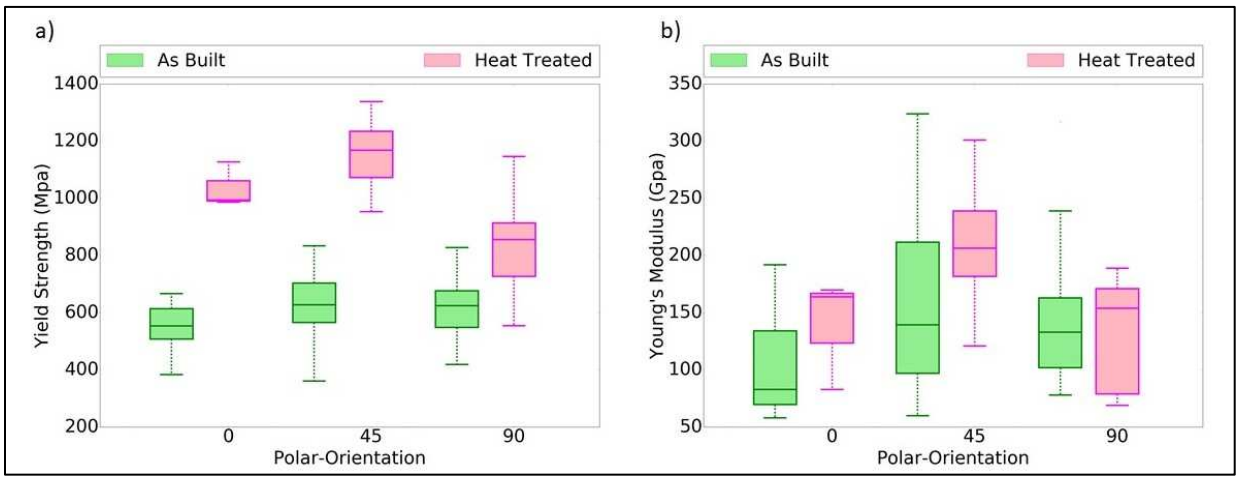

Fig. 4.2. Comparison of compressive (a) yield strength and (b) Young's modulus in the as-built and heat-treated conditions.

4.2. Effect of heat treatment on tensile properties

In general, after heat treatment, tensile samples showed improved yield, Young's modulus, and ultimate strength, but reduced ductility. As shown in Fig. 4.3, irrespective of polar build orientation, yield strength became uniform after heat treatment. Young's modulus retained the anisotropy ($\phi = 90° > \phi = 45° > \phi = 0°$) developed in the as-built condition, even after heat treatment. Tensile strength and ductility became uniform for $\phi = 0°$ and $\phi = 45°$ samples, and $\phi = 90°$ samples showed improved tensile strength and ductility when compared with samples from the other two orientations. $\phi = 0°$ and $\phi = 45°$ samples showed 45% and 36.3% improvement in yield, and $\phi = 90°$ samples showed only 31% improvement in yield after heat treatment. This could be understood by the effect discussed in section 4.3.1. The ratio of area scanned by contour laser setting is higher in $\phi = 0°$ and $\phi = 45°$ samples than in $\phi = 90°$ samples in the as-built condition. Additionally, the mechanical properties of the portion scanned by contour laser settings change in a way to make $\phi = 45°$ and $\phi = 0°$ samples lower in yield and Young's modulus.

From Fig. 4.4, it can be observed that anisotropy in properties developed in $\phi = 90°$ samples was also retained after heat treatment because of variation in the scanning path with respect to azimuthal orientation θ. $\theta = 45°$ samples show low modulus compared to that of the other two

orientations after heat treatment. This proves that anisotropy developed in the as-built condition is not modified after heat treatment. Hence, it is important to understand and control anisotropy in the as-built condition to achieve consistency in properties.

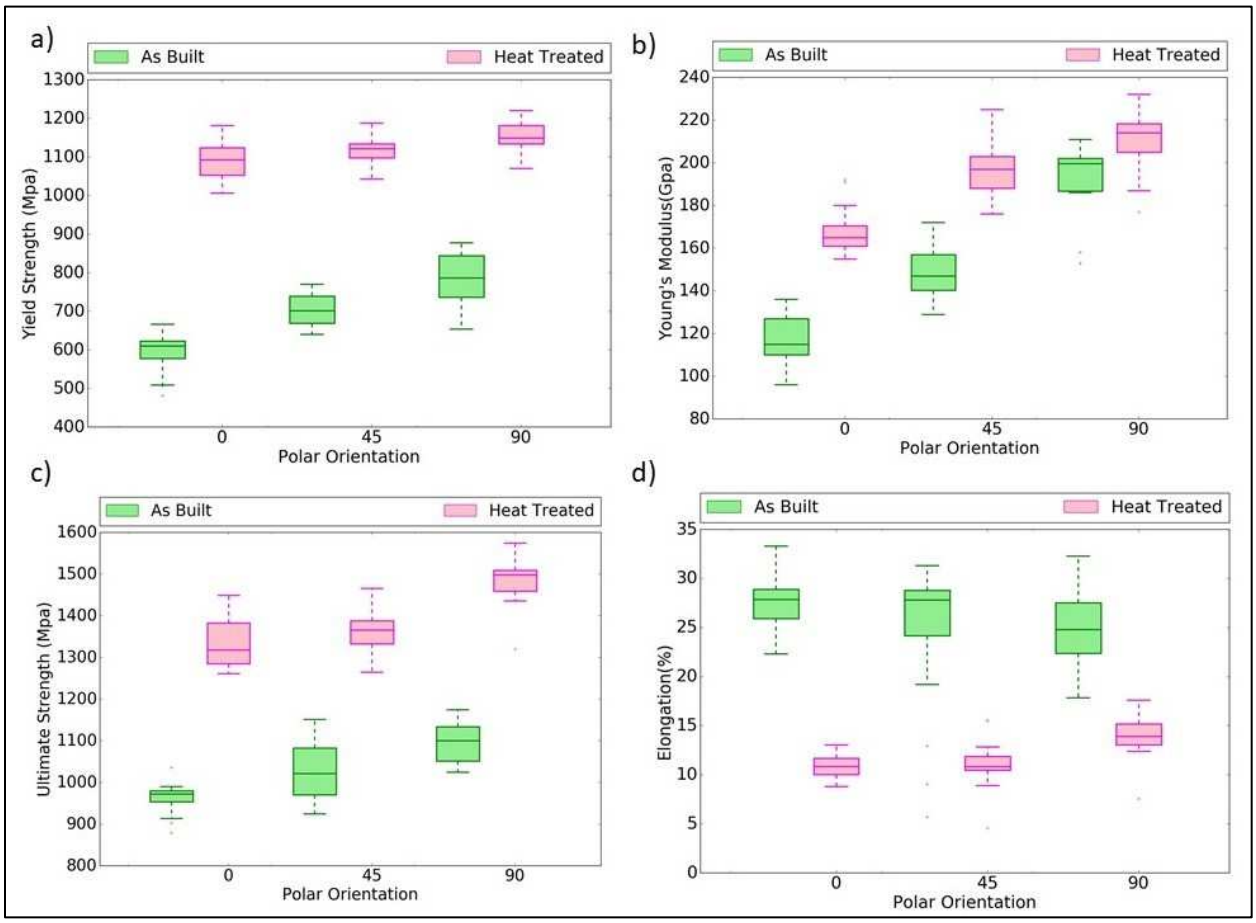

Fig 4.3. Comparison of (a) yield strength, (b) Young's modulus, (c) ultimate strength and (d) ductility (%) in the as-built and heat-treated conditions.

4.3 Influence of heat treatment on hardness

The hardness of the L-PBF printed samples improved from 312 ± 20 H_V in the as-built condition to 493 ± 32 H_V after heat treatment, an approximately 58% increase. As in the as-built compressive and tensile properties, no trends were observed with respect to polar orientation. Comparisons of hardness in the as-built and heat-treated conditions with respect to orientation are shown in Fig. 4.5.

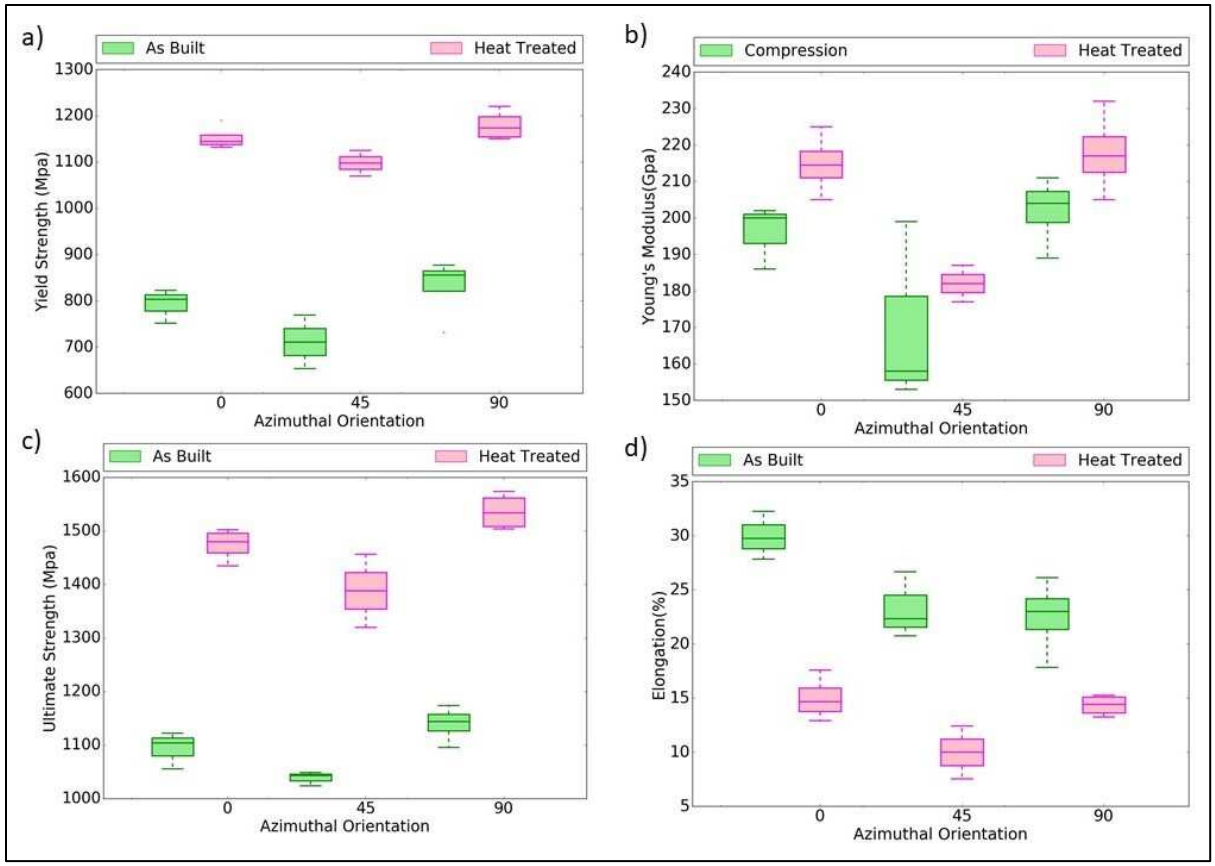

Fig 4.4. Comparison of (a) yield strength, (b) Young's modulus, (c) ultimate strength, (d) ductility (%) for $\phi = 90°$ samples in as-built and heat-treated conditions.

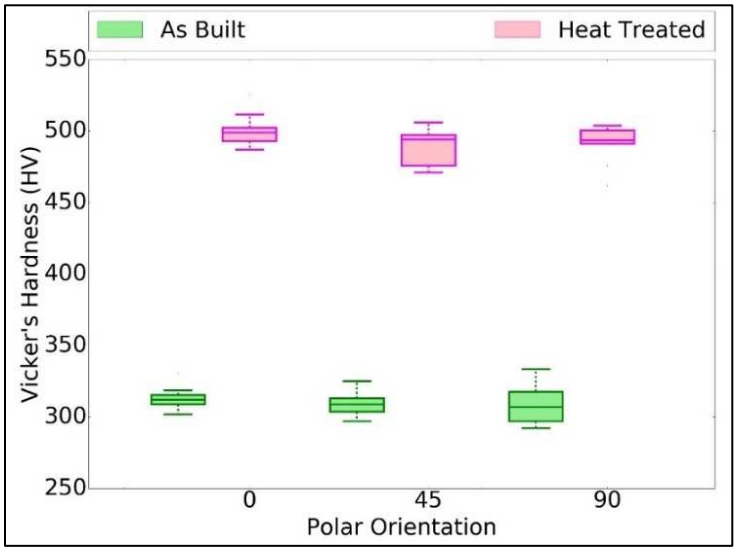

Fig 4.5. Comparison of Vicker's hardness in as-built and heat-treated conditions.

4.4 Comparison of compressive and tensile properties

Fig 4.6 and Fig 4.7 compare the tensile and compressive properties in the as-built and heat-treated conditions. It is clear from Fig. 4.6 that the tensile yield strength and Young's modulus are greater than the compression yield strength and Young's modulus in the as-built condition, irrespective of build orientation ϕ. In the heat-treated condition, samples with build orientations of $\phi = 0°$ and $\phi = 45°$ show similar properties in both compression and tension. For the same reasons discussed in section 3.3.2, the properties of $\phi = 90°$ samples look better in tension in both the as-built and heat-treated conditions. Fig 4.8 shows the typical stress-strain responses of as-built and heat-treated samples in both compression and tension. The strain hardening seen in this figure demonstrates that plastic deformation occurs through crystallographic slip. Overall, compression properties show a large distribution compared to tensile properties in both the as-built and heat-treated conditions.

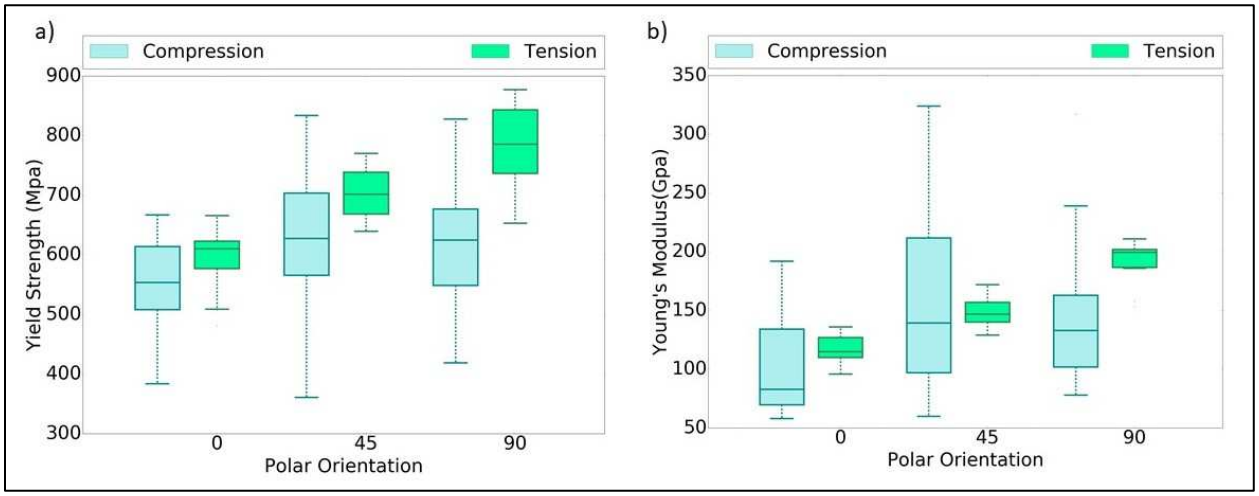

Fig 4.6 Comparison of compressive and tensile properties in as built condition a) yield strength b) Young's modulus

4.5 Porosity and its influence on mechanical properties

Figure 4.9 in page 57 shows the distribution of porosity volume fraction in the as-built and machined conditions. Although the sampling size in the two conditions is not equal, most as-built samples have a porosity volume fraction in the range of 0.1–0.2%, and most machined samples have a volume fraction below 0.1%. A reduction in the volume fraction porosity in excess of 50% is achieved after machining. Also, Figs. 4.9 in page 57 and 4.10 in page 58 show some samples with relatively high values of volume fraction and pore diameter.

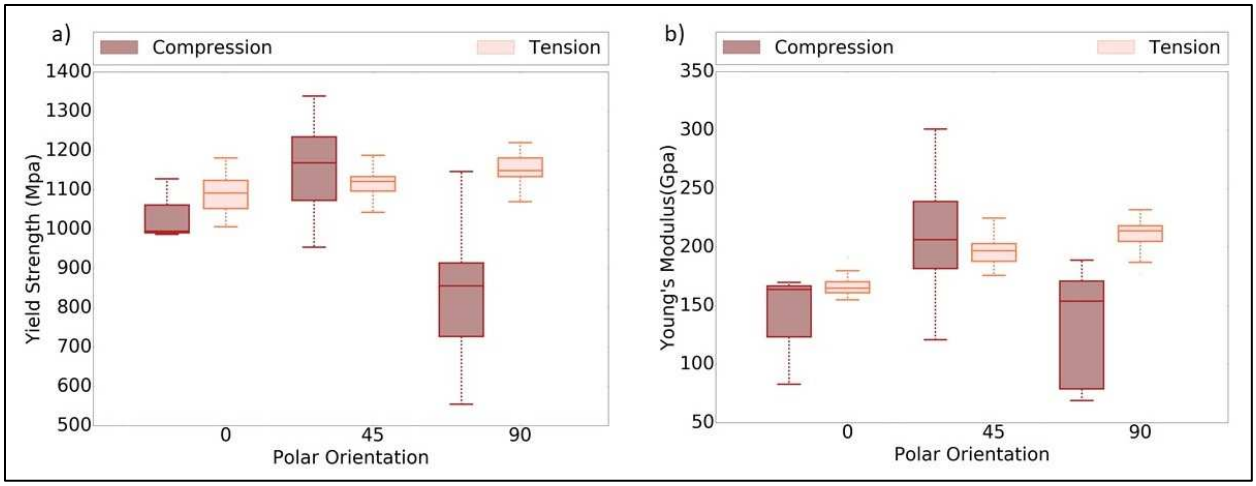

Fig 4.7 Comparison of compressive and tensile (a) yield strength and (b) Young's modulus in the heat-treated condition.

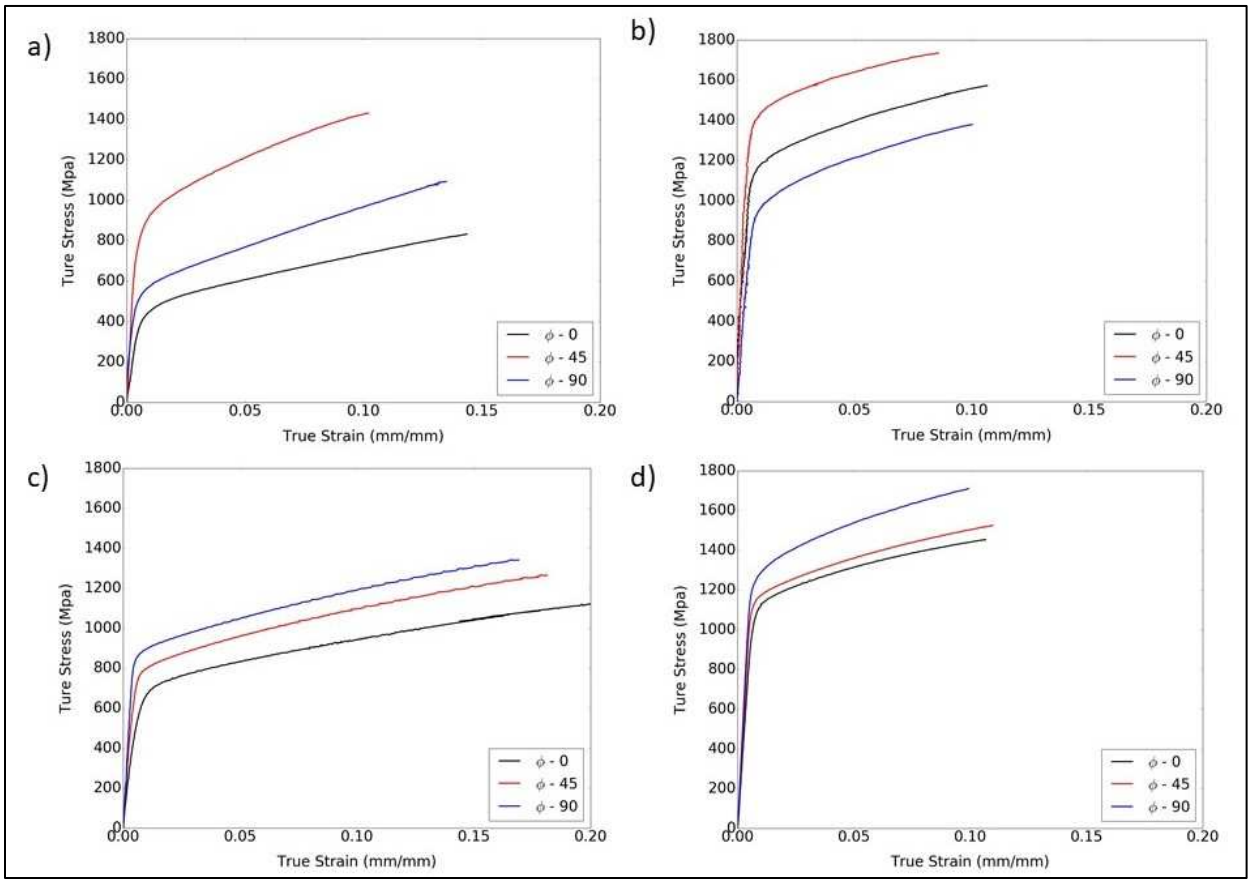

Fig 4.8 True stress-strain responses for (a) as-built samples under compression, (b) heat-treated samples under compression, (c) as-build samples under tension and (d) heat-treated samples under tension.

To understand these outliers, the distribution of porosity volume fraction and maximum pore diameter with respect to orientation was studied. Figure 4.11 shows the distribution of volume fraction of porosity and maximum pore diameters with respect to orientation. It is clear from Fig. 4.11 that most of the outliers with very high porosity volume and pore diameter were built at $\phi = 45°$, particularly those samples at $\theta = 0°$ located near the supply side of the build plate, as shown in the schematic in Fig. 4.12 in page 59. Further investigation into the tomography of those samples confirmed that the lack of fusion defect followed distortion of the sample build. A typical distorted sample with lack of fusion porosity is shown in Fig. 4.13 in page 59.

The mechanism for forming lack of fusion defects can be understood in the light of build mechanics. A "bow wave" is formed in the melt pool ahead of the laser along the laser path, as seen in Fig. 4.14 in page 60, which leads to the formation of overbuild. Once the overbuild reaches a critical size the powder blade hits the overbuild, affecting the powder distribution and, subsequently, the part geometry. This is a typical example that shows how orientation and location of samples affect the quality of the build.

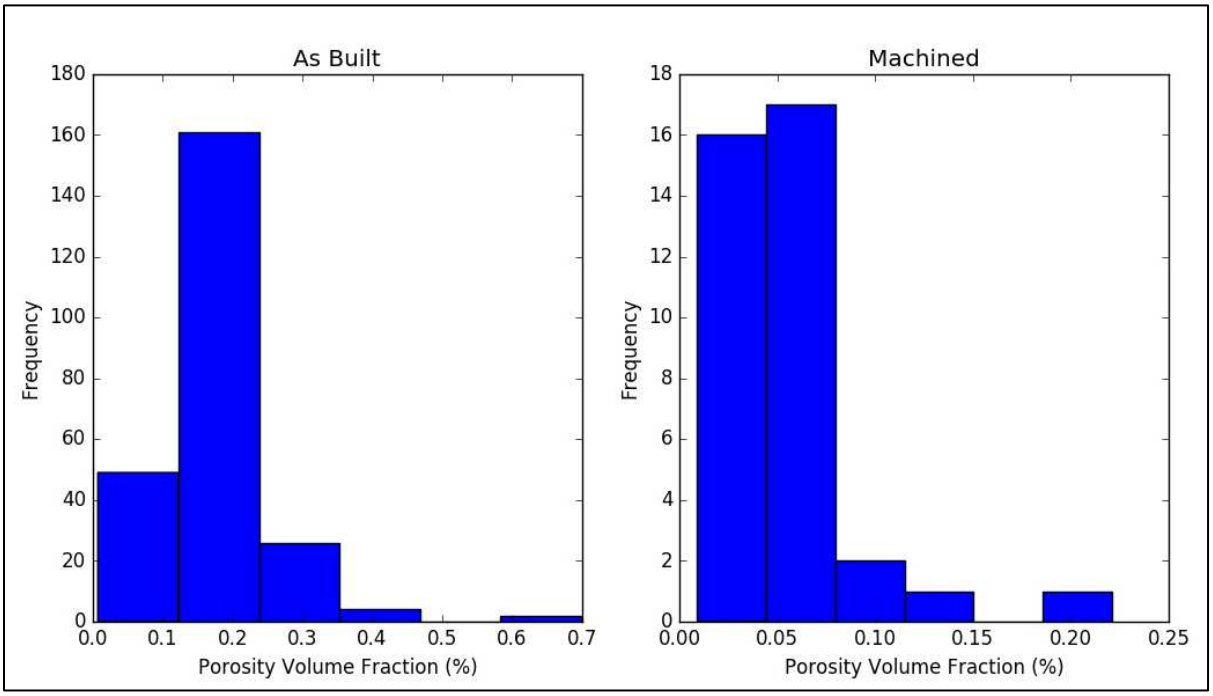

Fig 4.9 Comparison of porosity volume fraction in as-built and machined conditions.

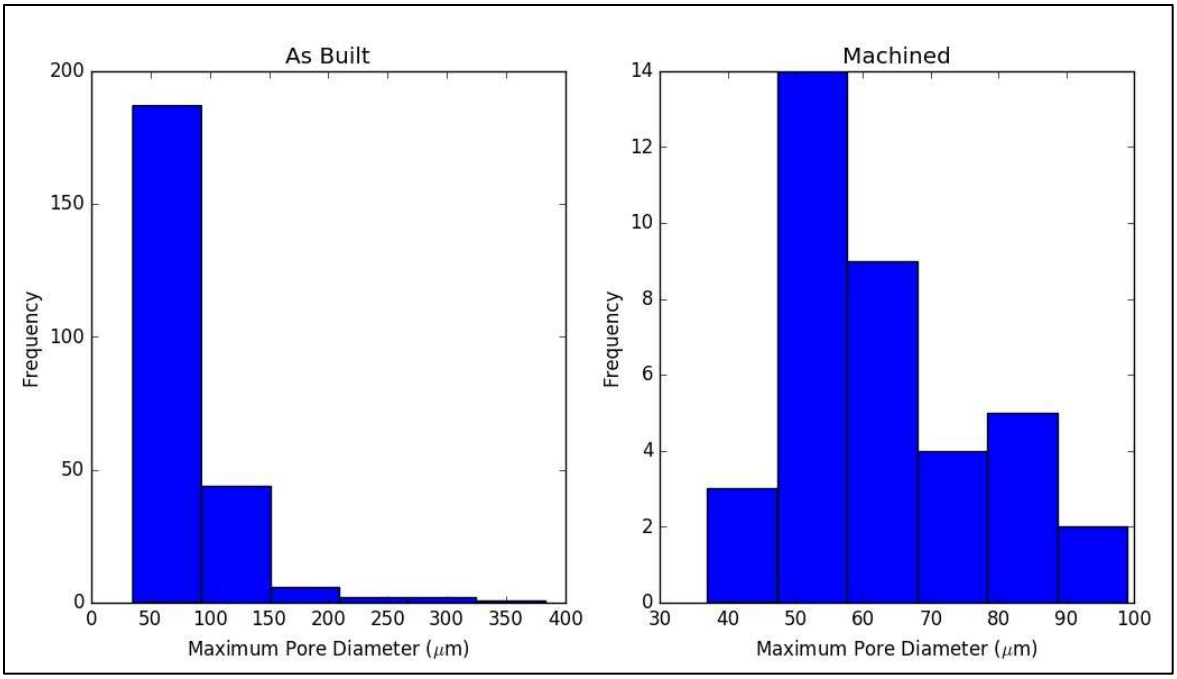

Fig 4.10 Comparison of maximum pore diameter in as-built and machined conditions.

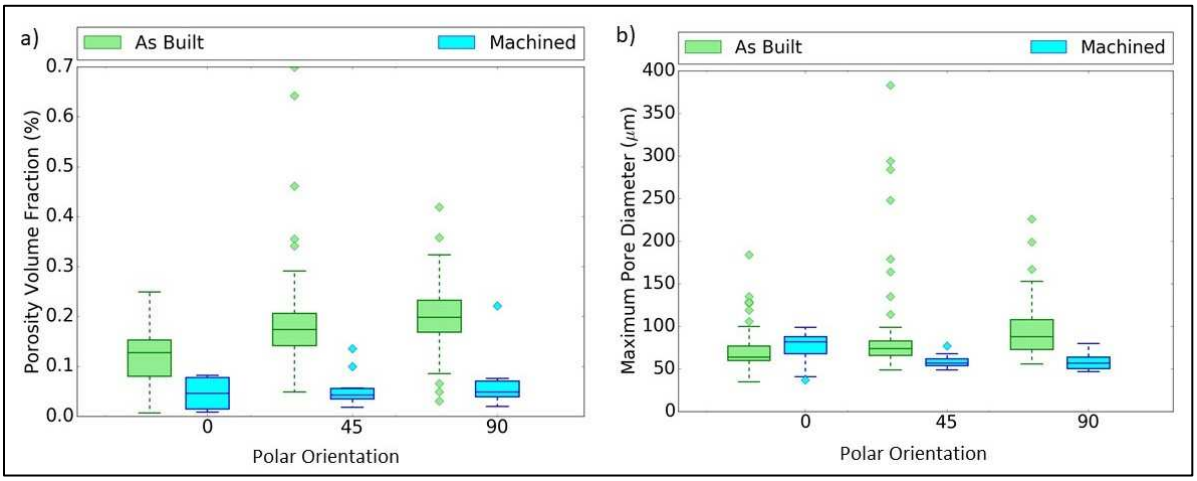

Fig 4.11 Distribution of porosity with respect to polar orientation in as built condition

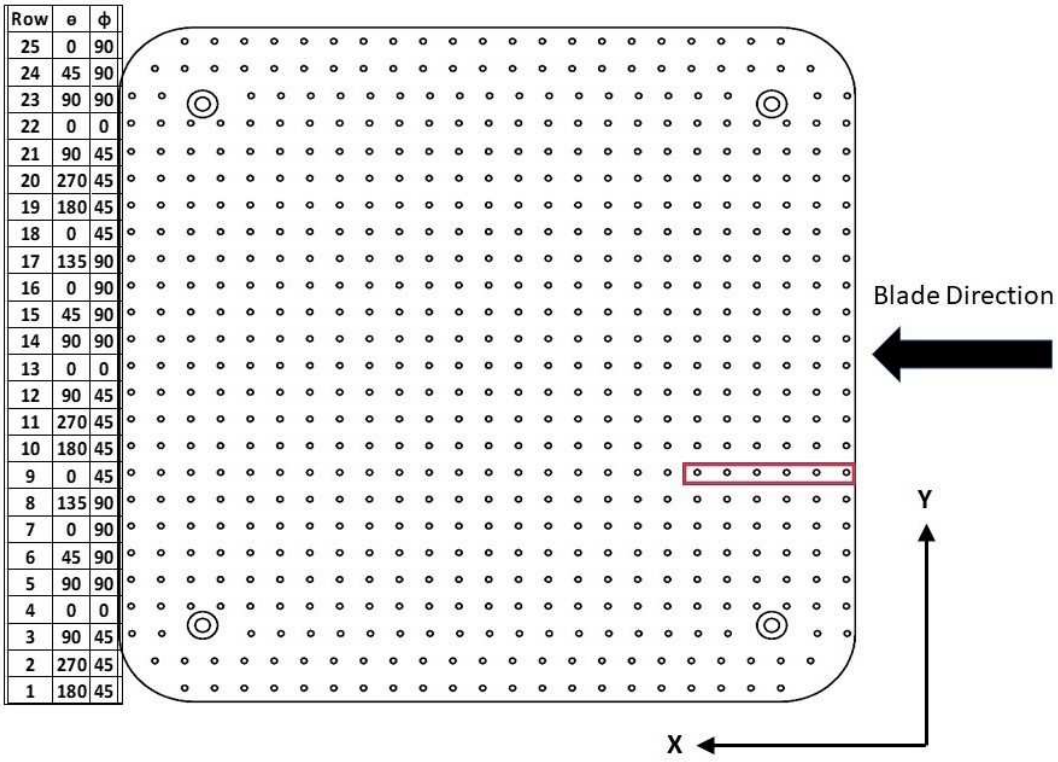

Fig 4.12 Location of samples with high porosity volume and max pore diameter are highlighted in red.

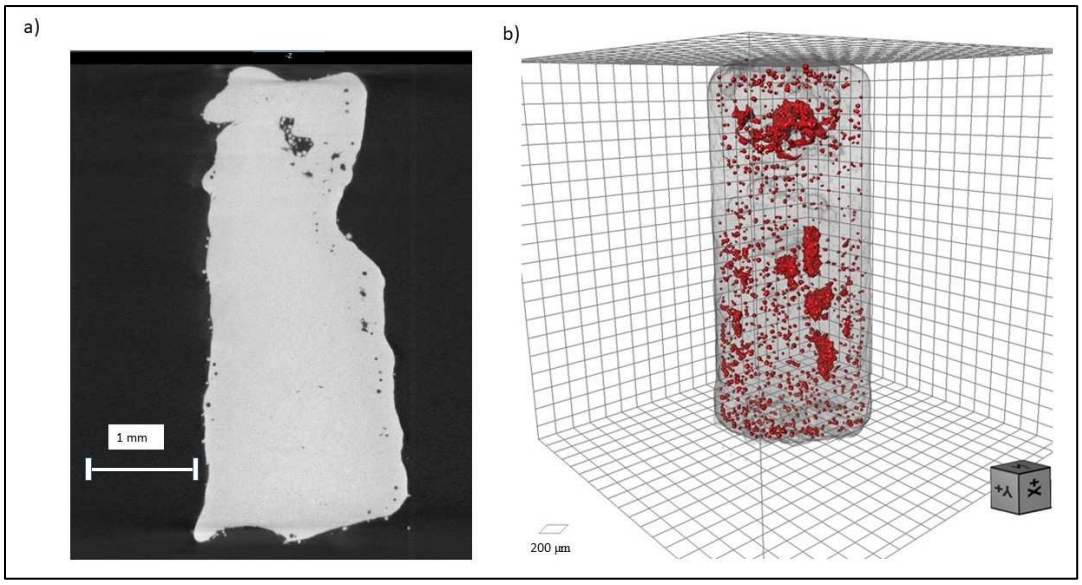

Fig 4.13 Tomography of a compression cylinder showing (a) distortion of the sample topology and (b) the porosity distribution.

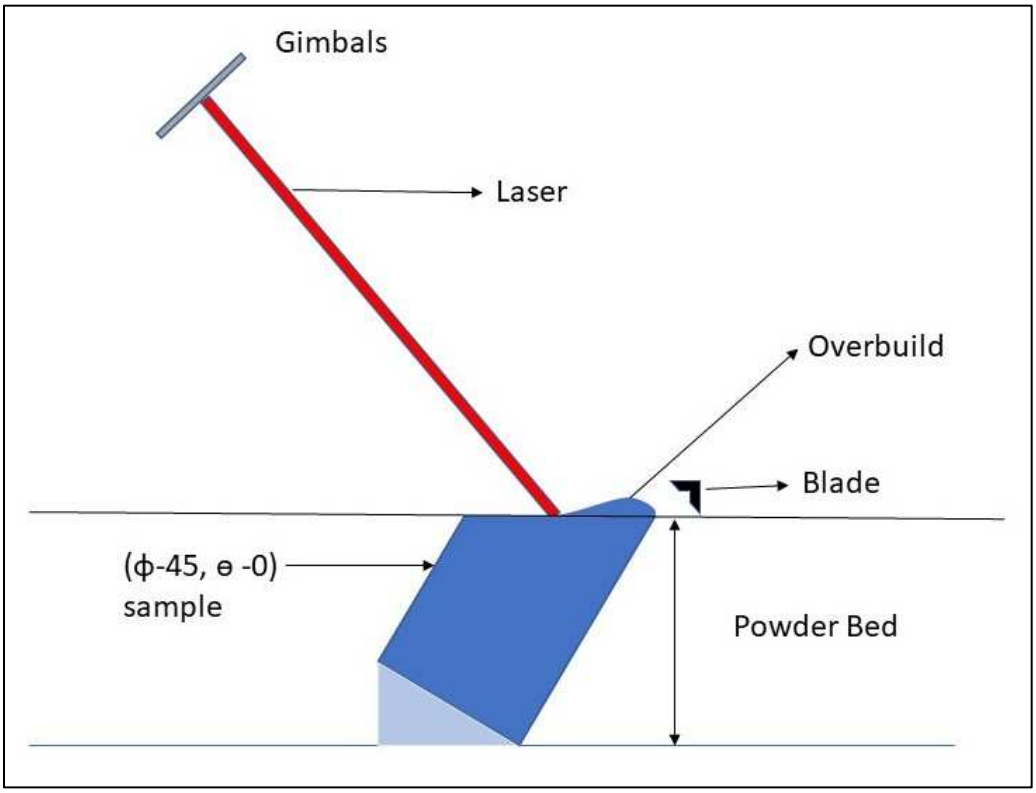

Fig. 4.14 Schematic showing the formation of overbuild in $\phi = 45°$, $\theta = 0°$ oriented sample.

CHAPTER 5

CONCLUSION AND FUTURE SCOPE

Based on the findings discussed in this work, the following conclusions can be made:

1. Both tensile and compressive properties show anisotropy with respect to polar build orientation (ϕ). The effect of a change in azimuthal orientation θ on mechanical properties of $\phi = 0°$ and $\phi = 45°$ oriented compression and tensile samples is insignificant. While the impact on $\phi = 90°$ oriented compression samples is also minor, the impact on $\phi = 90°$ tensile samples is significant. This is because of the relative orientation of the laser scanning path to the sample loading (gage) direction, which changes with azimuthal orientation. The impact of laser scanning path on the final mechanical properties could be studied in detail in future work.

2. Anisotropy due to build orientation and the laser scanning path in the as-built condition is retained after heat treatment. The crystallographic texture that develops with respect to build orientation in the L-PBF process is known and discussed in the literature [56]. This anisotropy may be favorable in the sense that the properties of the part could be tailored, or unfavorable when isotropic properties are desired. In future work, strategies could be researched to control, mitigate, or eliminate anisotropy developed in the L-PBF printed parts.

3. Compression samples tested after machining showed improved mechanical properties. Furthermore, compared to larger diameter, circular cross-section tensile samples reported in the literature [16], tensile samples of $\phi = 0°$ and $\phi = 45°$ orientations exhibit a lower Young's modulus, while $\phi = 90°$ samples show comparable Young's moduli. This provides evidence that the area scanned with contour laser settings may have an impact on the final mechanical properties of samples with smaller cross-sections perpendicular to the build direction. In the future, microstructural variations caused by scanning with contour and skin laser settings and their impact on mechanical properties could be studied.

4. For a given orientation, tensile samples do not show large variations in properties across the build plate; compressive properties do. Preliminary attempts at regression and classification modeling of these variations are discussed in Appendix A. Regression algorithms are unable to accurately predict Young's modulus from orientation and location. Comparatively, classification algorithms seem better suited to model the variation of properties across the build

plate. Though more accurate than regression algorithms, classification algorithms could not exceed 50% accuracy, which suggests that location and orientation of samples could only partially explain the variation in mechanical and structural properties. Additional features are required to better fit the observed property variation, features such as sample composition and microstructure. Such identification is left for future research. A future study could consider modeling variation of mechanical properties with respect to laser parameters such as spot size, overlap, laser power, and speed. The interlayer scanning interval (time interval for scanning one complete layer of the part) would increase with respect to an increase in the area of cross-section perpendicular to the build direction, which would result in different thermal cycles and subsequently change both microstructure and mechanical properties.

REFERENCES

[1] Designation: F2792 − 12a StandardTerminology for Additive Manufacturing Technologies 1,2, (n.d.). doi:10.1520/F2792-12A.

[2] Our Story | 3D Systems, (n.d.). https://www.3dsystems.com/our-story (accessed April 1, 2017).

[3] R. Jiang, R. Kleer, F.T. Piller, Predicting the future of additive manufacturing: A Delphi study on economic and societal implications of 3D printing for 2030, (2017). doi:10.1016/j.techfore.2017.01.006.

[4] C. Weller, R. Kleer, F.T. Piller, Economic implications of 3D printing: Market structure models in light of additive manufacturing revisited, Intern. J. Prod. Econ. 164 (2015) 43–56. doi:10.1016/j.ijpe.2015.02.020.

[5] A. Gebhardt, F.-M. Schmidt, J.-S. Hötter, W. Sokalla, P. Sokalla, Additive Manufacturing by Selective Laser Melting The Realizer Desktop Machine and its application for the Dental Industry, 5 (2010) 543–549. doi:10.1016/j.phpro.2010.08.082.

[6] R. Liu, Z. Wang, T. Sparks, F. Liou, J. Newkirk, 13 - Aerospace applications of laser additive manufacturing, (n.d.). doi:10.1016/B978-0-08-100433-3.00013-0.

[7] C.Y. Yap, C.K. Chua, Z.L. Dong, Z.H. Liu, D.Q. Zhang, L.E. Loh, S.L. Sing, Review of selective laser melting: Materials and applications, Cit. Appl. Phys. Rev. 2 (2015). doi:10.1063/1.4935926.

[8] A. Iturbe, E. Giraud, E. Hormaetxe, A. Garay, G. Germain, K. Ostolaza, P.J. Arrazola, Mechanical characterization and modelling of Inconel 718 material behavior for machining process assessment, (2017). doi:10.1016/j.msea.2016.11.054.

[9] D.M. D 'addona, S.J. Raykar, M.M. Narke, High speed machining of Inconel 718: tool wear and surface roughness analysis, Procedia CIRP. 62 (2017) 269–274. doi:10.1016/j.procir.2017.03.004.

[10] R. D'Aveni, The 3-D Printing Revolution, Harv. Bus. Rev. (2015) 40–48. https://hbr.org/2015/05/the-3-d-printing-revolution.

[11] I. Gibson, D. Rosen, B. Stucker, Additive Manufacturing Technologies, Second, Springer, New York, USA, 2015. doi:10.1007/978-1-4939-2113-3.

[12] H. Bikas, P. Stavropoulos, G. Chryssolouris, Additive manufacturing methods and modeling approaches: A critical review, Int. J. Adv. Manuf. Technol. 83 (2016) 389–405. doi:10.1007/s00170-015-7576-2.

[13] Insights into Continuous Liquid Interface Production (CLIP) and Digital Light Processing (DLP) 3D Printers, additive3d.com. (2016). https://www.additive3d.com/insights-continuous-liquid-interface-production-clip-digital-light-processing-dlp-3d-printers/ (accessed August 28, 2017).

[14] H.P. Tang, M. Qian, N. Liu, X.Z. Zhang, G.Y. Yang, J. Wang, Effect of Powder Reuse Times on Additive Manufacturing of Ti-6Al-4V by Selective Electron Beam Melting,

(n.d.). doi:10.1007/s11837-015-1300-4.

[15] # T Becker, M. Van Rooyen, D. Dimitrov, HEAT TREATMENT OF TI-6AL-4V PRODUCED BY LASERCUSING, South African J. Ind. Eng. August. 26 (2015) 93–103. http://www.scielo.org.za/pdf/sajie/v26n2/09.pdf (accessed January 11, 2018).

[16] E. Chlebus, K. Gruber, B. Ku??nicka, J. Kurzac, T. Kurzynowski, Effect of heat treatment on the microstructure and mechanical properties of Inconel 718 processed by selective laser melting, Mater. Sci. Eng. A. 639 (2015) 647–655. doi:10.1016/j.msea.2015.05.035.

[17] L.E. Murr, K.N. Amato, S.J. Li, Y.X. Tian, X.Y. Cheng, S.M. Gaytan, E. Martinez, P.W. Shindo, F. Medina, R.B. Wicker, W.M. Keck, Microstructure and mechanical properties of open-cellular biomaterials prototypes for total knee replacement implants fabricated by electron beam melting, J. Mech. Behav. Biomed. Mater. 4 (2011) 1396–1411. doi:10.1016/j.jmbbm.2011.05.010.

[18] Dental | 3D Systems, (n.d.). https://www.3dsystems.com/industries/dental (accessed October 2, 2017).

[19] Practical Applications & Uses | Additive Manufacturing | SPI Lasers, (n.d.). http://www.spilasers.com/whitepapers/practical-applications-and-uses-for-additive-manufacturing/ (accessed October 2, 2017).

[20] Metal 3D Printing Applications & Industries | Sciaky, (n.d.). http://www.sciaky.com/additive-manufacturing/applications-industries (accessed October 2, 2017).

[21] A. Gebhardt, Applications, Underst. Addit. Manuf. (2011). doi:10.1016/9783446431621.003.

[22] Aerospace 3D Printing Case Study: Lockheed Martin | Sciaky, (n.d.). http://www.sciaky.com/aerospace-case-study-lockheed-martin (accessed October 2, 2017).

[23] R. Hölker-Jäger, A.E. Tekkaya, Additive manufacture of tools and dies for metal forming, Laser Addit. Manuf. Mater. Des. Technol. Appl. 1 (2016) 439–464. doi:10.1016/B978-0-08-100433-3.00017-8.

[24] M. Attaran, The rise of 3-D printing: The advantages of additive manufacturing over traditional manufacturing, (2017). doi:10.1016/j.bushor.2017.05.011.

[25] B. Geddes, H. Leon, X. Huang, Introduction, in: Superalloays Alloy. Perform., ASM International, 2010: pp. 1–24.

[26] G.A. Greene, C.C. Finfrock, Oxidation of Inconel 718 in Air at High Temperatures, Oxid. Met. 556 (2001). https://link.springer.com/content/pdf/10.1023%2FA%3A1010359815550.pdf (accessed October 4, 2017).

[27] L. Garimella, P.K. Liaw, D.L. Klarstrom, Fatigue Behavior in Nickel.Based Superalioys: A Literature Review, (n.d.). https://link.springer.com/content/pdf/10.1007%2FBF02914771.pdf (accessed October 4,

2017).

[28] B. Pieraggi, J.F. Uginet, FATIGUE AND CREEP PROPERTIES IN RELATION WITH ALLOY 7 18 MICROSTRUCTURE, (n.d.). http://www.tms.org/superalloys/10.7449/1994/superalloys_1994_535_544.pdf (accessed October 4, 2017).

[29] Y.-L. Kuo, S. Horikawa, K. Kakehi, The effect of interdendritic δ phase on the mechanical properties of Alloy 718 built up by additive manufacturing, (2016). doi:10.1016/j.matdes.2016.12.026.

[30] R.B. Li, M. Yao, W.C. Liu, X.C. He, Phases in Inconel 718 alloy, (n.d.). https://ac.els-cdn.com/S1359646202000416/1-s2.0-S1359646202000416-main.pdf?_tid=92ec91bc-a94a-11e7-a3c4-00000aab0f26&acdnat=1507152522_c2f53c996ee173ecbdf5058a768e0874 (accessed October 4, 2017).

[31] Y.-T. Chen, A.-C. Yeh, M.-Y. Li, S.-M. Kuo, Effects of processing routes on room temperature tensile strength and elongation for Inconel 718, Mater. Des. 119 (2017) 235–243. doi:10.1016/j.matdes.2017.01.069.

[32] G.A. Rao, M. Kumar, M. Srinivas, D.S. Sarma, Effect of standard heat treatment on the microstructure and mechanical properties of hot isostatically pressed superalloy inconel 718, (n.d.). doi:10.1016/S0921-5093(03)00079-0.

[33] A. Chamanfar, L. Sarrat, M. Jahazi, M. Asadi, A. Weck, A.K. Koul, Microstructural characteristics of forged and heat treated Inconel-718 disks, Mater. Des. 52 (2013) 791–800. doi:10.1016/j.matdes.2013.06.004.

[34] L. Liu, K. Tanaka, A. Hirose, K.F. Kobayashi, Effects of precipitation phases on the hydrogen embrittlement sensitivity of Inconel 718, (2017). http://iopscience.iop.org/article/10.1016/S1468-6996(02)00039-6/pdf (accessed October 4, 2017).

[35] D.G. Thakur, B. Ramamoorthy, L. Vijayaraghavan, Effect of cutting parameters on the degree of work hardening and tool life during high-speed machining of Inconel 718, (n.d.). doi:10.1007/s00170-011-3529-6.

[36] T. Kitagawa, A. Kubo, K. Maekawa, Temperature and wear of cutting tools in high-speed machining of Incone1718 and Ti-6A1-6V-2Sn, Wear. 202 (1997) 142–148. http://ac.els-cdn.com/S0043164896072559/1-s2.0-S0043164896072559-main.pdf?_tid=c72c72b0-1db0-11e7-a8f0-00000aab0f6b&acdnat=1491803255_307d5415cf6867ab6d4cf97bf9b73398 (accessed April 9, 2017).

[37] W. Akhtar, J. Sun, P. Sun, W. Chen, Z. Saleem, Tool wear mechanisms in the machining of Nickel based super-alloys: A review, (n.d.). doi:10.1007/s11465-014-0301-2.

[38] A. Oradei-Basile, J.F. Radavich, A Current T-T-T Diagram for Wrought Alloy 718, The Minerals, Metals & Materials Soceity, 1991. doi:10.7449/1991/Superalloys_1991_325_335.

[39] H. Xiao, S. Li, X. Han, J. Mazumder, L. Song, Laves phase control of Inconel 718 alloy using quasi-continuous-wave laser additive manufacturing, (2017). doi:10.1016/j.matdes.2017.03.004.

[40] H. Xiao, S.M. Li, W.J. Xiao, Y.Q. Li, L.M. Cha, J. Mazumder, L.J. Song, Effects of laser modes on Nb segregation and Laves phase formation during laser additive manufacturing of nickel-based superalloy, (2016). doi:10.1016/j.matlet.2016.10.118.

[41] K. Kunze, T. Etter, J. Grässlin, V. Shklover, Texture, anisotropy in microstructure and mechanical properties of IN738LC alloy processed by selective laser melting (SLM), Mater. Sci. Eng. A. 620 (2014) 213–222. doi:10.1016/j.msea.2014.10.003.

[42] J.-P. Choi, G.-H. Shin, S. Yang, D.-Y. Yang, J.-S. Lee, M. Brochu, J.-H. Yu, Densification and microstructural investigation of Inconel 718 parts fabricated by selective laser melting, Powder Technol. 310 (2017) 60–66. doi:10.1016/j.powtec.2017.01.030.

[43] R. Konečná, L. Kunz, G. Nicoletto, A. Bača, Long fatigue crack growth in Inconel 718 produced by selective laser melting, Int. J. Fatigue. 92 (2015) 499–506. doi:10.1016/j.ijfatigue.2016.03.012.

[44] T. Trosch, J. Strößner, R. Völkl, U. Glatzel, Microstructure and mechanical properties of selective laser melted Inconel 718 compared to forging and casting, Mater. Lett. 164 (2015) 428–431. doi:10.1016/j.matlet.2015.10.136.

[45] S. Ghorbanpour, M. Zecevic, A. Kumar, M. Jahedi, J. Bicknell, L. Jorgensen, I.J. Beyerlein, M. Knezevic, A crystal plasticity model incorporating the effects of precipitates in superalloys: Application to tensile, compressive, and cyclic deformation of Inconel 718, (2017). doi:10.1016/j.ijplas.2017.09.006.

[46] R. Andreotta, L. Ladani, W. Brindley, Finite element simulation of laser additive melting and solidification of Inconel 718 with experimentally tested thermal properties, (2017). doi:10.1016/j.finel.2017.07.002.

[47] E.R. Denlinger, V. Jagdale, G. V Srinivasan, T. El-Wardany, P. Michaleris, Thermal modeling of Inconel 718 processed with powder bed fusion and experimental validation using in situ measurements, Addit. Manuf. 11 (2016) 7–15. doi:10.1016/j.addma.2016.03.003.

[48] P. Prabhakar, W.J. Sames, R. Dehoff, S.S. Babu, Direct Computational modeling of residual stress formation during the electron beam melting process for Inconel 718, Addit. Manuf. 7 (2015) 83–91. doi:10.1016/j.addma.2015.03.003.

[49] I IN NC CO ON NE EL L ® ® a al ll lo oy y 7 71 18 8, (n.d.). http://www.specialmetals.com/assets/smc/documents/inconel_alloy_718.pdf (accessed October 3, 2017).

[50] ASTM F3055 - 14a Additive Manufacturing Nickel Alloy (UNS N07718) with Powder Bed Fusion, (n.d.). doi:10.1520/F3055-14A.

[51] B. Geddes, H. Leon, X. Huang, Strengthening Mechanisms, in: Superalloays Alloy. Perform., ASM International, 2010: pp. 17–24.

[52] W.D.C. Jr., D.G. Rethwisch, Precipitation Hardening, in: Mater. Sci. Eng. an Introd., Wiley, 2009: pp. 436–440.

[53] W.M. Tucho, P. Cuvillier, A. Sjolyst-Kverneland, V. Hansen, Microstructure and hardness studies of Inconel 718 manufactured by selective laser melting before and after solution heat treatment, (2017). doi:10.1016/j.msea.2017.02.062.

[54] X. Q, T. N, B. L, Modeling and Simulation of Directional Solidification of Ni-Based Superalloy Turbine Blades Casting by Liquid Metal Cooling In: Poole W. et al. (eds) Proceedings of the 3rd World Congress on Integrated Computational Materials Engineering (ICME 2015). Spri, Springer, Cham. (2015). doi:https://doi.org/10.1007/978-3-319-48170-8_25.

[55] W. Meiners, K. Wissenbach, A. Gasser, Shaped Body Especially Prototype or Replacement Part Production, DE19649849C1, 1998.

[56] K.N. Amato, S.M. Gaytan, L.E. Murr, E. Martinez, P.W. Shindo, J. Hernandez, S. Collins, F. Medina, W.M. Keck, Microstructures and mechanical behavior of Inconel 718 fabricated by selective laser melting, Acta Mater. 60 (2012) 2229–2239. doi:10.1016/j.actamat.2011.12.032.

[57] Q. Jia, D. Gu, Selective laser melting additive manufacturing of Inconel 718 superalloy parts: Densification, microstructure and properties, J. Alloys Compd. 585 (2014) 713–721. doi:10.1016/j.jallcom.2013.09.171.

[58] D.H. Smith, J. Bicknell, L. Jorgensen, B.M. Patterson, N.L. Cordes, I. Tsukrov, M. Knezevic, Microstructure and mechanical behavior of direct metal laser sintered Inconel alloy 718, Mater. Charact. 113 (2016) 1–9. doi:10.1016/j.matchar.2016.01.003.

[59] D. Zhang, W. Niu, X. Cao, Z. Liu, Effect of standard heat treatment on the microstructure and mechanical properties of selective laser melting manufactured Inconel 718 superalloy, (2015). doi:10.1016/j.msea.2015.06.021.

[60] Q. Jia, D. Gu, Selective laser melting additive manufactured Inconel 718 superalloy parts: High-temperature oxidation property and its mechanisms, Opt. Laser Technol. 62 (2014) 161–171. doi:10.1016/j.optlastec.2014.03.008.

[61] P. Hanzl, M. Zetek, T. Bakša, T. Kroupa, The Influence of Processing Parameters on the Mechanical Properties of SLM Parts, Procedia Eng. 100 (2015) 1405–1413. doi:10.1016/j.proeng.2015.01.510.

[62] L.N. Carter, C. Martin, P.J. Withers, M.M. Attallah, The influence of the laser scan strategy on grain structure and cracking behaviour in SLM powder-bed fabricated nickel superalloy, J. Alloys Compd. 615 (2014) 338–347. doi:10.1016/j.jallcom.2014.06.172.

[63] F. Liu, X. Lin, C. Huang, M. Song, G. Yang, J. Chen, W. Huang, The effect of laser scanning path on microstructures and mechanical properties of laser solid formed nickel-base superalloy Inconel 718, J. Alloys Compd. 509 (2010) 4505–4509. doi:10.1016/j.jallcom.2010.11.176.

[64] J. Cao, F. Liu, X. Lin, C. Huang, J. Chen, W. Huang, Effect of overlap rate on recrystallization behaviors of Laser Solid Formed Inconel 718 superalloy, Opt. Laser

Technol. 45 (2013) 228–235. doi:10.1016/j.optlastec.2012.06.043.

[65] V. Popovich, E. Borisov, A. Popovich, Vs. Sufiiarov, D. Masaylo, L. Alzina, Functionally graded Inconel 718 processed by additive manufacturing: Crystallographic texture, anisotropy of microstructure and mechanical properties, Mater. Des. 114 (2017) 441–449. doi:10.1016/j.matdes.2016.10.075.

[66] S. Sui, J. Chen, E. Fan, H. Yang, X. Lin, W. Huang, The influence of Laves phases on the high-cycle fatigue behavior of laser additive manufactured Inconel 718, (2017). doi:10.1016/j.msea.2017.03.098.

[67] P. Nie, O.A. Ojo, Z. Li, Numerical modeling of microstructure evolution during laser additive manufacturing of a nickel-based superalloy, Acta Mater. 77 (2014) 85–95. doi:10.1016/j.actamat.2014.05.039.

[68] C.-J. Li, T.-W. Tsai, C.-C. Tseng, Numerical simulation for heat and mass transfer during selective laser melting of titanium alloys powder, Phys. Procedia. 83 (2016) 1444–1449. doi:10.1016/j.phpro.2016.08.150.

[69] Y. Huang, L.J. Yang, X.Z. Du, Y.P. Yang, Finite element analysis of thermal behavior of metal powder during selective laser melting, (2016). doi:10.1016/j.ijthermalsci.2016.01.007.

[70] M.M. Francois, A. Sun, W.E. King, N.J. Henson, D. Tourret, C.A. Bronkhorst, N.N. Carlson, C.K. Newman, T. Haut, J. Bakosi, J.W. Gibbs, V. Livescu, S.A. Vander Wiel, A.J. Clarke, M.W. Schraad, T. Blacker, H. Lim, T. Rodgers, S. Owen, F. Abdeljawad, J. Madison, A.T. Anderson, J.-L. Fattebert, R.M. Ferencz, N.E. Hodge, S.A. Khairallah, O. Walton, Modeling of additive manufacturing processes for metals: Challenges and opportunities, Curr. Opin. Solid State Mater. Sci. 21 (2017) 198–206. doi:10.1016/j.cossms.2016.12.001.

[71] J. Bell, Machine Learning Hands for Developers and Technical Professionals, Wiley, Indianapolis, 2015.

[72] P. Domingos, The Master Algorithm, Basic Books, New York, USA, 2015.

[73] T. Mueller, a G. Kusne, R. Ramprasad, Science : Recent Progress, Mach. Learn. Mater. Sci. Recent Prog. Emerg. Appl. 29 (n.d.).

[74] A. Ethem, Machine learning, 2014.

[75] F. Pedregosa, G. Varoquaux, A. Gramfort, V. Michel, B. Thirion, O. Grisel, M. Blondel, P. Prettenhofer, R. Weiss, V. Dubourg, J. Vanderplas, A. Passos, D. Cournapeau, M. Brucher, M. Perrot, É. Duchesnay, Scikit-learn: Machine Learning in Python, J. Mach. Learn. Res. 12 (2011) 2825–2830. http://jmlr.csail.mit.edu/papers/v12/pedregosa11a.html (accessed November 25, 2017).

[76] Y. Liu, T. Zhao, W. Ju, S. Shi, Materials discovery and design using machine learning, J Mater. 3 (2017) 159–177. doi:10.1016/j.jmat.2017.08.002.

[77] M.A. Shandiz, R. Gauvin, Application of machine learning methods for the prediction of crystal system of cathode materials in lithium-ion batteries, (2016).

doi:10.1016/j.commatsci.2016.02.021.

[78] G. Pilania, C. Wang, X. Jiang, S. Rajasekaran, R. Ramprasad, Accelerating materials property predictions using machine learning, Sci. Rep. 3 (2013) 2810. doi:10.1038/srep02810.

[79] J. Wang, X. Yang, Z. Zeng, X. Zhang, X. Zhao, Z. Wang, New methods for prediction of elastic constants based on density functional theory combined with machine learning, Comput. Mater. Sci. 138 (2017) 135–148. doi:10.1016/j.commatsci.2017.06.015.

[80] A. Chowdhury, E. Kautz, B. Yener, D. Lewis, Image driven machine learning methods for microstructure recognition, Comput. Mater. Sci. 123 (2016) 176–187. doi:10.1016/j.commatsci.2016.05.034.

[81] I. Santos, J. Nieves, Y.K. Penya, P.G. Bringas, Machine-learning-based mechanical properties prediction in foundry production, 2009 Iccas-Sice. (2009) 3–8.

[82] V.R. Surya, K.M.V. Kumar, R. Keshavamurthy, G. Ugrasen, H. V. Ravindra, Prediction of Machining Characteristics using Artificial Neural Network in Wire EDM of Al7075 based In-situ Composite, Mater. Today Proc. 4 (2017) 203–212. doi:10.1016/j.matpr.2017.01.014.

[83] Á. García, O. Anjos, C. Iglesias, H. Pereira, J. Martínez, J. Taboada, Prediction of mechanical strength of cork under compression using machine learning techniques, Mater. Des. 82 (2015) 304–311. doi:10.1016/j.matdes.2015.03.038.

[84] A. Behnood, K.P. Verian, M. Modiri Gharehveran, Evaluation of the splitting tensile strength in plain and steel fiber-reinforced concrete based on the compressive strength, Constr. Build. Mater. 98 (2015) 519–529. doi:10.1016/j.conbuildmat.2015.08.124.

[85] E. Alpaydin, Introduction to Machine Learning, Third, The MIT Press, Massachusetts, 2014.

[86] L. Breiman, Random Forests, Mach. Learn. 45 (2001) 5–32. https://link.springer.com/content/pdf/10.1023%2FA%3A1010933404324.pdf (accessed December 5, 2017).

[87] Nonlinear Classifiers, Pattern Recognit. (2008) 151–260. doi:10.1016/B978-1-59749-272-0.50006-2.

[88] C. Saunders, A. Gammerman, V. Vovk, R. Holloway, Ridge Regression Learning Algorithm in Dual Variables, (n.d.). http://citeseerx.ist.psu.edu/viewdoc/download?doi=10.1.1.872.1902&rep=rep1&type=pdf (accessed December 5, 2017).

[89] K. Rakesh, P.N. Suganthan, ScienceDirect An Ensemble of Kernel Ridge Regression for Multi-class Classification, Procedia Comput. Sci. 108 (2017) 375–383. doi:10.1016/j.procs.2017.05.109.

[90] Z. Wang, K. Guan, M. Gao, X. Li, X. Chen, X. Zeng, The microstructure and mechanical properties of deposited-IN718 by selective laser melting, J. Alloys Compd. 513 (2011) 518–523. doi:10.1016/j.jallcom.2011.10.107.

[91] Q. Jia, D. Gu, Selective laser melting additive manufactured Inconel 718 superalloy parts: High-temperature oxidation property and its mechanisms, Opt. Laser Technol. 62 (2014) 161–171. doi:10.1016/j.optlastec.2014.03.008.

[92] A.A. Popovich, V.S. Sufiiarov, I.A. Polozov, E. V. Borisov, Microstructure and Mechanical Properties of Inconel 718 Produced by SLM and Subsequent Heat Treatment, Key Eng. Mater. 651–653 (2015) 665–670. doi:10.4028/www.scientific.net/KEM.651-653.665.

[93] ASTM, ASTM E-8/E-8M; Standard Test Methods for Tension Testing of Metallic Materials, Astm. (2009) 1–27. doi:10.1520/E0008.

[94] C. Aca-, THE TENSION / COMPRESSION FLOW STRESS ASYMMETRY IN Ni3 (Al , Nb) SINGLE CRYSTALS, (1981).

[95] C. Lei, W. Weidong, C. Haitao, Z. Hongjian, X. Ying, Yield anisotropy and tension/compression asymmetry of a Ni 3 Al based intermetallic alloy, Chinese J. Aeronaut. 26 (2013) 801–806. doi:10.1016/j.cja.2013.04.002.

[96] G. Tapia, A.H. Elwany, H. Sang, Prediction of porosity in metal-based additive manufacturing using spatial Gaussian process models, Addit. Manuf. 12 (2016) 282–290. doi:10.1016/j.addma.2016.05.009.

[97] H. Geerlings, High throughput image based porosity characterization using TRACR, Colorado School of Mines, 2018.

[98] N. Mccormick, J. Lord, Digital Image Correlation, Mater. Today. 13 (2010) 52–54. doi:10.1016/S1369-7021(10)70235-2.

[99] V. Popovich, E. Borisov, A. Popovich, Vs. Sufiiarov, D. Masaylo, L. Alzina, Functionally graded Inconel 718 processed by additive manufacturing: Crystallographic texture, anisotropy of microstructure and mechanical properties, Mater. Des. 114 (2017) 441–449. doi:10.1016/j.matdes.2016.10.075.

[100] B. Pan, K. Qian, H. Xie, A. Asundi, Two-dimensional digital image correlation for in-plane displacement and strain measurement: a review Two-dimensional digital image correlation for in-plane displacement and strain measurement: a review, Meas. Sci. Technol. 20 (2009) 62001–17. doi:10.1088/0957-0233/20/6/062001.

[101] ASTM, ASTM E384-2016: Standard Test Method for Knoop and Vickers Hardness of Materials, ASTM Stand. (2016) 1–43. doi:10.1520/E0384-16.

[102] ASTM, ASTM E-9;Standard Test Methods of Compression Testing of Metallic Materials at Room Temperature, Annu. B. ASTM Stand. 3.01 (2012) 92–100. doi:10.1520/E0009-09.2.

APPENDIX A

INVESTIGATION OF THE RELATIONSHIP BETWEEN ORIENTATION, LOCATION AND MECHANICAL PROPERTIES USING MACHINE LEARNING ALGORITHMS

A.1 Data collection and processing

A total of 72 compression samples of nine different orientations were tested in the as-built condition. Young's modulus was chosen as the target property for modeling, as it shows wide variation. The following variables are used as input parameters to predict the Young's modulus:

a) X (mm) – Horizontal distance from the plate edge. (Ref Fig 6.1)

b) Y (mm) – Vertical distance from the bottom edge of the plate. (Ref Fig 6.1)

c) ϕ (degree) – Polar orientation

d) θ (degree) – Azimuthal orientation

The first problem was approached using the dimensionality reduction and data visualization technique t-SNE (t-distributed stochastic neighbor embedding) to observe any obvious spatial correlation between input parameters and Young's modulus and to identify gaps in sampling the phase space. Subsequently, the problem was approached with the regression technique to examine any relationship between input and output parameters. Finally, the problem was approached using the classification technique. For the development of all machine learning models, Python module *Scikit-learn* [75] was used in this research work.

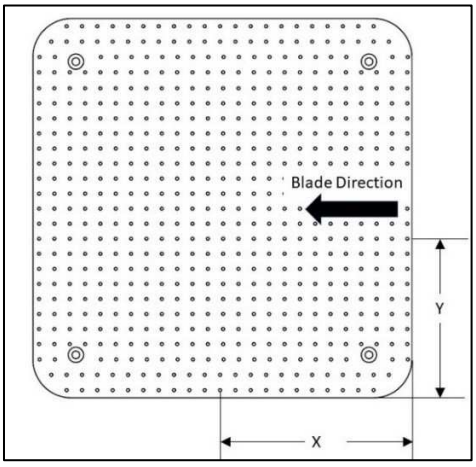

Fig A.1 Horizontal (X) and vertical (Y) distance from edge of the plate

A.2 t-SNE plot

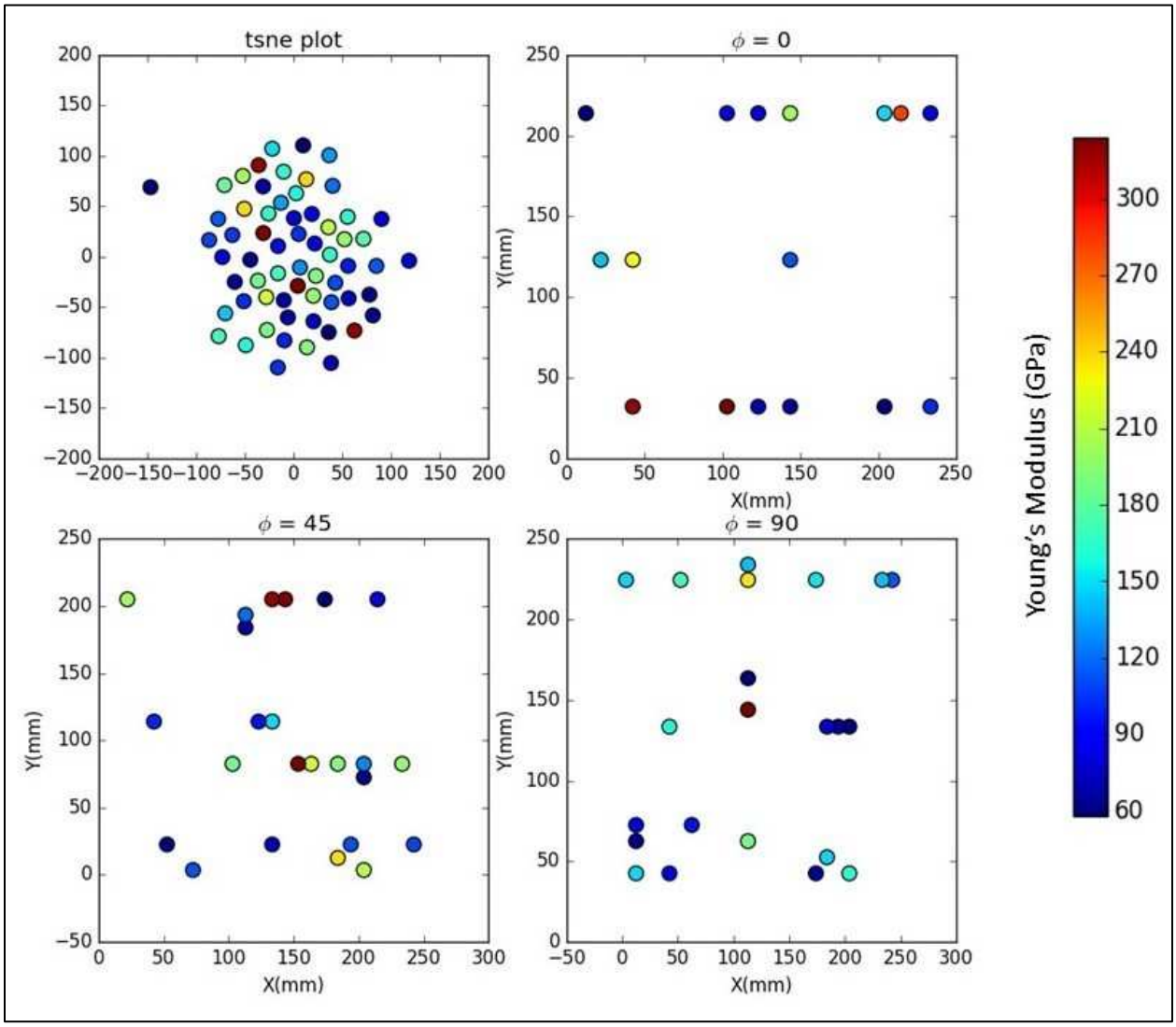

Fig. A.2 a) t-SNE plot, Young's modulus vs. location, b) ϕ = 0°, c) ϕ = 45°, d) ϕ = 90°

Figure A.2a shows the t-SNE plot, which visualizes spatial relationship by reducing four dimensions X, Y, θ, and ϕ, to two dimensions. Figure A.2b, c, and d show the variation of Young's modulus with respect to the location of the sample on the plate. No obvious relationship between the location of the sample and its Young's modulus could be observed from the plots. Also, the t-SNE plot does not show any interesting clustering that could describe the variation of Young's modulus; hence, regression algorithms were used to find any nonlinear relationship between input parameters and output.

A.3 Regression algorithms.

As the distribution of powder may vary from blade start point to finish across the build plate, and the angle of incidence of the laser varies for samples in the middle of the plate to samples at the edges, a functional relationship between sample position on the build plate and its mechanical properties could be expected. Regression algorithms were used to investigate the possibility of a nonlinear relationship between input parameters X, Y, θ, and ϕ, and output parameter Young's modulus. Regression models like decision tree regression, random forest regression, kernel ridge regression, and support vector regression were used to model available data. Tenfold cross-validation was performed to evaluate the performance of these models. Mean absolute error (MAE) was used as a metric to estimate the model performance. Results are shown in Fig. A.3.

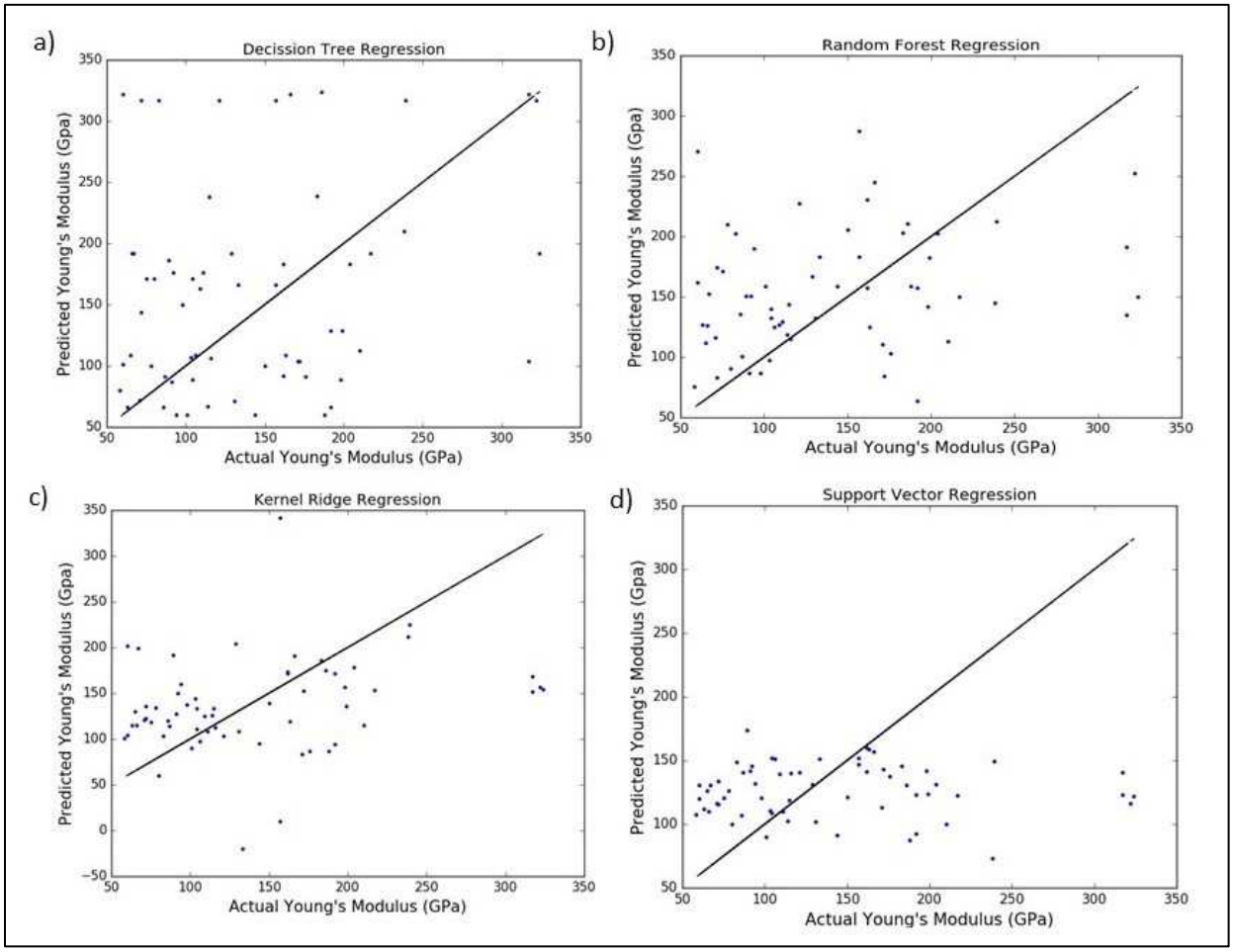

Fig A.3 Predictions for cross-validated model a) decision tree regression b) random forest regression c) kernel ridge regression d) support vector regression

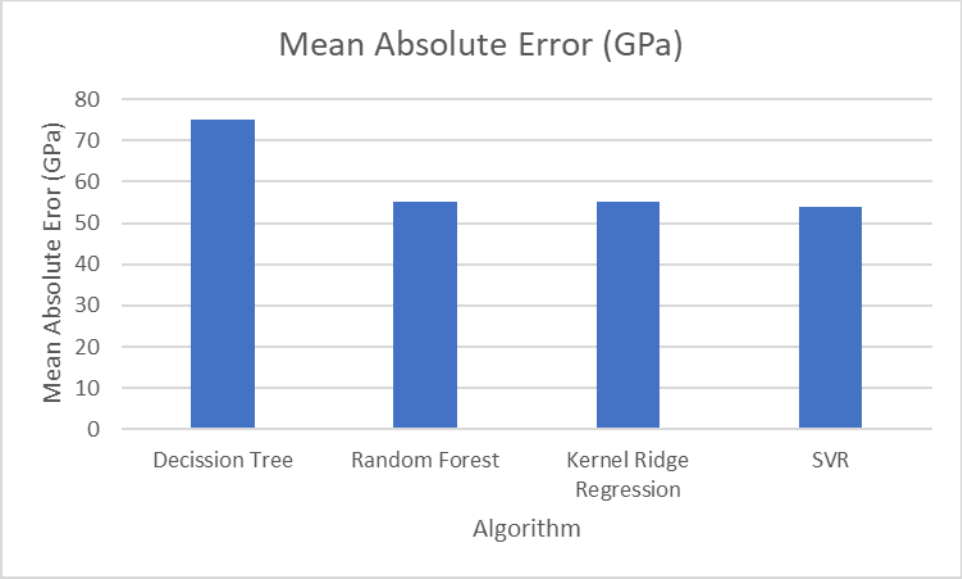

Fig A.4 Mean absolute error in 10-fold cross validation

None of these regression algorithms were consistent in predicting the Young's modulus. All these algorithms could predict only with a mean absolute error of at least 50 GPa. This means that there is 100 GPa of uncertainty in all predictions. Therefore, these models are not reliable in predicting the Young's modulus. It could be understood that input variables do not have non-linear relationship with the Young's modulus.

A.4 Classification algorithms

From the failure of regression algorithms to predict the modulus precisely, it can be understood that variability in data does not allow precise prediction of properties with respect to orientation and location. Regression modeling may have failed because of the small sample size, and regression algorithms may be sensitive to outliers. So, a new approach of classification model was used to predict a range of Young's modulus achievable for a sample with desired orientation and location.

Young's modulus was converted into a categorical variable by dividing it into four different classes. Two different methods were used in classifying the data.

Method 1: Four different classes in accordance with four bins uniformly divided as shown in the histogram in Fig. A.5a.

Method 2: Assumes a normal distribution. Four different classes based on mean μ and standard deviation σ. Class1: Modulus < μ -σ, Class2: μ – σ < Modulus < μ, Class3: μ < Modulus μ + σ and Class4: Modulus > μ + σ

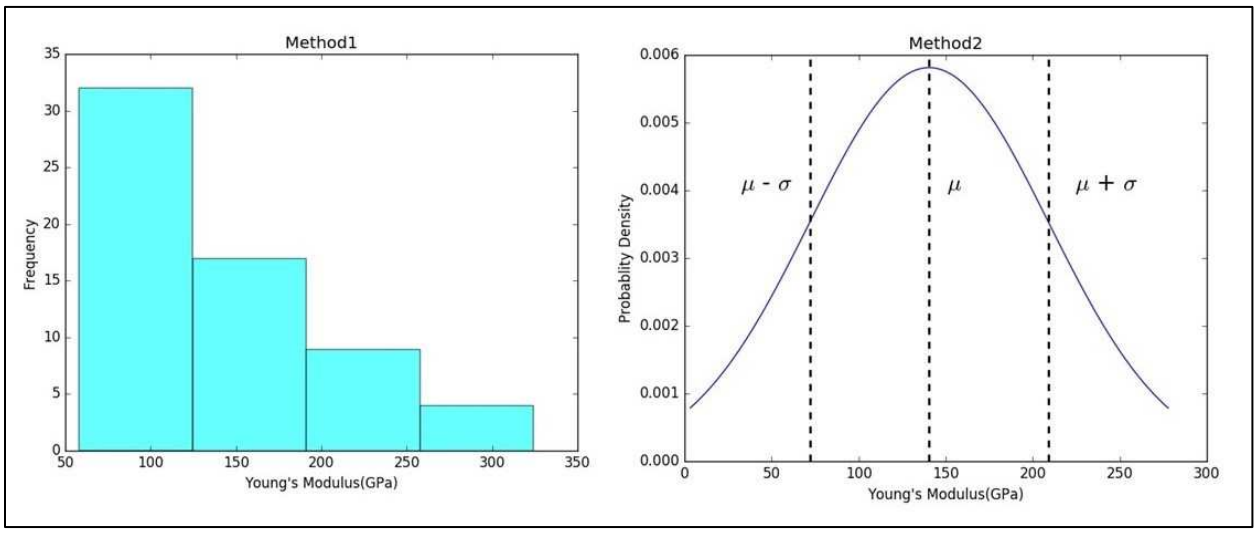

Fig A.5 a) Histogram plot of Young's modulus b) normal distribution

Five different classification algorithms—decision tree classification, random forest classification, K-neighbor classification, naïve Bayes, and SVM classification—were used to model the data classified according to both methods. Since the number of samples in each class was not equal, instead of K-fold cross-validation, stratified K-fold (fivefold) cross-validation was used to estimate the performance outside the training range. Stratified K-fold cross-validation ensures the percentage of samples in each class is preserved in all of the five folds divided. Average precision, recall, f-1 score, and accuracy score were used as metrics for comparing the performance of the classification algorithms. Final results are shown in Figs. A.6 and A.7.

From results shown in Figs. A.6 and A.7, it could be observed that the classification algorithm works better than regression. Also, from Figs. A.6 and A.7, it could be inferred that K-neighbor classifier works better than other classifiers in Method 1 classification and naïve Bayes classifier works better in Method 2 classification. They have balanced recall, precision, and f1-score as well.

K-neighbor classifier works based on reducing the Euclidean distance between the data points in multidimensional space. The fact that it works better for this problem than other

classifiers confirms that samples having the same build orientation and similar location tend to have similar properties. Naïve Bayes classifier works better in Method 2 because naïve Bayes classifier assumes a Gaussian distribution of the data, which matches with the definition of classification in the second method.

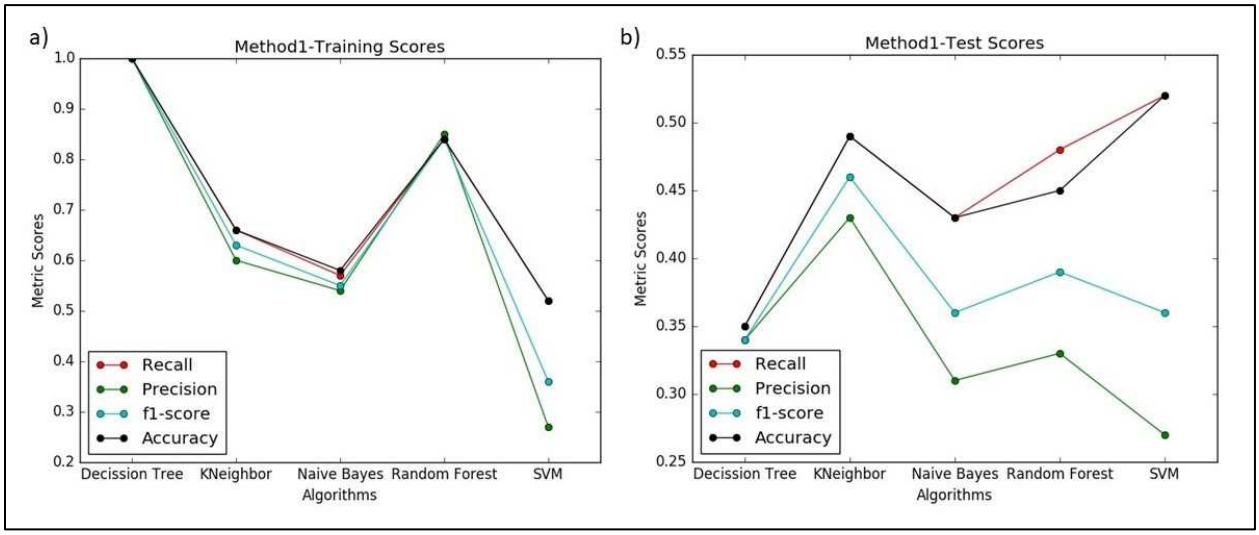

Fig A.6 Performance results of classification algorithms for Method 1

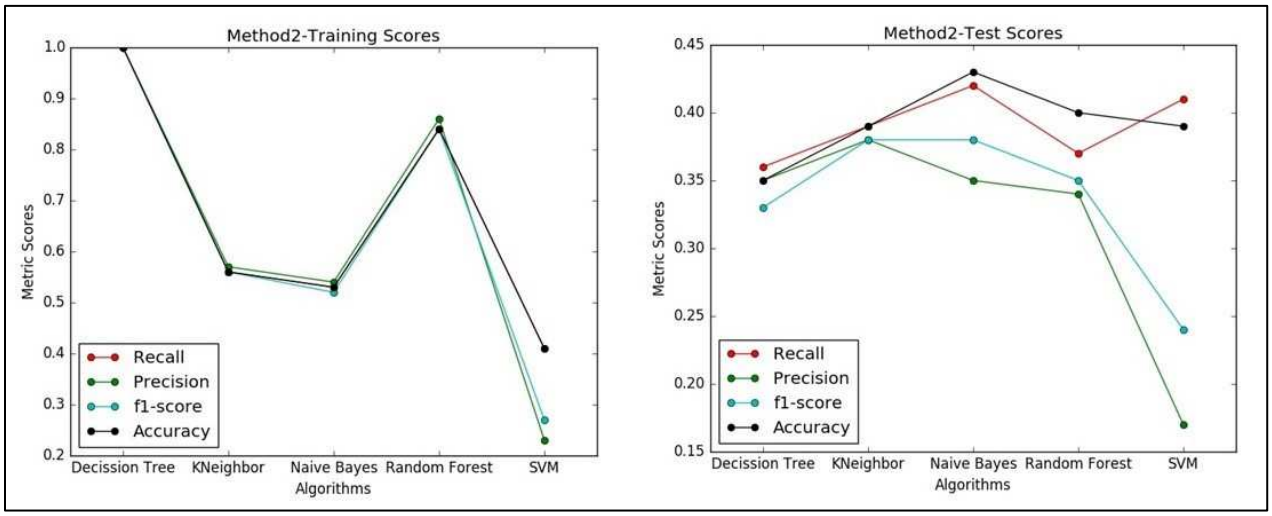

Fig A.7 Performance results of classification algorithms for Method 2

For comparing the two best classification models, a confusion matrix of both models from all five iterations is plotted (Fig. A.8). It is clear from Fig. A.8 that the naïve Bayes classification model using Method 2 classification works better, as it could predict at least three classes with higher classification accuracy.

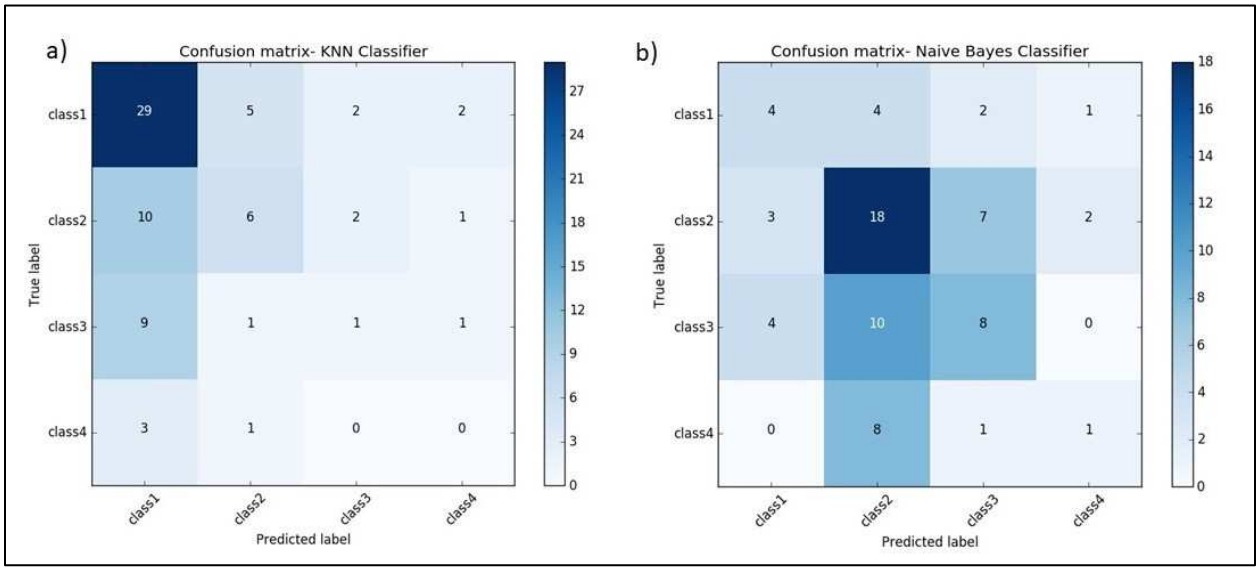

Fig A.8 Confusion matrix of a) KNN classifier Method 1 and b) Naïve Bayes classifier Method 2

Although classification algorithms perform better than regression models they could not exceed 50% accuracy. This explains that there are variations that could not be explained by orientation and location of the sample. Investigation into microstructural variations, examination of compositional variations and probing into defects other than porosity may be required to explain these variations.